
PAVOL JOZEF ŠAFÁRIK
UNIVERSITY
IN KOŠICE
NFA 2024
The 8th International
Conference on
NOVEL MATERIALS
Fundamentals and Applications
2024
13 -16th October 2024
Štrbské Pleso, High Tatras
innovlab
SBaA
T··Systems·
METTLER TOLEDO
ÚSTAV
CHEMICKÝCH VIED
Metrohm
supported by
Visegrad Fund
NATO
OTAN
EUROPEAN UNION
European Regional Development Fund
OP Integrated Infrastructure 2014 – 2020
MINISTERSTVO
ŠKOLSTVA, VEDY,
VÝSKUMU A ŠPORTU
SLOVENSKEJ REPUBLIKY
SLOVAK RESEARCH
AND DEVELOPMENT
AGENCY
InoHub
Energy
https://nfa.science.upjs.sk

Pavol Jozef Šafárik University on Košice
Faculty of Science

BOOK OF ABSTRACTS

The 8th International Conference on Novel Materials Fundamentals and Applications

October 13-16, 2024
Organized by:

Department of Physical Chemistry
Faculty of Science
Pavol Jozef Šafárik University in Košice
&
Slovak Chemical Society
Bratislava

Košice 2024

The 8th International Conference on Novel Materials Fundamentals and Applications

Book of Abstracts

Edited by: Jana Shepa, *Pavol Jozef Šafárik University in Košice, Institute of Chemistry, Moyzesova 11, 040 01 Košice, Slovakia, jana.shepa@upjs.sk*

Reviewed by: Erika Múdra, *Intitute of Materials Research, Slovak Academy of Sciences, Watsonova 47, 040 01 Košice, Slovakia, emudra@saske.sk*

Ivan Shepa, *Intitute of Materials Research, Slovak Academy of Sciences, Watsonova 47, 040 01 Košice, Slovakia, ishepa@saske.sk*

Organized by:
Pavol Jozef Šafárik University in Košice
Slovak Chemical Society
Slovak Battery Alliance

Available at: https://unibook.upjs.sk
Publication date: 11.10.2024

ISBN 978-80-574-0353-1 (e-publication)

LIST OF CONTENTS

LIST OF AUTHORS

Preface

On behalf of the NFA 2024 Organizing Committees, we introduce with pleasure these proceedings devoted to contributions from the 8th NFA Novel Materials Fundamentals and Applications conference held in Štrbské pleso, High Tatras, Slovakia. The conference is organized by the Faculty of Science Pavol Jozef Šafárik Uninversity in Košice and Slovak Chemical Society. The conference program provides an opportunity for researchers interested in various applications of nanomaterials to discuss their latest results and exchange ideas on the new trends. The main objective of the conference umbrella is to encourage discussion on a broad range of related topics and to stimulate new collaborations among the participants.

The proceedings contain all papers of both: oral and poster presentations. We hope that these proceedings will give readers an excellent overview of important and diversity topics discussed at the conference. We thank all authors for submitting their latest work, thus contributing to the excellent technical contents of the Conference. Especially, we would like to thank the organizators that worked diligently to make this conference a success, and to the recenzents for the thorough and careful review of the papers.

We wish all attendees of NFA 2024 an enjoyable scientific gathering in High Tatras, Slovakia. I wish all participants enjoy this scientific meeting to collect new information form nanoscience.

Ivana Šišoláková

This is not just a potentiostat

µStat-i Multi16

Introducing µStat-i MultiX by Metrohm DropSens

Enhanced possibilities for electrochemical research based on an efficient, versatile and reliable user experience are at hand with the newly launched µStat-i MultiX. This multi-channel bipotentiostat, galvanostat and impedance analyzer (with MultiplEIS® technology for performing dual-channel Electrochemical Impedance Spectroscopy) is suitable for multi-user and multi-disciplinary work.

Choose the number of channels that you need (with optional floating mode), benefit from having several users working with the same instrument at the same time, work remotely and support your research with an easy to use software.

Electrochemistry has proven its high potential to solve real-life analytical problems. µStat-i MultiX simplifies analytical research and transforms daily work.

Discover more about µStat-i MultiX by visiting: www.metrohm.com

PEOPLE
YOU
CAN
TRUST

FIND OUT MORE

Metrohm

Invited Lectures

8th International Conference on Novel Materials Fundamentals and Applications
High Tatras, 13.-16.10.2024

Impedance Spectroscopy: Fundamentals and Applications

G. Fafilek[a]*

[a] Institute of Chemical Technologies, TU Wien, Getreidemarkt 9/164ec
*guenter.fafilek@tuwien.ac.at

Electrochemical impedance spectroscopy is a versatile tool for the characterization of materials and electrochemical processes. It provides a detailed insight into the electrical properties of electrochemical systems or even physicochemical processes like mass transport phenomena connected to Faradaic processes.

On one hand – technically – it is a simple method widely used in battery and fuel cell research, corrosion science and other fields of electrochemistry. However, on the other hand, since specific impedance data is not exclusively connected to specific processes, the physical interpretation of impedance spectra is challenging.

The "impedance" is the ratio between a voltage across a component and the electrical current flowing through it.

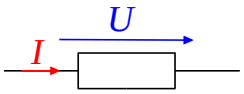

$$\underline{U} = \underline{Z} \cdot \underline{I}$$

voltage — impedance — current

Fig. 1 Relation between alternating current and voltage for a component resembling Ohm's law.

The value for the impedance at a certain frequency of a sine-wave shaped AC signal is a complex number. Considering the impedance in terms of absolute value (or modulus) and phase angle, the modulus reflects the ratio between the amplitudes of the voltage and the current, like it is the case in Ohm's law for ohmic resistors. However, some basic electrical elements, like capacitors or inductors, behave like small energy storage elements, and therefore for them, Ohm's law is not valid at all times. This behaviour causes – for sine-waves – a phase shift between current and voltage. The phase angle of the complex value for the impedance is identical to this phase shift. For the impedance of a mixed network consisting of resistors and capacitors (or other AC elements), modulus and phase angles are frequency dependent. The frequency dependence of a system is a kind of "fingerprint" for the occurring processes.

This contribution shows the mathematical origins of the concept "impedance" and derive the basics of the "golden rules" to be followed when measuring impedance.

These are → make sure that your system fulfils:

- linearity
- stability
- causality

which is difficult to achieve in electrochemical systems. Electrochemical processes are strongly non-linear, which means that Ohm's law ($U = I \cdot R$) does not apply in general. Moreover, such systems are not stable, e.g. a corroding surface changes its properties over time or a battery might change its state of charge during a measurement. The third condition "causality" might be violated by external sources of signals e.g. noise.

The first step in making good impedance measurements is to build a suitable measuring setup. The most important rule is shielding to avoid external noise. Use short cables to reduce inductive effects and again noise. When using 3 electrodes, like it is often the case in electrochemical setups, additional complications arise from the bandwidth of the potentiostat and from coupling effects between the electrodes.

Since the system can be non-linear, low signal amplitudes have to be used. It is very common to apply a voltage with just 5mV amplitude to avoid non-linear current response. In this case, the signal to noise ratio might become an issue.

If stability could be a problem, the data can be checked with the Kramers-Kronig-relation. Modulus and phase or real and imaginary part of the complex impedance cannot change independently with frequency. The KK-relation checks if these values correlate correctly and if not, stability might be a problem. As an example, a pure ohmic resistor has phase angle of 0 degree and a frequency independent modulus. If the resistor changes with time (the system is not stable), a change of the modulus with frequency is observed because each measured data point corresponds to a different point in time. The KK-test detects such, even less obvious, inconsistencies.

Once valid impedance data is available, in most cases it can be related to the behaviour of an electrical equivalent circuit. Selecting a suitable equivalent circuit is the second step in successfully analysing the impedance of a system. Theoretically, an impedance spectrum can always be described by an equivalent circuit, provided it is sufficiently complicated. The challenge is to find a circuit of which the elements can be related to electrochemical or physical processes.

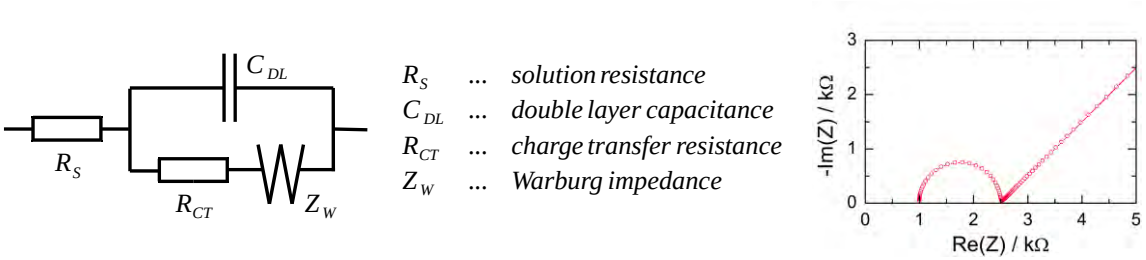

Fig. 2 Randles equivalent circuit [1] with the denotation of each element and the complex plane plot of the corresponding impedance spectrum.

The most common circuit, which describes the behaviour of an electrode is the Randles equivalent circuit displayed in Fig. 2. It includes the properties of the interface between the electronic conductor (the electrode) and the ionic conductor (the electrolyte solution), consisting of the double layer capacity (C_{DL}) and the resistance of the double layer (R_{CT}) against the charge transfer reaction which is the redox reaction of an electroactive species (a Faraday reaction). Limited mass transport by diffusion is described with the Warburg impedance Z_W. The Warburg impedance is a specific combination of resistive and capacitive (storage) elements in a "transmission line". R_S represents the solution resistance of the cell.

Such simple equivalent circuits are only valid for "simple systems". This means for instance that a one-dimensional geometry has to be assumed. However, real systems do not have a one-dimensional geometry, they do have a, sometimes complicated, 3-D geometry on the nano- to macroscopic scale. Real electrodes have roughness, are porous or have certain shapes and arrangements in relation to each other. In addition, the electrical parameters can have a spatial distribution. All these properties influence the impedance spectra, which must be taken into account. In order to include these effects in equivalent circuits, so-called "constant phase elements" CPEs are used. Strictly speaking, resistors and capacitors are also CPEs, with phase angles of 0° and -90° respectively. A general CPE is neither a resistor nor a capacitor, but something in between with a phase angle of $0° > \varphi > -90°$. For example, the double layer capacitance is often described as a CPE with a phase angle close to, but not exactly -90°.

After selecting the proper equivalent circuit diagram for a system, the third step in impedance analysis is to determine the correct values for the elements. For this purpose, a non-linear curve fitting of complex functions with multiple parameter adjustment is performed. Fortunately, there is special software that enables the drawing of electrical circuits and the automatic generation of the impedance function. The program finds minima of the target function, which is the sum of squared differences between measured and calculated data. With complicated circuits, there is a risk of getting stuck in local minima. Good estimates for the initial values are therefore important.

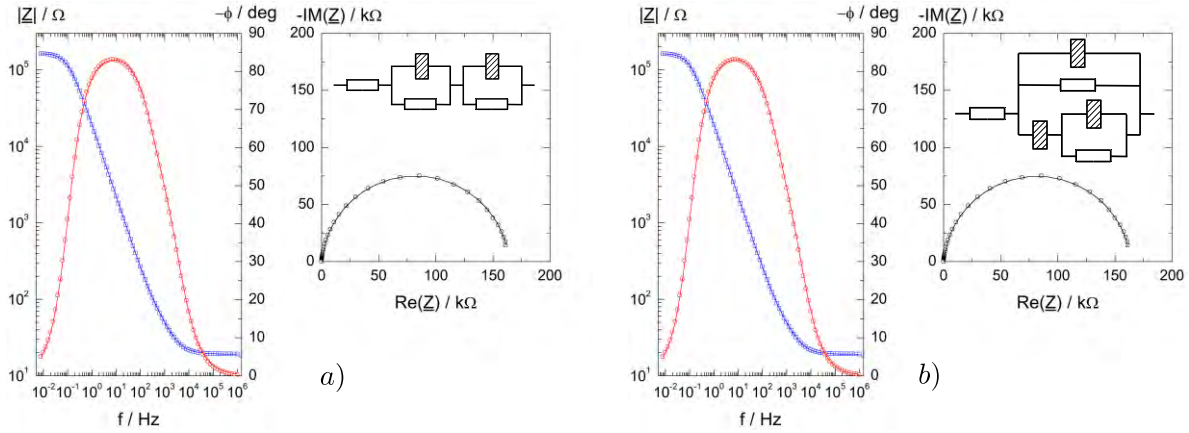

Fig. 3 EIS of a passive layer on Zn (symbols), a) and b) show the simulated impedance (lines) with two different equivalent circuits (inserts). The quality of the fit is practically equal, however model b) better represents the physical properties of the passive layer [2].

In Fig. 3 a comparison is made between two fits with different equivalent circuits representing the impedance of a passive Zn surface. There is practically no difference of the quality of the fit, which shows the difficulties in finding the right model.

If there is a good fit, the story is not over yet. The last step of the procedure is to identify the elements with physical processes. This interpretation of the equivalent circuit is the most important, but also the most difficult part of impedance analysis. It requires additional knowledge of the system, either from experience or from additional experiments, such as independent analytical data or specific electrochemical methods. In some examples it is demonstrated how the interpretation of impedance spectra is possible by varying the experimental conditions. For instance, the model of the example in Fig.3 b) is the better choice, since the parameters change their values correctly with the applied DC-potential.

References

[1] J. E. B. Randles, “Kinetics of rapid electrode reactions”, *Discuss. Faraday Soc.*, vol.1, pp. 11-19, 1947, doi: 10.1039/DF9470100011.

[2] G. Fafilek, “A novel experimental method for potential controlled electrochemical impedance spectroscop”, *Monatshefte fuer Chemie*, vol.140, pp. 1121-1127, 2009.

High Capacity Ink-Jet Printing as a Viable Method for the PEM Fuel Cells Catalyst Layer Deposition?

M. Hala[a], M. Prokop[a], M. Veselý[a], P. Čapek[a], T. Zubkova[b], K. Heinrich[b], A. Willert[b], R. Zichner[b], K. Bouzek[a*]

[a] Department of Inorganic Technology, University of Chemistry and Technology, Prague
Technicka 5, 166 28, Prague 6, Czech Republic
[b] Fraunhofer Institute for Electronic Nano Systems ENAS, Technologie-Campus 3
09126 Chemnitz, Germany
*bouzekk@vscht.cz

Broad implementation of the hydrogen technologies into daily life applications requires important changes in the currently used production technologies. Rapid and cost-effective manufacturing of the individual components is essential. This concerns also PEM fuel cells and production of their components. Beside rapidness and cost effectiveness, often saving of cost intensive materials is necessary. This especially concerns platinum based catalyst. Therefore, in the present study, the focus is on method of the catalyst layer deposition. Currently used technologies, like decal, slot die or spray coating are characterized by different operational features defining their field of application. The issues they are facing are connected mainly to either slow production rate and/or catalyst losses caused by depositing it outside the active electrode area. An interesting, novel option represents industrial ink-jet printing. This technique is characterized by a high speed of layer production and, at the same time, precise deposition of the catalyst to the desired locations. It allows not only to cover exactly the active zone of the cell, but also gradient loading of the catalyst according to the corresponding reaction intensity. Accordingly, this technique is recently attracting significant interest of the scientific and industrial community around the globe.

Critical aspect of the application of ink-jet printing for the catalyst layer production are properties of the resulting membrane-electrode-assembly (MEA). This contribution focusses on comparison of performances of MEAs produced by the ink-jet printing and by depositing ultrasonically-dispersed catalyst ink of the identical composition on the surface of the membrane. The tests of the produced MEAs in a laboratory fuel cell have surprisingly shown superior performance of the ink-jet produced catalytic layer. Performance comparable to those reached using MEAs prepared by depositing of the ultrasound dispersed catalytic ink was achieved by Pt load reduced down to one third. To gain deeper understanding of the behaviour observed, FIB-SEM and TEM tomography were used to analyse internal structure of both catalyst layers. The results indicate more compact, les porous structure of the ink-jet produced catalyst layers. At the same time, it shows slightly higher electronic conductivity comparing to the more voluminous catalyst layer produced by ultrasound dispersion. In the next step, transport parameters were evaluated theoretically for both types of catalyst layer on the basis of replicas of structure obtained using tomography images. Results of this analysis were validated experimentally by means of catalyst layer electron conductivity, as well as its permeability for gaseous reactants. Whereas electronic conductivity values show very good agreement, in the case of permeability, experimentally determined values significantly exceeds those determined theoretically. This observation is explained by cracks formed in the catalyst layer during drying. In the operating fuel cell these cracks have no significant impact on the reactants transport unless the distance between the cracks is comparable to the catalyst layer thickness. In performed permeation experiment, however, flux through the cracks clearly dominated over the porous structure of catalyst layer itself. Trial to correct the results for the viscose flow was, unfortunately, not successful.

Present contribution provides a novel insight into impact of the catalyst deposition techniques on the internal structure of the active part of the fuel cell gas diffusion electrode and thus on the resulting performance of produced MEA.

Acknowledgements

This work was supported by the project "The Energy Conversion and Storage", funded as project No. CZ.02.01.01/00/22_008/0004617 by Programme Johannes Amos Comenius, call Excellent Research. This project has received funding from the European Union's Horizon 2020 research and innovation programme under grant agreement No 958174. This project is co-financed from the state budget by the Technology agency of the Czech Republic under the M-ERA.Net Programme, project No. TH80020006. This project is co-financed with tax funds on the basis of the budget passed by the Saxon state parliament.

The use of reconstructive surgery and conservative management for a large skin defect following a bite injury in a domestic cat

M. Kožár[a]*, B. Šišková[a]

[a] University of Veterinary Medicine and Pharmacy in Košice, 041 81 Košice, Slovak Republic

This clinical case demonstrates the primary use of conservative management following the repair of extensive necrotization of the skin and subcutaneous tissue as a complication of a domestic cat bite by a rat. On clinical examination, a culture sample was collected from the wound site for bacteriological culture with the development of antibiotic resistance. On microbiological culture, Staphyloccocus haemolyticus was confirmed with subsequent targeted antibiotic therapy with a combination of amoxicillin and clavulanic acid (Synulox, Zoetis, Czech Republic) at a dose of 20 mg/kg two times per day for 38 days. The patient had skin damage and necrotization on the lateral surface over the scapula extending to the elbow joint, where the defect extended to the medial forearm area. Fairly significant skin damage was also present over the carpal joint area extending to the dorsal surface of the fingers. The first steps of therapy were mechanical removal of the necrotic skin. After mechanical debridement, application of collagen cover (Suprasorb C, Lohmann & Rauscher, Slovakia) was chosen with the expectation of granulation bed formation. The wound was covered with an external dressing with bandaging every 48 hours for 24 days. This study describes the active effect of collagen covering on rapid wound closure in the form of retraction of the wound edges and formation of granulation tissue at the base of the wound. However, despite the rapid wound healing process, the skin defect represented a large lesion with no superficial overlying by absent structure; therefore, a rotational skin flap was used in the area of the lateral surface of the elbow. The skin flap represented a suitable substitute for the absent tissue with overgrowth of the skin defect with hair and effectively shortened the length of therapy while closing the defect at this location. Topical application of collagen and mastic was continued on the distal limb. Bandages were applied every 5 days during this period. Overall therapy was supported throughout by topical application of sodium hyaluronate and silver salt sulfadiazine (Ialugen Plus, IBSA Farmaceutici Italia Srl, Italy) applied at each bandaging.

The total healing time of the skin defect from the primary examination was 38 days, consisting of conservative wound management with support of the granulation phase of wound healing and subsequent transfer of a rotational type skin flap obtained from the distal part of the rib cage to the 12 rib area and overlapping of the skin defect with granulation tissue overgrowth over the entire wound bed. The highlight of the whole therapy is the effect of collagen on the healing process of the skin defect with the possibility to restore functionality and aesthetic closure of the skin defect.

Acknowledgements

This work was supported by the project APVV-20-0278 of the Slovak Research and Development Agency.

8th International Conference on Novel Materials Fundamentals and Applications
High Tatras, 13.-16.10.2024

Engineering of Biomaterials – the Pillar of Modern Bone Regenerative Medicine

A. Przekora[a]*

[a] Department of Tissue Engineering and Regenerative Medicine, Medical University of Lublin, Chodzki 1 Street, 20-093 Lublin, Poland
*agata.przekora@umlub.pl

Background

In some cases, such as extensive bone defects, osteoporotic fractures or bone defects/fractures in oncological patients who underwent radiotherapy, regeneration of bone tissue is hindered and requires application of modern strategy that uses implantable biomaterials as scaffolds for stem cells and osteoprogenitor cells in order to temporarily maintain function and growth of bone tissue during the process of its regeneration. Biomaterials for bone tissue engineering applications should primarily provide interconnected, macroporous, and three-dimensional (3D) structure which is favorable to growth, proliferation, and differentiation of osteoblasts and osteoprogenitor cells [1]. Within our studies we have developed and characterized various bioceramic-based biomaterials for potential applications in regenerative medicine. Produced biomaterials were subjected to comprehensive microstructural, mechanical, and biological characterization [2]–[6].

Methods

Biomaterials for bone regenerative medicine applications were produced using hydroxyapatite (HA) as ceramic phase and biopolymers (chitosan, agarose, β-1,3-glucan) as organic phase. Porosity (total, open, closed) of the biomaterials was assessed using microcomputed tomography (microCT). Surface topography was visualized using scanning electron microscope (SEM) and mechanical parameters were determined in a compression test. Bioactivity of the biomaterials (apatite-forming ability) *in vitro* was performed in accordance with ISO 23317 procedure (2014) by immersion of the materials in the simulated body fluid (SBF) and analysis using SEM equipped with EDS detector to calculate the Ca/P atomic ratio (confirmation of the presence of apatite crystals). Biocompatibility *in vitro* was assessed using osteoblasts and mesenchymal stem cells by evaluation of cell adhesion, proliferation, and osteogenic differentiation on the biomaterials. Moreover, osseointegration process was determined using *ex vivo* human bone explant model.

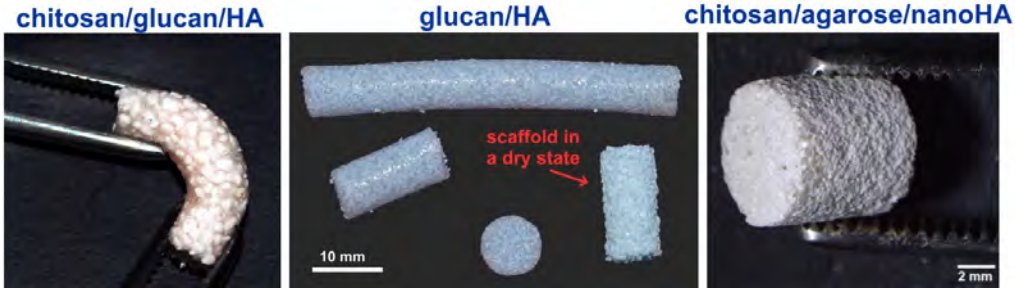

Fig. 1 Developed biomaterials for bone regenerative medicine applications.

Results

Three various bone scaffolds were developed: chitosan/β-1,3-glucan/HA, β -1,3-glucan/HA (Patent PL no. 229329, 2018), and chitosan/agarose/nanoHA (Patent PL no. 235822, 2020) (Figure 1). Among all developed biomaterials,

chitosan/agarose/nanoHA scaffold shows the most desired microstructural properties (surface roughness, high macroporosity, desired compressive strength value). All scaffolds exhibit high bioactivity and biocompatibility *in vitro* (Figure 2). The scaffolds are very promising implantable materials as they favor growth of osteoblasts and stem cells, promote cell proliferation and bone forming processes thereby accelerating bone regeneration [2]–[6]. Moreover, it was proven using *ex vivo* model that chitosan/β-1,3-glucan/HA biomaterial has the ability to support osseointegration process (Figure 3) [7].

Conclusion

It was proven using *in vitro* cellular models that developed biomaterials possess great potential as an innovative tissue engineered products (TEPs) to be applied for reconstruction or regeneration of bone tissue. In practice, produced biomaterials could be used in the orthopedic surgery departments as implantable materials (bone substitutes for implantation without pre-seeding with cells) allowing for acceleration of regeneration process at the site of implantation or as modern bone scaffolds initially seeded with osteoprogenitor cells isolated from patient organism to generate so-called living graft under *in vitro* conditions. Implantation of such TEPs at the site of bone defect would significantly accelerate bone regeneration, and thus would make even shorter the time of convalescence of the patient. The bone scaffolds used as TEPs can be an alternative to autografts and allografts.

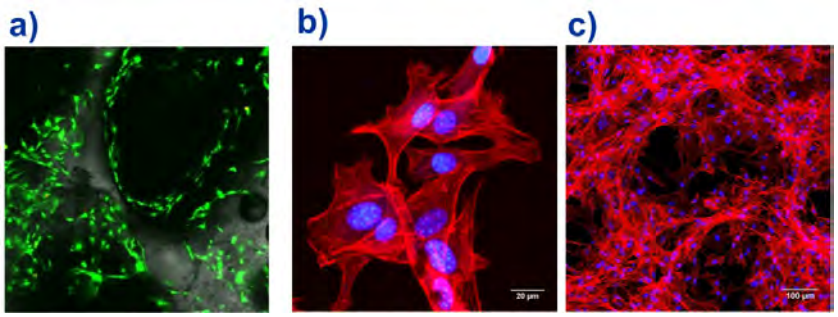

Fig. 2 Biocompatibility tests on biomaterials: a) viable (green fluorescence) osteoblasts on chitosan/β-1,3-glucan/HA scaffold [4]; b) good osteoblast adhesion and spreading as well as c) excellent osteoblast growth on chitosan/agarose/nanoHA scaffold (red fluorescence is cell cytoskeleton, blue are cell nuclei) [2].

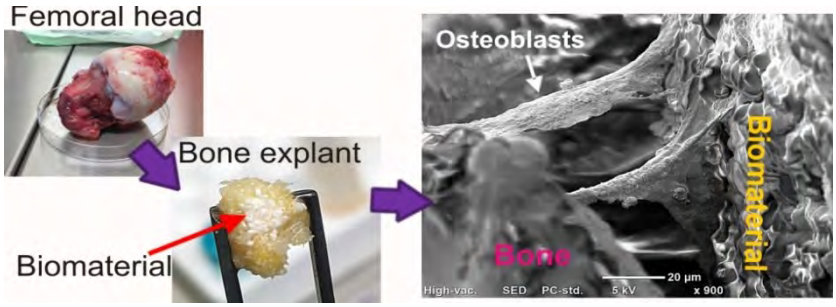

Fig. 3 Osseointegration of the chitosan/β-1,3-glucan/HA biomaterial with human bone assessed *ex vivo* [7].

Acknowledgements

The studies were funded by the National Science Centre (NCN) in Poland within OPUS 16 grant no. UMO-2018/31/B/ST8/00945 and OPUS 22 grant no. UMO-2021/43/B/NZ7/00447. The research was partially also supported by the Ministry of Science and Higher Education in Poland within the statutory activity of the Medical University of Lublin (DS 3 and DS 630 projects).

References

[1]A. Przekora, "The summary of the most important cell-biomaterial interactions that need to be considered during in vitro biocompatibility testing of bone scaffolds for tissue engineering applications," *Mater. Sci. Eng. C*, vol. 97, 2019.

[2]P. Kazimierczak, A. Benko, M. Nocun, and A. Przekora, "Novel chitosan/agarose/hydroxyapatite nanocomposite scaffold for bone tissue engineering applications: Comprehensive evaluation of biocompatibility and osteoinductivity with the use of osteoblasts and mesenchymal stem cells," *Int. J. Nanomedicine*, vol. 14, 2019.

[3]P. Kazimierczak, A. Benko, K. Palka, C. Canal, D. Kolodynska, and A. Przekora, "Novel synthesis method combining a foaming agent with freeze-drying to obtain hybrid highly macroporous bone scaffolds," *J. Mater. Sci. Technol.*, vol. in press, 2020.

[4]A. Przekora and G. Ginalska, "Addition of 1,3-β-d-glucan to chitosan-based composites enhances osteoblast adhesion, growth, and proliferation," *Int. J. Biol. Macromol.*, vol. 70, pp. 474–481, 2014.

[5]A. Przekora and G. Ginalska, "Enhanced differentiation of osteoblastic cells on novel chitosan/β-1,3-glucan/bioceramic scaffolds for bone tissue regeneration," *Biomed. Mater.*, vol. 10, no. 1, 2015.

[6]K. Klimek, A. Przekora, A. Benko, W. Niemiec, M. Blazewicz, and G. Ginalska, "The use of calcium ions instead of heat treatment for β-1,3-glucan gelation improves biocompatibility of the β-1,3-glucan/HA bone scaffold," *Carbohydr. Polym.*, vol. 164, 2017.

[7]A. Przekora, P. Kazimierczak, and M. Wojcik, "Ex vivo determination of chitosan/curdlan/hydroxyapatite biomaterial osseointegration with the use of human trabecular bone explant: New method for biocompatibility testing of bone implants reducing animal tests," *Mater. Sci. Eng. C*, vol. 119, 2021.

Advancing Bone Tissue Engineering with Polyol-Citrate Added Bioactive Composites

T. Sopcak[a]*, L. Medvecky[a], T. Csanádi[a], F. Kromka[a], M. Giretova[a], R. Stulajterova[a], R. Sedlák[a], M. Streckova[a], K. Balázsi[b]

[a] Institute of Materials Research of SAS, Watsonova 47, 04001 Kosice, Slovak Republic
[b] Centre for Energy Research, Institute of Technical Physics and Materials Science, Konkoly-Thege M. Str. 29-33, 1121 Budapest, Hungary
*tsopcak@saske.sk

Bone tissue engineering is one of the most rapidly advancing fields in materials science, driven by the growing prevalence of musculoskeletal disorders affecting bones and joints. As a result, biomaterials developed for this field must meet essential requirements to mimic the physical, chemical, and biomechanical properties of the bone tissue's extracellular matrix, ensuring successful integration and functionality [1]. Common biomaterials used in bone tissue engineering include bioceramics, polymers, and their composites, which can effectively regenerate and restore damaged bone tissue [2]. Hydroxyapatite (HAp) bioceramics is the primary mineral component of bone tissue, making biomaterials based on hydroxyapatite or other calcium phosphates (CaP) a suitable choice for bone replacement materials. However, CaP biomaterials are limited by their relatively low mechanical strength due to inherent porosity and brittleness, as well as their slower degradation and resorption rates compared to natural hydroxyapatite in bone tissue. In recent decades, these drawbacks have been addressed by incorporating biodegradable polymers, such as polylactides, into the ceramic matrix [3].

More recently, a new class of biodegradable thermoset polymers with elastomeric properties has been developed through the simple esterification of polyhydroxy alcohols, such as diols or polyols, with citric acid in a catalyst-free reaction over a wide temperature range, resulting in inexpensive, biodegradable polymers with improved processability and mechanical properties compared to thermoplastic polylactides. Among all polyol citrates, poly(1,8-octanediol-co-citrate) (POC) is the first thermoset polyester in the polyol-citrate family, extensively studied primarily for soft tissue repair and engineering due to its soft and viscoelastic properties. For bone tissue engineering applications, POC has been combined with bioactive inorganic materials, such as HAp and bioactive glass, to enhance mechanical properties and provide the necessary bioactivity to mimic the natural environment of bone tissue. The relatively long chain length of POC increases its hydrophobicity, prompting researchers to develop other polyol citrates with significantly higher water wettability and hydrophilicity, thereby promoting improved cell and tissue interactions [4].

Motivated by this, our research group aimed to develop glycerol-citrate (G-C) polyester-modified calcium phosphate cements, with the G-C polyester incorporated into the cement matrix through infiltration in an ethanolic solution. In this lecture, we present our recent developments regarding the chemical, structural, and biological interactions between the G-C elastomer and the cement matrix. Additionally, we discuss in detail the strengthening mechanisms at the polymer/cement interface on the nano- and micrometer scales, which have been rarely explored in similar studies.

Acknowledgements

This work was funded by the EU NextGenerationEU through the Recovery and Resilience Plan for Slovakia under the project No. 09I03-03-V04-00133, by the Slovak Grant Agency of the Ministry of Education of the Slovak Republic and the Slovak Academy of Sciences, Project No. 2/0039/24, by the Slovak Research and Development Agency under contract No. APVV-20-0184, APVV-20-0299 and APVV-20-0278 and by the Slovak - Hungarian bilateral cooperation HAS-SAS-2022-1. T.Cs. is grateful for the funding of the programme “Support for Seal of Excellence projects” of the Slovak Academy of Sciences via the project of Strengthecs, H2020-MSCA-IF

References

[1] A.R. Amini, C. T. Laurencin and S. P. Nukavarapu, "Bone Tissue Engineering: Recent Advances and Challenges," *Crit. Rev. Biomed. Eng.*, vol. 40, no. 5, pp.363-408, Sep. 2013, doi: 10.1615/critrevbiomedeng.v40.i5.10

[2] P. Dec, A. Modrzejewski and A. Pawlik, "Existing and Novel Biomaterials for Bone Tissue Engineering" Int. J.Mol.Sci., vol. 24, no. 1, pp. 1-14, Dec. 2022, doi: 10.3390/ijms24010529

[3] X. Carette, R. Mincheva, M. F. Gonon and J.M. Raquez, "A simple approach for a PEG-b-PLA-compatibilized interface in PLA/HAp nanocomposite. From the design of the material to the improvement of thermal/mechanical properties and bioactivity," *J. App. Pol. Sci.*, vol. 139, pp. 1-12, Apr. 2022, doi.org/10.1002/app.52807

[4] M. Wang, P. Xu and B. Lei, "Engineering multifunctional bioactive citrate-based biomaterials for tissue engineering," *Bioact.Mater.*, vol. 19, pp. 511-537, May. 2022, doi: 10.1016/j.bioactmat.2022.04.027

Novel Catalyst for Hydrogen Evolution Reaction

M. Strečková[a]*, E. Matisová[b], A. Fedoročková[b], A. Gubóová[a], R. Oriňaková[c]

[a] Institute of Materials Research, Slovak Academy of Sciences, Watsonova, 040 01, Kosice, Slovak Republic
[b] Faculty of Materials, Metallurgy and Recycling, Technical university of Košice, Slovak Republic
[c] Institute of Chemistry, Faculty of Science, P.J. Safarik University, Moyzesova 11, 040 01, Kosice, Slovak Republic
*mstreckova@saske.sk

Hydrogen is regarded as a clean energy source when compared to fossil fuels. Notable methods for converting water into H_2 using renewable energy include electrochemical and photoelectrochemical water splitting. However, catalysts are essential for hydrogen production from water. At present, platinum and platinum group metals are viewed as the most effective catalysts for the hydrogen evolution reaction (HER).

This poses a major challenge to electrochemical hydrogen production via water splitting and impacts the economic feasibility of electrolyzers. As a result, there has been significant interest in creating catalysts that do not rely on noble metals but still offer high efficiency and durability. Transition metal compounds such as sulfides, phosphides, nitrides, carbides, and hydroxides are being explored as potential alternatives to Pt/C catalysts. For advancing hydrogen technology, it is crucial that the catalysts have different morfologies with a high specific surface area and ample active sites. Recent studies have shown that metal phosphides demonstrate catalytic efficiency comparable to that of platinum catalysts [1-4].

The goal of this study was to create cost-effective electrocatalysts for the hydrogen evolution reaction (HER) in alkaline conditions, focusing on different morphologies, namely hollow spherical particles prepared by the spray-drying method (SDM), compared to MoFeP particles obtained using the sol-gel(SG) method. The new catalysts in the form of hollow spheres were developed based on bimetallic MoFeP and trimetallic MoFeNiP and MoFeCoP phosphides prepared through the SDM method. We investigated three different combinations of transition metals for their electrocatalytic activity by standar voltammetry methods like (LSV, CV or EIS analysis) and compared their performance to that of platinum, a leading electrocatalyst. Stability tests were performed using chronoamperometry measurements.

The novel metallic phosphide catalysts were prepared in a citric acid (CA) environment. All nitrates were dissolved in a 4M citric acid solution, and the molar ratio of salts was maintained at CA : Fe : Mo : P = 2 : 0.5 : 0.5 : 0.5, corresponding to the stoichiometric ratios of the final bimetallic MoFeP and trimetallic MoFeNiP and MoFeCoP phosphides. Individual compounds were added slowly to the citric acid solution until complete homogenization was achieved. After homogenization, the solution was sprayed into small droplets which were dried in a stream of hot air to form a fine powder. A spray dryer (TEFIC Biotech; TFS-2L) was utilized to produce the powdered material. Fig. 1 illustrates a schematic representation of the spray dryer. The spray-dried samples were subsequently heat-treated at 100°C in an argon atmosphere, followed by calcination at 650°C in a hydrogen atmosphere for 2 hours to produce the final black powder phosphides (Fig. 2b).

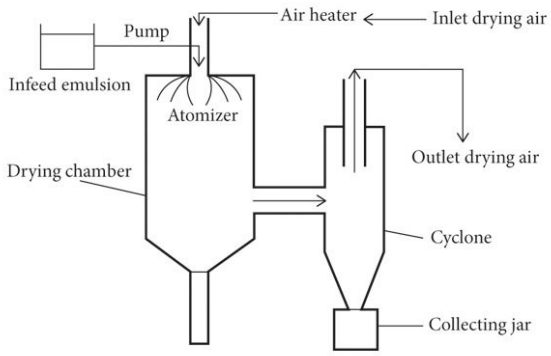

Fig. 1 Schematic representation of the spray dryer (SDM method).

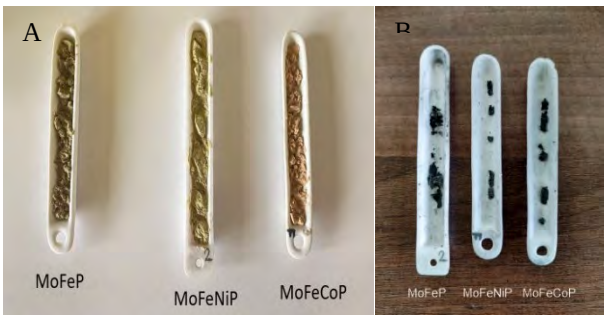

Fig. 2 MoFeP, MoFeNiP and MoFeCoP powders
(a) after spray drying (b) after calcined at 650 °C.

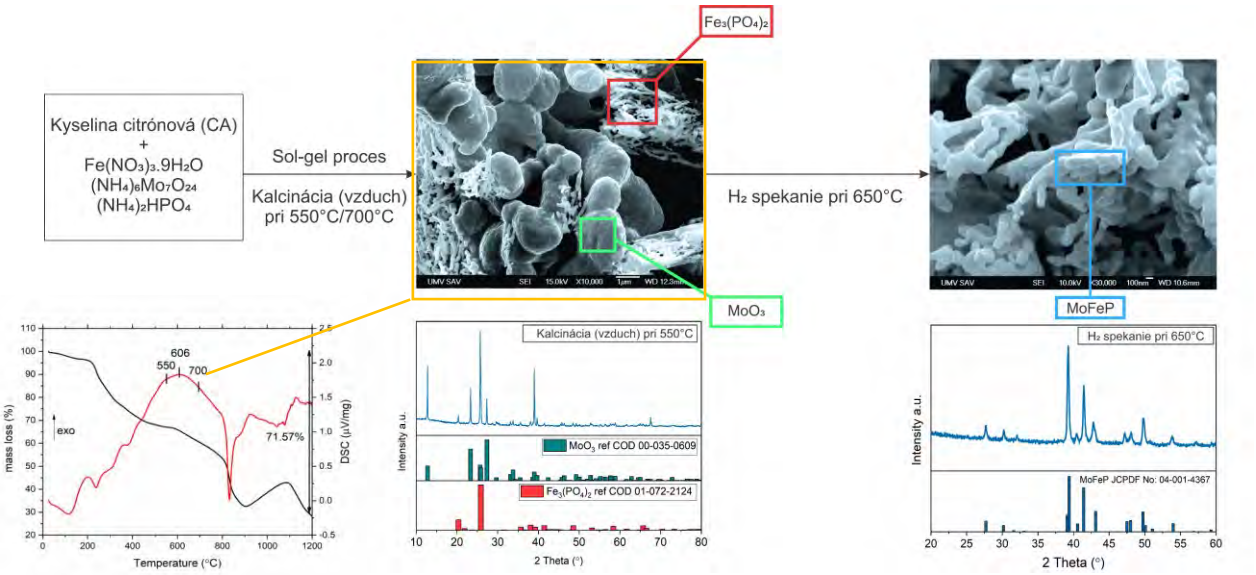

Fig.3 Schematic illustration of the preparation powdered MoFeP via sol-gel (SG) method followed by calcination at 500°C in air/2h and sintering in reduction atmosphere at 650°C/2h.

Figure 3 illustrates the preparation of MoFeP powder based on TG/DSC analysis, which shows an exothermic peak with a maximum at 606°C. After the sintering process in air, XRD analysis confirmed the presence of two different oxide phases, $Fe_3(PO_4)_2$ and MoO_3. These phases transform into the final MoFeP structure after sintering in a reduction atmosphere at 650°C for 2 hours. The XRD diffractogram of the final MoFeP powder exhibits an orthorhombic structure with a space group of Pnma, in accordance with ICDD 04-001-4637 (a = 5.922, b = 3.663, and c = 6.79).

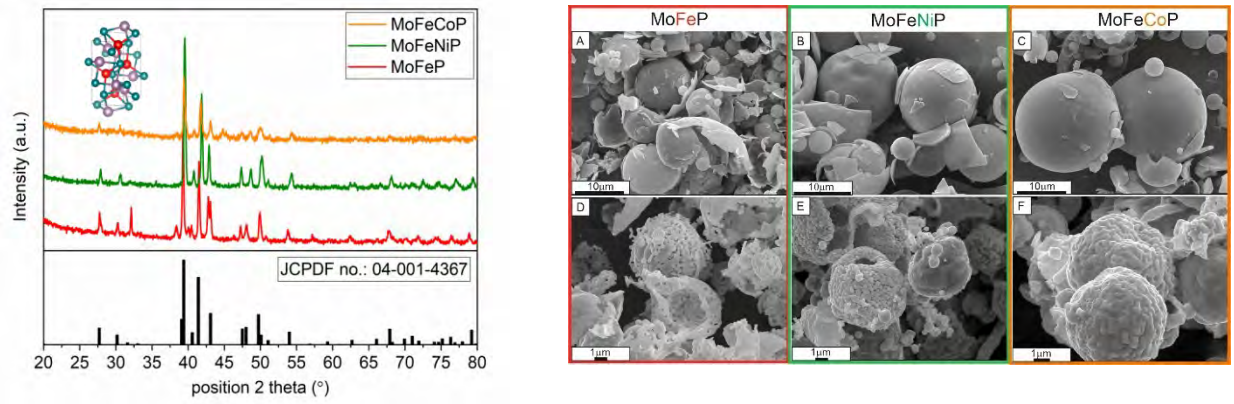

Fig.4 XRD pattern of MoFeP, MoFeNiP and MoFeCoP prepared using spray-drying followed by calcination. SEM image of hollow spherical particles immediately after the SDM method (a,b,c), and after reduction (d,e,f).

The XRD pattern in Figure 4 illustrates the phase structures of the final MoFeP, MoFeNiP, and MoFeCoP samples heat-treated at 650°C in a reduction environment. The XRD pattern corresponding to the stoichiometric MoFeP phase was detected for all prepared samples, implying that Ni and Co were successfully incorporated into the orthorhombic structure with space group Pnma, in accordance with ICDD 04-001-4637 (a = 5.922, b = 3.663 and c = 6.79). The most intesive peak at 37.9 (321) plane in comparison with peak at 42.3 (411) confim thermodynamically stabile facet of the (321) plane. SEM images in Figs. 4 (a, b, c) point to a regular spherical shape of hollow particles in all samples obtained immediately after the SMD method. However, the change after the reduction is quite obvious. The spherical morphology of particles with a hollow interior was preserved Figs. 4(d,e,f). However, the particle diameter was approximately halved, while the shell thickness increased. The morphology of the resulting MoFeP, MoFeNiP, and MoFeCoP particles was formed with irregular shapes grains joined into regular globular particles.

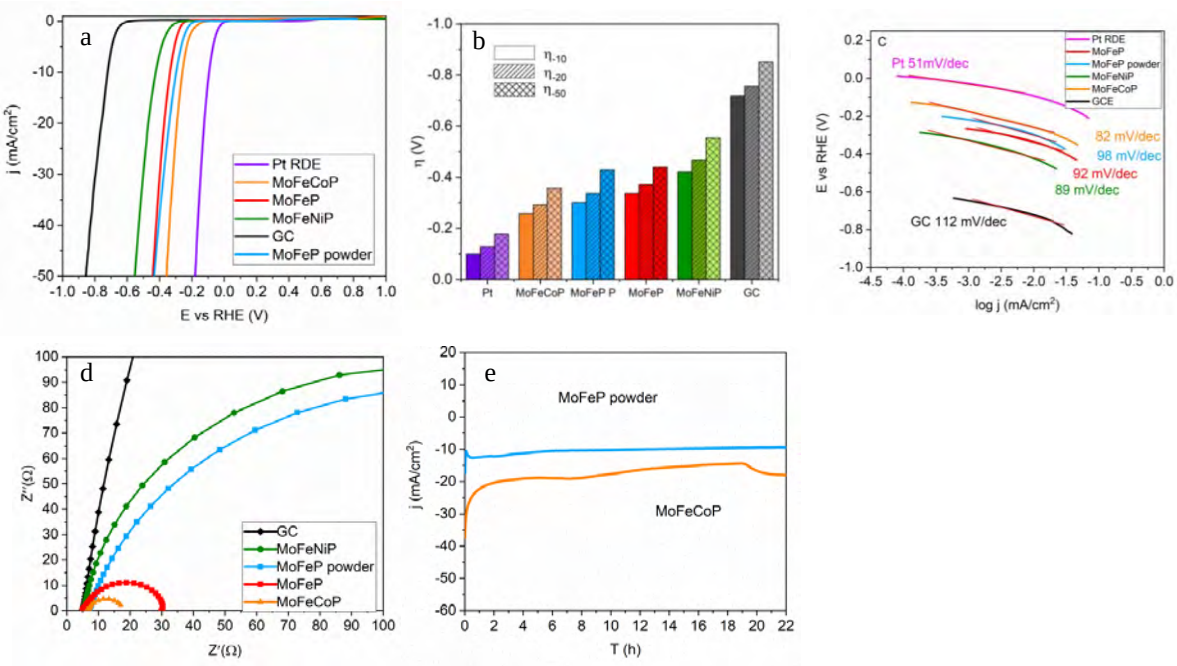

Fig.5 Electrochemical measurements of prepared catalysts in 1M KOH (a) LSV, (b) column graphs for different overvolatages, (c) Tafel slopes, (d) EIS analysis, (e) chronoamperometry measurement for 22 h at E vs RHE -385 mV. Note the powdered samples were prepared by SG method and spheres by SDM method.

The electrocatalytic activity and stability of the synthesized catalysts prepared using sol gel method (denoted as SG) and spray-draying method (denoted as SDM) toward HER in a 1M KOH environment were investigated using LSV measurements and EIS analysis (Fig. 5). The HER activity of phosphides was compared with that of the bare GC electrode and a commercial Pt electrode. As expected, the bare GC electrode showed the high overpotential of -718 mV at a cathodic current density of -10 mA/cm² (η-10), while the Pt electrode displayed the best HER activity among all samples of -100 mV at η-10. As shown in Fig. 5a and b, the overpotentials η_{-10} of the prepared samples increased in the order of MoFeCoP (SDM) 285 mV < MoFeP (SG) 295mV< MoFeP(SDM) 337 mV < MoFeNiP(SDM) 421 mV, indicating the highest activity of the phosphide doped by Co. However, it is evident that the overpotentials for all the prepared catalysts are very similar, despite the different morphologies of the powders prepared using SG (Fig.3) and SDM (Fig.4) method. Similarly, the very similar Tafel plots for all prepared samples, MoFeCoP(SDM), MoFeP(SG), MoFeP(SDM) , and MoFeNiP(SDM), with values of 82 mV/dec, 96 mV/dec, 92 mV/dec, and 89 mV/dec, respectively, obtained from the polarization curves (Fig. 5c), indicated that the rate-determining step in the hydrogen reduction mechanism is electrochemical desorption, specifically the Heyrovsky reaction ($H_{ads} + e^- + H_2O \rightarrow H_2 + OH^-$). On the other hand, the results of the EIS analysis (Fig. 5e) show that the charge transfer resistance of the spherical MoFeCoP phosphide catalyst achieved the highest charge transfer kinetics from all compared samples. Chronoamperometry measurements at a constant potential of -385 mV vs. RHE for 22 h were used to evaluate the stability of the most active catalytic sample, MoFeCoP (SDM) and MoFeP(SG).

Acknowledgements

This work was financially funded by the EU NextGenerationEU through the Recovery and Resilience Plan for Slovakia under the project No. 09I03-03-V04-00109 and by the grant of the Slovak Research and Development Agency provided under the contract No. APVV-20-0299 and by the grant of the Slovak Academy of Sciences and The Ministry of Education, Science, Research, and Sport of the Slovak Republic provided under the contracts No. VEGA 2/0027/23, 1/0095/21 and 1/0503/23.

References

[1] F. Zhou, G.Liu, Ch. Wang, J. Wang, *Rare Mat.* 40 (2021) 3375.

[2] H. Yin, F. Rong, Y. Xie, *Int. J. of Hydro. Energy* 52 (2024) 350.

[3] K. Bhunia, M. Chandra, S. Sharma, D. Pradhan, S. Kim, *Coord. Chem. Rev.s* 478 (2023) 1.

[4] S. Fang, T. Chou, S. Samireddi, L. Chen, W. Chen, *R. Soc. Open Sci.* 4 (2017) 1.

Tracing the Origins of the Cavalry Armour Collection Exhibited at the Palace Armoury in Valletta, Malta: A Materiographic Examination

L. Zerafa [a], M. Pizzuto[b], J. Bezzina [a], A. Sciberras, R. Howard, M. Grima[a], R. Cassar [a], D. A. Vella[a]*

[a] Department of Metallurgy and Materials Engineering, Faculty of Engineering, University of Malta, Msida, MSD 2080, Malta
[b]Faculty of Medicine and Surgery,University of Malta, Msida, MSD 2080, Malta
*daniel.vella@um.edu.mt

This study deals with a physical and materiographic examination of cavalry armour suits from the collection at the Palace Armoury within the Grandmaster's Palace in Valletta, aiming to identify the origins of these artefacts. Stylistically, the cavalry armour suits align with Italian designs from the early 1600s (circa 1610-1620). An armourer's mark that takes the form of a castle on a few armour pieces may indicate the workshop of the relatively obscure *Maestro del Castello*. However, there is no written documentation confirming the armour's origin or the attribution of the armourer's mark. The cavalry armour is particularly intriguing due to (i) the lack of recorded evidence for its inclusion in the Palace collection and (ii) the absence of documented cavalry battles in Malta after 1600. Given Malta's small size and unsuitable terrain for cavalry warfare, coupled with the impracticality of a full armour suit and closed helmet in the island's hot climate, consensus among curatorial staff is that these armour suits may have been purchased for offshore military campaigns.

In the first part of this study, three randomly selected cavalry armour suits, comprising 24 pieces, were physically examined to assess their attributes, including plate thickness and surface hardness. The second part involved selective invasive sampling of six armour pieces from the original 24. Small metal fragments, a few millimeters in size, were extracted from three breastplates featuring lance rests and three left tassets—pieces designed to protect the lower limb and composed of multiple lames for flexibility. Each tasset contributed two fragments from lame numbers 1 and 9. The cut out fragments were cold mounted in epoxy resin ground and polished for metallographic analysis. Results revealed that the armour was mostly hot-worked from either wrought iron or low carbon steel, with observed microstructures being either completely ferritic, ferrite-pearlite, or predominantly pearlite. Of note, two tasset pieces exhibited similar metallurgical characteristics, suggesting perhaps that they were manufactured by the same armourer. Using a variable pressure scanning electron microscopy coupled with an energy dispersive spectrometer, the concentrations of minor elements in the metal matrix and slag inclusions were determined against certified reference materials.

The findings allowed for the armour pieces to be distinguished according to the metal extraction process, namely the single-step Bloomery process and the indirect two-step process involving a blast furnace and finery furnace. Elemental biplots of minor elements in the slag inclusions from different lames of the same tasset reinforced the hypothesis that a single metal sheet was used in their production.

A statistical analysis of the chemical signatures of the slag inclusions present within the Palace cavalry armour, compared with other European armour of known origin through Principal Component Analysis, indicates a likely Italian provenance. However, confirming this requires further comparison of trace element signatures, which can be detected using techniques such as LA-ICP-MS.

Fig. 1 Complete suit of cavalry armour showing breast plate with lance rest and tassets.

Abstracts

Investigation of Conductive Properties of Nanocellulose

E. Bencúrová[a]*, T. Dandekar[a]

[a] University of Würzburg, Germany
*elena.bencurova@uni-wuerzburg.de

Introduction

Cellulose, the most abundant natural polymer, is a linear biopolymer composed of anhydroglucose units, varying in degrees of polymerization. Depending on its source and processing, cellulose can consist of several thousand glucose units. The extensive intra- and intermolecular hydrogen bonds within cellulose allow it to form strong microfibrils, presenting significant potential for applications in food, cosmetics, medicine, and technical fields. Cellulose's renewability, biocompatibility, and non-toxicity offer distinct advantages over synthetic materials in electronic devices.

In recent years, cellulose and nanocellulose have gained significant attention in electronics [1-3]. A recent study demonstrated a cellulose organic field-effect transistor (OFET) using either a cellulose thin film or a semiconducting layer coated onto a cellulose dielectric [4]. The demand for energy-efficient portable electronic devices, like mobile phones and laptops, has prompted studies toward low power consumption, high carrier mobility, and reduced off-state current in unipolar n-type field-effect transistors (FETs).

While OFETs present promising solutions [5], they have disadvantages, such as low intrinsic carrier mobility and loosely pinned off-state current, leading to a poor current on/off ratio compared to inorganic FETs. This results in a decreased noise margin, higher power consumption in standby mode, and lower processing power. In contrast, inorganic n-type FETs exhibit high carrier mobility, a high current on/off ratio, and well-defined saturation characteristics.

Nanocellulose (NC) emerges as a versatile material easily produced and integrated into a nanocellulose chip. Material itself if cheap, it easy to obtain and process, as well as ecologically friendly. NC can be obtained from the various natural or agricultural sources, such as plants, bacterial or even the waste in the food processing [6]. Its unique electronic properties, whether in isolation or combined with graphene, enable it to function as a conductor, insulator, or semiconductor. Furthermore, nanocellulose serves as an optimal composite material and support for green paper electronics. For instance, ink-printed green electronics, including transistors, can be advantageously printed on nanocellulose supports. A significant advancements have been made in transforming nanocellulose into both p-type and n-type semiconductor materials. For instance, the work by Farahani et al. (2022)[7] successfully demonstrated the development of p-type semiconducting nanocellulose, while Yu et al. (2021)[8] reported the creation of n-type semiconducting nanocellulose. These breakthroughs represent a crucial step forward in the functionalization of nanocellulose for electronic applications.

Despite these promising developments, the application of these semiconducting nanocellulose materials in transistor fabrication remains largely unexplored. However, the successful conversion of nanocellulose into both p-type and n-type materials strongly suggests that a fully complementary metal-oxide-semiconductor technology based on nanocellulose is within reach. Such a technology would leverage the unique properties of nanocellulose, including its flexibility, biocompatibility, and renewability, potentially paving the way for sustainable and biodegradable electronic devices. The realization of complementary p-type and n-type transistors using nanocellulose could lead to the development of all-organic electronic circuits with enhanced performance and lower power consumption, thereby expanding the potential applications of nanocellulose in the field of organic electronics.

Materials and Methods

Nanocellulose Preparation: Bacterial nanocellulose was derived from a Kombucha membrane (SCOBY, a symbiotic culture of bacteria and yeast). The culture was cultivated in a tea infusion with 10 g of black tea and 10% sugar steeped for 10 minutes in 1 L of boiling water. After cooling to ambient temperature, 50 ml of medium from the previous culture was added. The SCOBY was added, and the glass bottle was covered with lightweight paper. The culture matured at room temperature for 30 days. The SCOBY was washed with distilled water and incubated for 24 hours in 1M NaOH to remove impurities and microorganisms. The nanocellulose was blended, filtered through a 0.45 micrometer filter under vacuum, and rinsed to reach neutral pH.

For the conductive nanocellulose composite, graphene oxide (2mg/ml) was added to the bacterial nanocellulose and mixed using a magnetic stirrer at room temperature for 24 hours. The nanocellulose was filtered to remove excess water, and dried at 60°C for 12 hours. Measurements were performed using a Laqua Twin (Horiba, Japan) according to the manufacturer's instructions. The samples were imaged in a JSM-7500F field emission scanning electron microscope (SEM; JEOL, Tokyo, Japan) with an acceleration voltage of 5 kV, a probe current of 0.3 nA, and a working distance of 6.0 mm.

Results

Nanocellulose can be customized for a wide range of applications, including chip design, through various primary sources and processing methods. This material exhibits diverse optical properties, from transparent to non-transparent forms, and can be processed into different physical states such as wet gel, aerogel, and solid stage. Bacterial nanocellulose has minimal environmental impact during production and processing, making it more sustainable compared to wood-sourced nanocellulose.

We investigated the electrical properties of nanocellulose composites, focusing on graphene oxide incorporation. Previous work identified iodine-doped nanocellulose as a suitable conductive material, but due to environmental toxicity, graphene oxide was explored as a more suitable alternative . The treatment with graphene oxide significantly enhances the conductivity of nanocellulose, which can be observed from the experiment measuring the conductivity of GO-nanocellulose (GO-NC) in the liquid phase (panel f). The data from panel f reveals that untreated nanocellulose exhibits relatively low conductivity, whereas GO-treated nanocellulose displays a marked increase in conductivity. Specifically, the untreated nanocellulose shows a conductivity of approximately 0.1 S/m, while GO-treated nanocellulose reaches up to 200 S/m, demonstrating its transition towards more conductive and semiconductive properties. (Figure. 1). The panel g outlines the conceptual design of a transistor, where GO-NC layers serve as the active channel. In this model, the GO-treated nanocellulose acts as a semiconductive layer, modulating current flow between the source and drain, while untreated nanocellulose and doped nanocellulose (either N- or P-doped) are also integrated into the design to optimize performance. This arrangement highlights the potential of GO-NC as a promising material in flexible electronics and other applications requiring tunable conductivity.

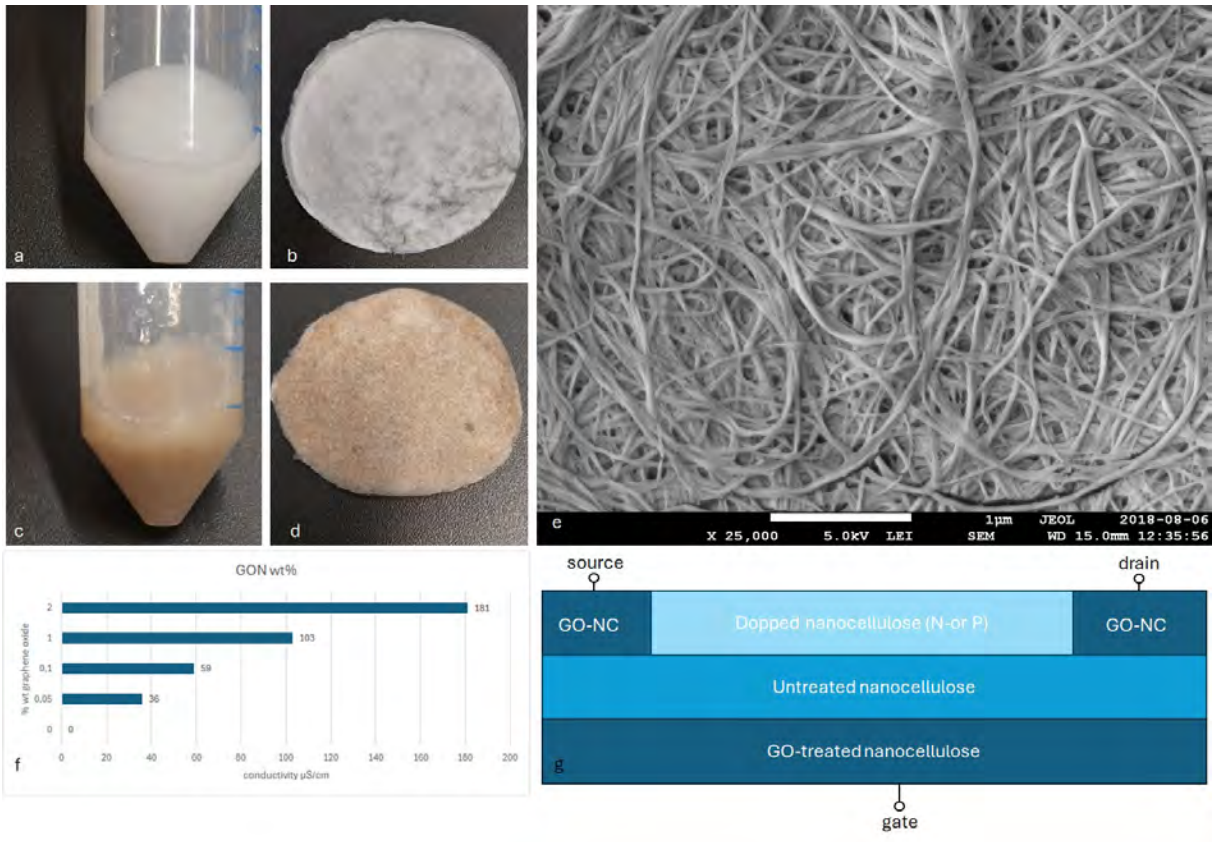

Fig. 1 Fabrication and Conductive Properties of Nanocellulose. Panels (a) and (b) depict non-conductive nanocellulose, while panels (c) and (d) show nanocellulose treated with graphene oxide. Panels (a) and (c) illustrate the hydrogel form, and panels (b) and (d) display the dried nanocellulose, on the panel e is depicted fine structure of the NC captured by scanning electron microscope. Panel (f) presents the conductivity measurements of bacterial nanocellulose doped with varying weight percentages (wt%) of graphene oxide.Panel (g) represent a schematic overview of transistor using the non-treated nanocellulose as a dielectric layer and GO-treated nanocellulose as a semiconductor for the multiple electronic applications.

Conclusion

Previous research highlighted nanocellulose's suitability for advanced applications, especially in semiconductor technologies. Our previous study demonstrated the semiconducting properties of iodine-doped nanocellulose . Additionally, transistors have been successfully printed on nanocellulose substrates using ink-jet technology, emphasizing the material's adaptability and compatibility with existing manufacturing processes . The potential for single electron transistor properties in nanocellulose indicates its capability to support cutting-edge electronic components . These studies collectively underscore nanocellulose's versatility and promise in advancing environmentally friendly and efficient electronic devices.

Acknowledgement

We thank Land Bavaria for support (contribution to DFG Project number 324392634 – TRR 221/INF)

References

[1] H. Yang, H. Zheng, Y. Duan, T. Xu, H. Xie, H. Du, C. Si, "Nanocellulose-graphene composites: Preparation and applications in flexible electronics," *Int. J. Biol. Macromol.* 253, 126903, 2023, doi: 10.1016/j.ijbiomac.2023.126903.

[2] Y. H. Jung, T. H. Chang, H. Zhang, C. Yao, Q. Zheng, V. W. Yang, H. Mi, M. Kim, S. J. Cho, D .W. Park, "High- 384 performance green flexible electronics based on biodegradable cellulose nanofibril paper," *Nature Communications*, vol. 6, pp. 7170, 2015.

[3] Z. Fang, H. Zhang, S. Qiu, Y. Kuang, J. Zhou, Y. Lan, C. Sun, G. Li, S. Gong, Z. Ma, "Versatile Wood Cellulose for Biodegradable Electronics," *Adv. Mater. Technol.* vol. 6, pp. 2000928, 2021, https://doi.org/https://doi.org/10.1002/admt.202000928.

[4] G. Konwar, P. Saxena, V. Raghuwanshi, S. Rahi, S. P. Tiwari, "Multifunctional Flexible Organic Transistors with a High-k/Natural Protein Bilayer Gate Dielectric for Circuit and Sensing Applications," *ACS App. Electron. Mater.* vol.4, pp. 2525–2533, 2022, https://doi.org/10.1021/acsaelm.2c00303

[5] Y. Xie, C. Ding, Q. Jin, L. Zheng, Y. Xu, H. Xiao, M. Cheng, Y. Zhang, G. Yang, M. Li, "Organic transistor-based integrated circuits for future smart life." *SmartMat*, pp. e1261, https://onlinelibrary.wiley.com/doi/pdf/10.1002/smm2.1261.

[6] M. M. Ansari, Y. Heo, K. Do, M. Ghosh, Y. O. Son, "Nanocellulose derived from agricultural biowaste by-products–Sustainable synthesis, biocompatibility, biomedical applications, and future perspectives: A review." *Carbohydr. Polym. Technol. App.*, vol. 8, pp. 100529, 2022, https://doi.org/10.1016/j.carpta.2024.100529

[7] M. S. Vasheghani Farahani, M. Nikzad, M. Ghorbani, "Fabrication of Fe-doped ZnO/nanocellulose nanocomposite as an efficient photocatalyst for degradation of methylene blue under visible light," *Cellulose*, vol. 29(13), pp. 7277-7299, 2022, https://link.springer.com/article/10.1007/s10570-022-04735-y

[8] J. Yu, Z. Zhu, H. Zhang, Y. Qiu, D. Yin, Y. Cheng, S. Wang, "Stepwise carbonization of nanocellulose to N-doped carbons with structural transformation and enhanced peroxymonosulfate activation." *Chem. Eng. J.*, vol. 407, pp. 127185, 2021, https://doi.org/10.1016/j.cej.2020.127185

Magnetic Nanoparticles Coated with Silica for Biomedical Applications

E. Beňová[a]*, N. Király[a], Ľ. Nagy[b], J. Košuth[c], A. Zeleňáková[b], V. Zeleňák[a]

[a] Institute of Chemistry, Faculty of Science, P.J. Šafárik University, Moyzesova 11, 04001 Košice, Slovakia
[b] Institute of Physics, Faculty of Science, P.J. Šafárik University, Park Angelinum 9, 04001 Košice, Slovakia
[c] Institute of Biology and Ecology, Faculty of Science, P.J. Šafárik University, Šrobárova 2, 04154 Košice, Slovakia
*eva.benova@upjs.sk

Magnetic mesoporous silica nanoparticles (MSNs) are an advanced class of nanomaterials that combine the benefits of magnetic properties with the versatile capabilities of mesoporous silica. These nanoparticles feature a unique structure: a porous silica shell integrated with superparamagnetic iron oxide cores. This design provides a dual functionality: the mesoporous silica shell allows for the efficient loading and controlled release of various therapeutic agents, while the magnetic core facilitates targeted drug delivery and imaging through external magnetic fields [1], [2], [3].

In biomedical applications, magnetic MSNs have emerged as powerful tools due to their ability to enhance drug delivery and imaging [4]. The magnetic properties enable precise targeting of therapeutic agents to specific sites within the body, improving the efficacy and reducing side effects of treatments. Their porous structure supports the encapsulation of a wide range of drugs, including those that are poorly soluble or require controlled release. These nanoparticles are particularly promising in areas such as cancer therapy, where they can be used for targeted drug delivery and magnetic resonance imaging (MRI) to monitor treatment progress. Overall, magnetic MSNs represent a versatile and innovative approach in nanomedicine, combining advanced drug delivery capabilities with enhanced imaging and therapeutic precision [5], [6], [7]. They also hold potential for treating thrombotic disorders, allowing for precise delivery of antithrombotic drugs directly to blood clots, potentially improving treatment outcomes and reducing the risk of systemic side effects [8], [9], [10].

In our project we focused on the synthesis of core-shell magnetic nanoparticles. The core is iron oxide Fe_3O_4, and the shell is made of a non-porous layer of silica with third layer created by various organic ligands or a porous layer of silica. Ferrite nanoparticles were synthesized by coprecipitation method according to BOMB protocol [11]. Briefly, $FeCl_3$ and $FeCl_2$ solutions were mixed in a 1:2 molar ratio and slowly dripped into a preheated alkali solution leading to the formation of black ferrite (Fe_3O_4) precipitate. The core particles were coated with silica immediately after synthesis to prevent their oxidation. Tetraethyl orthosilicate (TEOS) was hydrolysed in a basic environment, thus forming a SiO_2 layer surrounding the magnetic core. The prepared core-shell nanoparticles Fe_3O_4@SiO_2 were further functionalized by different organic ligands, or another layer of porous silica to expand their functionality (Figure 1).

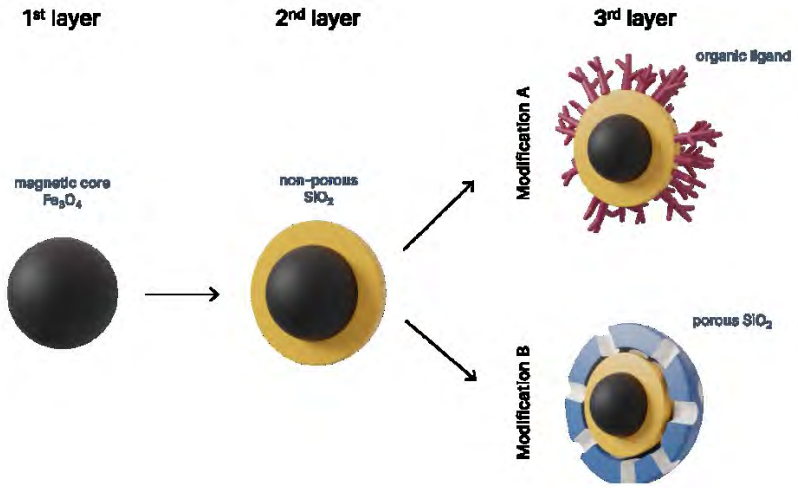

Fig. 1 Schematic representation of individual layers of prepared magnetic materials.

Prepared magnetic nanoparticles were investigated for biomedical purpose: the isolation of viral RNA in diagnostic RT-qPCR. Different magnetic nanoparticles were characterized by HRTEM, SEM, FT-IR, XRD, magnetic measurements, and the efficiency of RNA isolation was quantified by RT-qPCR method. The application of the prepared nanoparticles for isolation of viral RNA was tested on two different kinds of clinical samples and viruses in diagnostic RT-qPCR. One sample represented the complex biological sample - tissue from liver pig naturally infected with hepatitis E virus – HEV, while the others were biofluid samples – swab samples from patients infected by SARS-CoV-2.

We proved efficient reversible adsorption of RNA to the prepared nanoparticles during isolation of viral RNA using commercially available nanobeads-based RNA isolation kits, in which the original/commercial magnetic beads (comMNPs) were replaced by our experimental nanoparticles (eMNPs). We showed that the eMNPs-isolated viral RNA is readily detectable by RT-qPCR with a comparable sensitivity to detection of viral RNA isolated by comMNPs.

Similarly high efficiency of viral RNA isolation by the tested eMNPs was acquired also with biofluid/swab samples infected with SARS-CoV-2 virus. With all tested eMNPs we were able to isolate high quality viral RNA. The comparison with commercial MNPs shows comparable yield of isolated viral RNA. It turned out that two samples unmodified MNPs and porous surface modified MNPs exhibit the results of efficiency like comMNPs.

We expected that the surface modification and surface bound ligands could provide higher capacity for binding RNA and therefore higher effectivity of RNA isolation. Although we used comparable amounts of eMNPs as in the original procedure we did not observe significant improvement in the isolation process. The reason could be saturation of the isolation process, weaker interaction of the modified surface with RNA in the lysis/binding solution or contrariwise too strong affinity of the ligand groups with RNA and problems with elution/desorption efficiency. However, we should point out that using the IVD certified SARS-CoV-2 kit, we always detected all tested SARS-CoV-2 genes in the Covid-19 positive clinical samples, which unambiguously confirmed that RNA isolated using our eMNPs is suitable for clinical diagnostics. Thus, the prepared eMNPs appear to be very suitable for the isolation of viral RNA, or cellular RNA from biofluid samples as well as from animal tissues [12].

We are currently working on the project where we would like to investigate the potential of these magnetic nanoparticles as carriers for antithrombotic drugs. We are currently studying adsorption of antithrombotic drugs (apixaban and rivoraxaban) into magnetic nanoparticles. In the next step we will perform release experiments of loaded drugs. Administration of antithrombotic drugs through silica nanoparticles could lead to a prolongation of their

biological half-life, uniform administration. Such a drug delivery system should enable the targeted administration of the antithrombotic drugs to the thrombotic site directly and their release at the point of need.

Acknowledgements

Funding was provided by Fellowship for excellent researchers R2-R4 (Grant 09I03-03-V04-00722) financed by EU/NextGeneration EU/ program ´´Recovery and Resilience Plan, part of Investment 3: Excellent Science´´.

References

[1]S. R. Mokhosi, W. Mdlalose, A. Nhlapo, and M. Singh, 'Advances in the Synthesis and Application of Magnetic Ferrite Nanoparticles for Cancer Therapy', *Pharmaceutics*, vol. 14, no. 5, Art. no. 5, May 2022, doi: 10.3390/pharmaceutics14050937.

[2]C. Tang *et al.*, 'Application of magnetic nanoparticles in nucleic acid detection', *J. Nanobiotechnology*, vol. 18, no. 1, p. 62, Apr. 2020, doi: 10.1186/s12951-020-00613-6.

[3]C. Comanescu, 'Magnetic Nanoparticles: Current Advances in Nanomedicine, Drug Delivery and MRI', *Chemistry*, vol. 4, no. 3, Art. no. 3, Sep. 2022, doi: 10.3390/chemistry4030063.

[4]A. Avasthi, C. Caro, E. Pozo-Torres, M. P. Leal, and M. L. García-Martín, 'Magnetic Nanoparticles as MRI Contrast Agents', in *Surface-modified Nanobiomaterials for Electrochemical and Biomedicine Applications*, A. R. Puente-Santiago and D. Rodríguez-Padrón, Eds., in Topics in Current Chemistry Collections. , Cham: Springer International Publishing, 2020, pp. 49–91. doi: 10.1007/978-3-030-55502-3_3.

[5]F. da S. Bruckmann, F. B. Nunes, T. da R. Salles, C. Franco, F. C. Cadoná, and C. R. Bohn Rhoden, 'Biological Applications of Silica-Based Nanoparticles', *Magnetochemistry*, vol. 8, no. 10, Art. no. 10, Oct. 2022, doi: 10.3390/magnetochemistry8100131.

[6]S. Khizar, A. A. Al-Dossary, N. Zine, N. Jaffrezic-Renault, A. Errachid, and A. Elaissari, 'Contribution of magnetic particles in molecular diagnosis of human viruses', *Talanta*, vol. 241, p. 123243, May 2022, doi: 10.1016/j.talanta.2022.123243.

[7]P. Montazersaheb, E. Pishgahzadeh, V. B. Jahani, R. Farahzadi, and S. Montazersaheb, 'Magnetic nanoparticle-based hyperthermia: A prospect in cancer stem cell tracking and therapy', *Life Sci.*, vol. 323, p. 121714, Jun. 2023, doi: 10.1016/j.lfs.2023.121714.

[8]V. Priya, Vikas, A. K. Mehata, D. Jain, S. K. Singh, and M. S. Muthu, 'Efficient delivery of abciximab using mesoporous silica nanoparticles: In-vitro assessment for targeted and improved antithrombotic activity', *Colloids Surf. B Biointerfaces*, vol. 218, p. 112697, Oct. 2022, doi: 10.1016/j.colsurfb.2022.112697.

[9]M. Wang, J. Zhang, Z. Yuan, W. Yang, Q. Wu, and H. Gu, 'Targeted Thrombolysis by Using of Magnetic Mesoporous Silica Nanoparticles', *J. Biomed. Nanotechnol.*, vol. 8, no. 4, pp. 624–632, Aug. 2012, doi: 10.1166/jbn.2012.1416.

[10]R. Bhat *et al.*, 'Thrombin-Responsive Gated Silica Mesoporous Nanoparticles As Coagulation Regulators', *Langmuir*, vol. 32, no. 5, pp. 1195–1200, Feb. 2016, doi: 10.1021/acs.langmuir.5b04038.

[11]P. Oberacker *et al.*, 'Bio-On-Magnetic-Beads (BOMB): Open platform for high-throughput nucleic acid extraction and manipulation', *PLOS Biol.*, vol. 17, no. 1, p. e3000107, Spring 2019, doi: 10.1371/journal.pbio.3000107.

[12]A. Zeleňáková *et al.*, 'The surface modification of the silica-coated magnetic nanoparticles and their application in molecular diagnostics of virus infection', *Sci. Rep.*, vol. 14, no. 1, p. 14427, Jun. 2024, doi: 10.1038/s41598-024-64839-2.

Novel Phosphide Catalysts for Hydrogen Evolution Reaction in Both Acidic and Alkaline Environments

C. Bera[a], M. Streckova[a]*, A. Guboova[a],

[a] Institute of Materials Research, Slovak Academy of Sciences, Watsonova 47, 040 01, Kosice, Slovak Republic
*cbera@saske.sk

Today, it is more than clear that green hydrogen will play a key role mainly in the decarbonization of industrial processes and carbon-intensive sectors (ammonia production for fertilizers, heavy industry and transport, aviation, etc.). Now that the price of renewable energy sources like wind and solar has plummeted, green hydrogen has come within economic reach for a huge number of potential applications [1]. However, the production of green hydrogen is still not competitive, as approximately 60% of the total cost is the cost of renewable energy used to produce it. Another important component of the relatively high price of hydrogen is the cost of the electrolyzer and the fuel cell technology. Main goal of this work is to present innovative catalyst used in water electrolysis for two half reactions: hydrogen evolution reaction (HER) and oxygen evolution reaction (OER)[2][3]. The electrode material was prepared by NLE (needleless electrospinning technology). This method is used to generate large scale production of fibers from polymeric solution. Finding optimal composition of reagents and chemicals needs to be achieved to prepare polymer solution. Optimization of heat treatment was also important step in the preparation process. The heat treatment process was suggested based on the results obtained from TG/DSC analysis. Prepared fibers were then heat treated in air to create oxidized form after reduction in combined Ar/H_2 atmosphere. Range of temperatures were proposed – from 700 to 1100 °C in air atmosphere. Prepared materials were fibers without carbon matrix but consisting themselves of NiCoP – noted as F7-11 NiCoP. Morphology and electrochemical performance of these materials was studied. Electrochemical performance of material was investigated and compared with commercial Pt/C for HER and IrO_2 for OER. Electrochemical results revealed that the NiCoP fibers prepared by this methodology operate for HER in alkaline solution at overpotentials η-10 (-141 mV) and η-20 (-230 mV) and low value of Tafel slope (66 mV/dec), while in acidic media the corresponding values were η-10 (-146 mV) and η-20 (-265 mV) with Tafel slope of 77 mV/dec. The NiCoP sample sintered at 900 °C in air endured to work for 22 h without any microscopic degradation. The innovative spinning process employed in the preparation of sample F9 results in a highly conductive fibrous structure with elongated NiCoP particles. This unique morphology maximizes electroactive surface area, leading to exceptional catalytic activity and stability. The absence of an inert carrier further enhances the material's performance and versatility. This proposed methodology offers highly versatile and well-established industry technology for the high-capacity catalyst production.

Acknowledgements

This work was financially funded by the EU NextGenerationEU through the Recovery and Resilience Plan for Slovakia under the project No. 09I03-03-V04-00109 and by the grant of the Slovak Research and Development Agency provided under the contract No. APVV-20-0299 and by the grant of the Slovak Academy of Sciences and The Ministry of Education, Science, Research, and Sport of the Slovak Republic provided under the contracts No. VEGA 2/0027/23.

References

[1]M. Nasser, T. F. Megahed, S. Ookawara, and H. Hassan, “A review of water electrolysis–based systems for hydrogen production using hybrid/solar/wind energy systems,” *Environ. Sci. Pollut. Res.*, vol. 29, no. 58, pp. 86994–87018, 2022, doi: 10.1007/s11356-022-23323-y.

[2]M. Ďurovič, J. Hnát, and K. Bouzek, “Electrocatalysts for the hydrogen evolution reaction in alkaline and neutral media. A comparative review,” *J. Power Sources*, vol. 493, no. February, 2021, doi: 10.1016/j.jpowsour.2021.229708.

[3]X. Xie *et al.*, “Oxygen Evolution Reaction in Alkaline Environment: Material Challenges and Solutions,” *Adv. Funct. Mater.*, vol. 32, no. 21, 2022, doi: 10.1002/adfm.202110036.

Utilizing Gold Nanocrystals to Study Bacterial Growth Inhibition

I. Božeková[a], M. Mazúrová[b], J. Zaťková[b], M. Horniačková[b], M. Sýkora[a]*

[a] Laboratory for Advanced Materials, Faculty of Natural Sciences, Comenius University, Ilkovičova 6, 842 15 Bratislava, Slovakia
[b] Department of Microbiology, Institute of Microbiology, Slovak Medical University in Bratislava, Limbová 12, 833 03 Bratislava, Slovakia
*sykoram@uniba.sk

Introduction

Recent studies showed that gold nanocrystals (Au NCs) with a size below 100 nm have the ability to inhibit the growth of antibiotic resistant bacteria [1-3], which may open a path to effective treatments of bacterial infections. However, for the quantitative studies of the interactions between Au NCs and bacteria, effective methodologies have to be developed. A necessary first step is identification of conditions, where the Au NCs are stable, with respect to aggregation in bacterial growth media, at a sufficiently high concentration for determination of the bacterial minimal inhibitory concentration (MIC). Preliminary results indicate that these concentrations are higher than 300 mg of NCs per milliliter of a growth medium. However, at these concentrations Au NCs aggregate in the known growth media at significantly lower concentrations, which represents a serious barrier for the quantitative studies of the NC-bacteria interactions.

Herein, we describe a method for stabilization of the Au NCs with sizes 4-22 nm in the Tryptic Soy Broth (TSB) bacterial growth medium via modification of the "native" citrate and tannic acid NC surface ligands with HEPES (4-(2-hydroxyethyl)-1-piperazineethanesulfonic acid). We show that the modified NCs are stable in TSB at concentrations up to 500 mg/milliliter, which opens a door to systematic studies of the NC-bacterial interactions at high NC concentrations.

Experimental section

Au NCs were synthetised by colloidal synthesis in aqueous solution via chemical reduction of corresponding salt $HAuCl_4$ (precursors) using reducing agents, tannic acid (TA), sodium citrate (SC) [4]. The materials were obtained from: SC 99.5% Glentham; TA 99.5% and HCl 35% Centralchem; K_2CO_3 99% and $AuCl_3$ 99% Sigma Aldrich; AgNO3 99% VWR, and used without further purification. Transmission Electron Microscopy (TEM) images were obtained using Analytical transmission electron microscope JEM ARM 200cF. The absorption spectra of NCs were collected on diode-array spectrometer Agilent 8453. The biological growth media and buffers were obtained from several suppliers: Tryptic Soy Broth (TSB) from Neogen, USA; Mueller Hinton Broth (MHB) Bio-Rad, France; Luria-Bertani Broth (LB) from BD, Difco Laboratories, France; PBS (Phosphate-Buffered Saline) and HEPES-Buffered Saline from Gibco, USA and refrigerated until use.

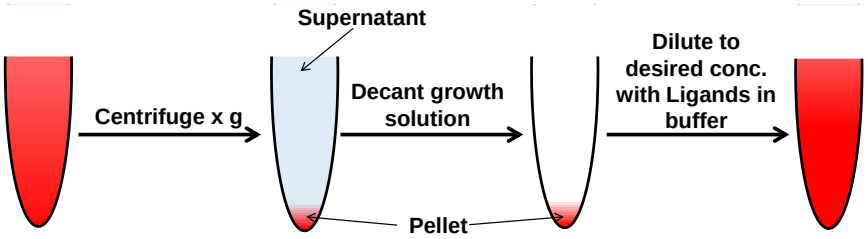

Fig. 1. Schematic representation of centrifugation, where the pellet represents the NC sediment at the bottom of the centrifugal tube and the supernatant is the aqueous solution of the excess ligands.

The surface modification procedure is schematically summarized in Fig. 1. In a first step the growth solution from the Au NC synthesis centrifuged at high speeds (depending on NC size). After centrifugation, the NCs form a pellet on the bottom of the centrifuge tube, which can be separated from the excess of "native" ligands by decanting the supernatant. Subsequently the NC pellet is dissolved in a concentrated solution of a buffer containing the ligand selected for the surface ligand exchange. This procedure also allows adjustment of the concentration of Au NCs. The changes in optical properties of NCs upon transfer to the biological growth media were analyzed by comparison of the turbidity (absorption spectra) of the NCs in water solution (control) and appropriate growth medium.

Results and discussion

Following the procedures reported previously in literature [4], we prepared Au NCs with sizes in the range of 4 - 22 nm. The optical spectra of selected Au NCs in water are shown in Fig. 2a. The spectra are characterized by a distinct plasmonic peaks at 505-522 nm, related to size of Au NCs. The sizes of the prepared NCs were determined by TEM (see Fig. 2 b-c). The size dispersion of the prepared materials ranged from 10-20 % (Fig. 2 d-e). In aqueous solution the absorption spectra of NCs were stable for period of at least 1 year.

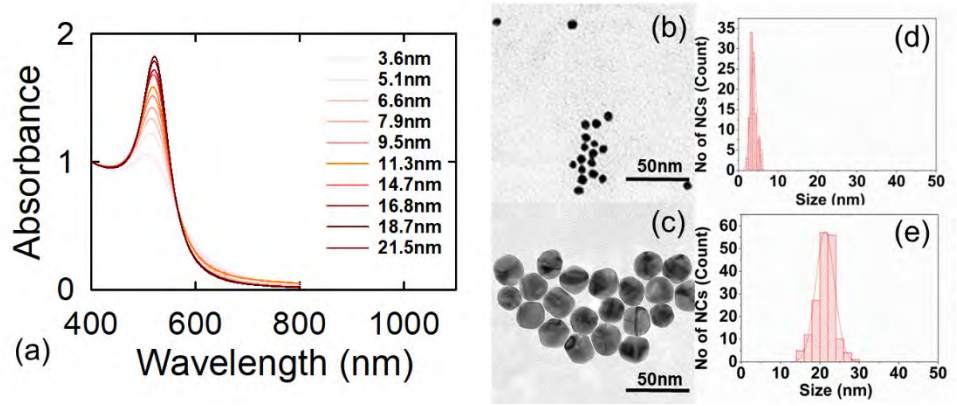

Fig. 2 (a) The absorption spectra of Au NCs in aqueous media (b-c) examples of TEM images and (d-f) size dispersion histograms for the synthesized Au NCs.

The functionalization of Au NCs was monitored by UV-VIS absorption spectroscopy. Example of Au NCs optical spectra in water before and after ligand exchange are shown in Fig. 3. After binding of selected ligands to the Au NCs surface, the Abs_{max} peak will red-shift by a few nanometers, which is attributed to the change in the dielectric constant at the Au NCs surface. If the approximate 3 nm red-shift of the peak is accompanied by maintaining the overall shape of the spectra, that suggests a successful conjugation of the new ligands to the gold surface.

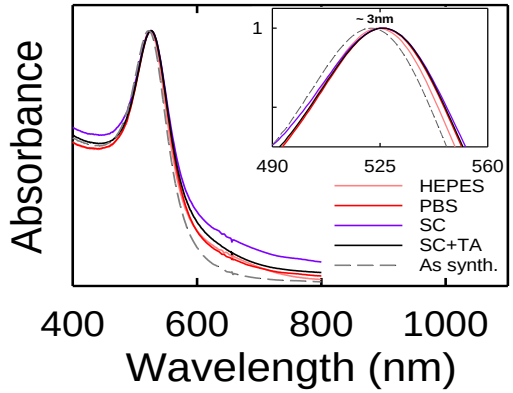

Fig. 3 The absorption spectra of Au NCs with diameter 22.3 nm, before and after ligand exchange.

While in the aqueous media the absorption spectra were stable, upon transferring to biological growth media, the absorption spectra of Au NCs show distinct changes (Fig. 4 a-d.). These optical changes are associated with the aggregation of the NCs. When the NCs aggregate, the absorption peaks dramatically red-shift and become broader. This behaviour was observed in the case of MHB, LB and in the case of Au NCs passivated with native citrate ligand also in TSB. Aggregation states are also visibly detected by a change in colour of the solution from red to blue/purple or transparent. Similar studies were also performed for other sizes of Au NCs. The results suggest that the stability of the Au NCs is best in TSB growth medium with HEPES ligands on their surface.

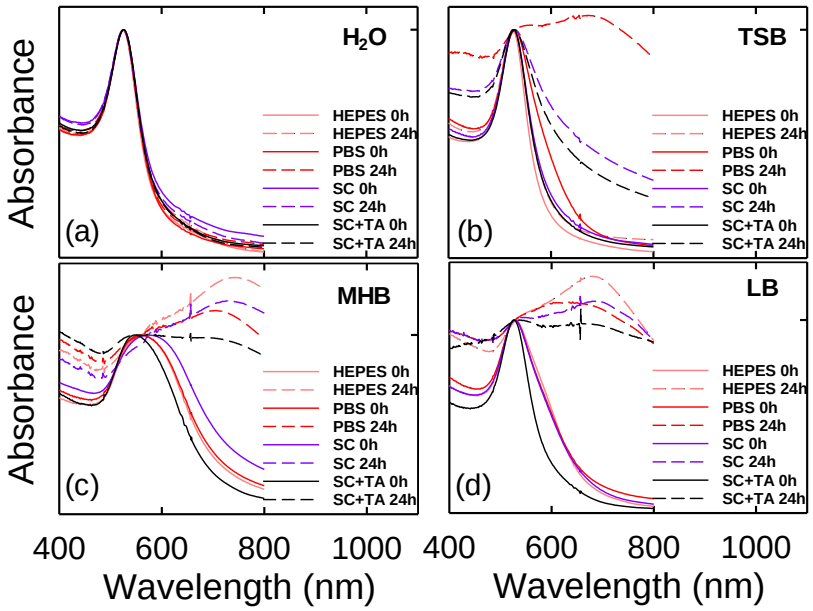

Fig. 4 A comparison of the absorption spectra of Au NCs with diameter 22.3nm (a) in water; (b) in TSB; (c) in MHB; (d) in LB, with different ligands on their surface.

Conclusions

We prepared and characterized Au NCs with sizes of 4-22 nm. They are stable in aqueous media and show characteristic plasmonic absorption peaks, with the peak energy varying systematically with the NC size. However, the absorption characteristics of the plasmon bands are significantly distorted in the biological growth media, primarily due to the NC aggregation. We found that when the native ligands are substituted with HEPES ligand the NCs can be stabilized in TSB with respect to aggregation. This opens a path to studies of interactions between Au NCs and bacteria. More quantitative analysis of the inhibition concentration and the mechanism of NCs bacteria interactions are currently in progress.

Acknowledgements

This work was financially supported by the European Union's Horizon 2020 research and innovation programme under grant agreement No. 810701, Slovak Research and Development Agency under grant agreement No. APVV-23-0300, Slovak Ministry of education under grant agreement No. 1/0892/21, Slovak Medical University in Bratislava Grant No 132021-SVG1 and by UK grant No. UK/425/2021 and UK/1177/2024.

References

[1] T. Vos, S.S. Lim, C. Abbafati, et.al.“ Global burden of 369 diseases and injuries in 204 countries and territories, 1990–2019: a systematic analysis for the Global Burden of Disease Study 2019,” *The Lancet*, vol. 396, no. 10258, pp. 1204-1222, October. 2020, doi: 10.1016/S0140-6736(20)30925-9.

[2] M. A. Faramarzi, A. Sadighi.“ Insights into biogenic and chemical production of inorganic nanomaterials and nanostructures,” *Adv. Colloid Interface Sci.*, vol. 189-190, pp. 1-20, March. 2013, doi: 10.1016/j.cis.2012.12.001.

[3] D. Pires, M. E. A. Kraker, E. Tartari, et al.“ Fight Antibiotic Resistance—It’s in Your Hands’: Call From the World Health Organization for 5th May 2017,” *Clin. Inf. Diseases.*, vol. 64, no. 12, pp. 1780-1783, May. 2017, doi: 10.1093/cid/cix226

[4] J. Piella, N. G. Bastús, V. Puntes, et al.“ Size-Controlled Synthesis of Sub-10-nanometer Citrate-Stabilized Gold Nanoparticles and Related Optical Properties,” *Chem. Mater.*, vol. 28, no. 4, pp. 1066-1075, January. 2016, doi: 10.1021/acs.chemmater.5b04406.

Modification of Simple Model of Cell Surface with Anti-adhesion Chemicals

D. Burčík[a]*, N. Podrojková[a], A. Oriňak[a]

[a] Department of Physical Chemistry, Moyzesova 11, Košice 04001, Slovakia
*5170274@upjs.sk

Cancer presents one of the most dangerous and lethal diseases in the world. Several scientific disciplines try to provide the best techniques and approaches to understand and cure this disease. Every discipline examines cancer from a different angle of view. Progress of cancer can be characterized by many biological or chemical parameters. Many stages of cancer are connected with cell adhesion. Cell adhesion provides mostly communication between cells and is responsible for cohesion of tissues. Cancer cells undergo mutations that determine their characteristics and abilities. Many cancer cells gain metastatic potential and can become circulating tumor cell (CTC). Cancer cells have aggressive behavior and uncontrollably reproduce themselves. Cell adhesion is very important for cancer cells, too (fig.1). These cells can break adhesion forces between healthy cells in the process of their invasion into distant tissues or organs. Cell adhesion is directly connected with few physical parameters. Most important of them is surface energy. Surface energy can be modified by several chemicals. Changes of surface energy lead to interruption of cell adhesion. This method could block cell adhesion in different stages of cancer development. However, it is important to find out how various chemicals can influence surface energy of cancer cells. Also, not all types of cancers are compatible with all chemicals. Every cancer cell has on its surface several same or different receptors which interact with ligands that we can find in an extracellular matrix or on the surface of other cells. Receptors are the most common cell adhesion molecules (integrins, selectins, immunoglobulins or cadherins). Cell adhesion can be blocked by creation of ligand-receptor interaction or modification of biochemical cascades in cells. This is a good opportunity to stop spreading cancer or metastases in organisms.

There are several techniques and methods on how to measure surface energy. In most cases scientists measure contact angle which can help to observe changes on cell surfaces. Chosen methods depend on provided experiments. One of possible options is interference contrast microscopy. This method uses surfaces created from a double layer, which consist of thin glass surface and agarose bead that is modified to interact with specific ligands. These experiments use Johnson-Kendall-Robertson's model which effectively connects size of surfaces and their elasticity with surface energy [1]. This measurement depends on binding affinity of potential ligands and receptors in this model situation. Low binding affinity is characterized by linear trend and high binding affinity is characterized by logarithmic trend. Agarose beads could simulate a simple model of cytoplasmic membrane. It can be modified by one of the cell surface receptors. Then there are added different chemicals which can bind with these specific receptors. During experiment there is observed binding affinity of chosen chemicals and also changes in model's surface energy in this process. For purposes of our experiment we chose two chemicals with anti-adhesion characteristics, ursolic acid [2] and folic acid [3]. These acids were originally extracted from natural resources (various parts of plants). Their lower concentrations are not toxic for healthy cells and still report the ability to influence cell adhesion. They can bind to different receptors on cell surfaces according to binding affinity of presented receptors. Mostly, they bind with cell adhesion molecules which are responsible for cell adhesion.

Modification of cell surfaces has promising potential to better understand cancer or many other diseases connected with cell adhesion. Anti-adhesion chemicals can be used as functional ligands in treatment of cancer or as supportive medications during this procedure. All executed experiments were conducted with model situations. For in vivo studies there is necessary to create nanocarriers with knowledge of nanotechnology.

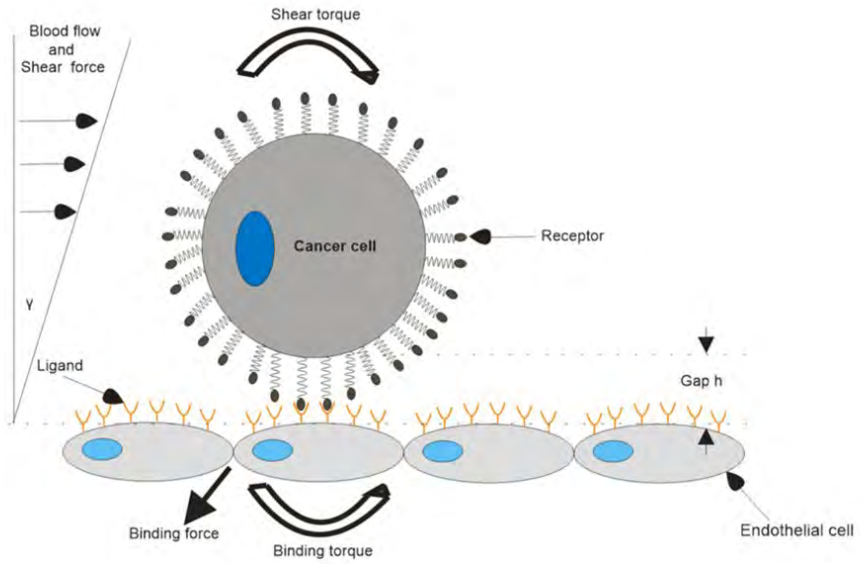

Fig. 1 Schematic picture of the adhesion of CTC to endothelial cells. CTC has a receptor on its surface and endothelial cells express ligands [4].

Acknowledgements

Thanks for financial support of APVV-20-0278.

References

[1] V. T. Moy, Y. Jiao, T. Hillmann, H. Lehmann, and T. Sano, "Adhesion energy of receptor-mediated interaction measured by elastic deformation," *Biophys J*, vol. 76, no. 3, pp. 1632–1638, 1999, doi: 10.1016/S0006-3495(99)77322-4.

[2] D. Kashyap, H. S. Tuli, and A. K. Sharma, "Ursolic acid (UA): A metabolite with promising therapeutic potential," *Life Sciences*, vol. 146. Elsevier Inc., pp. 201–213, Feb. 01, 2016. doi: 10.1016/j.lfs.2016.01.017.

[3] S. C. Liew, "Folic acid and diseases - Supplement it or not?," *Revista da Associacao Medica Brasileira*, vol. 62, no. 1. Associacao Medica Brasileira, pp. 90–100, Jan. 01, 2016. doi: 10.1590/1806-9282.62.01.90.

[4] J. Cui, Y. Liu, L. Xiao, S. Chen, and B. M. Fu, "Numerical study on the adhesion of a circulating tumor cell in a curved microvessel," *Biomech Model Mechanobiol*, vol. 20, no. 1, pp. 243–254, Feb. 2021, doi: 10.1007/s10237-020-01380-x.

8th International Conference on Novel Materials Fundamentals and Applications
High Tatras, 13.-16.10.2024

Chalcogenide Perovskites and Their Thermal Stability

R. Bystrický[a,b]*, S. K. Tiwari[a], P. Hutár[a,c], M. Sýkora[a]*

[a] Laboratory for Advanced Materials, Faculty of Natural Sciences, Comenius University, Ilkovičova 6, 842 15 Bratislava, Slovakia
[b] Center for Advanced Materials Applications, Slovak Academy of Sciences, Dúbravská cesta 9, 845 11 Bratislava, Slovakia
[c] Institute of Electrical Engineering, Slovak Academy of Sciences, Dúbravská cesta 9, 841 04 Bratislava, Slovakia
*roman.bystricky@uniba.sk, *sykoram@uniba.sk

Introduction

Halide Perovskites (HPs) have over the past two decades attracted a great deal of attention due to their record-breaking performance as active components of solar cells [1-3] and other optoelectronic applications [4, 5]. Integration of HPs into thin-film solar cells led to unprecedented performance enhancements [6]. HPs were also shown to be very promising materials for the development of efficient light-emitting diodes, lasers, detectors, and other technologies [7-9]. Despite the promise of HPs, their limited thermal and chemical stability and inclusion of toxic ions, such as lead, pose challenges for their commercial exploitation.

Structurally related Chalcogenide Perovskites (CPs), crystalline solids with composition ABX_3, where A, B, are metal cations and X = S^{2-}, Se^{2-}, have recently been suggested as a possible alternative with the potential to address the limitations of HPs [10, 11]. Theoretical and experimental studies suggest that CPs have optical and electronic properties similar to the HPs and can be prepared without the use of toxic elements [12-14]. Initial studies of thermal stability of $BaZrS_3$ and β-$SrZrS_3$ powders concluded that CPs have an excellent thermal stability in air to at least 550 °C and that the $BaZrS_3$ films show better thermal and chemical stability than HP $MAPbI_3$ ($MA = CH_3NH_3^+$) [15, 16].

Experimental section

In a typical reaction, starting materials (ternary oxide, boron, sulfur) were ground in an agate mortar for 10-15 min. Well ground powder was transferred to a 15 mm i.d. quartz tube. The tube was connected to a Schlenk line and evacuated at <2 Pa for 30 min. After the flame sealing, the ampule with the reagents was transferred into a temperature calibrated furnace where it was heated at temperatures 800-1000 °C. The typical heating rate was 5 °C/min with the holding time 5 hrs. at 300 °C and 600 °C and the cooling rate was 5 °C/min. After the cool down, the ampoules were opened at ambient conditions and characterized. The crystalline phases present in the powder samples were identified using X-ray diffraction (XRD) (Panalytical Empyrean, Netherlands, Cu Kα radiation). High-temperature XRD measurement was performed on Panalytical Empyrean diffractometer coupled with Anton Paar high-temperature chamber HTK-16N using Pt heating strip in air. The patterns were collected every 10 °C, with data collection time of 60 seconds. During the data collection the temperature was held constant. The heating rate between the measurements was 8 °C/min. Reflectance spectra were measured on Jasco V-770 (Uv-Vis/NIR) spectrophotometer attached to a manual absolute reflectance measurement accessory ARSN-917. Thermal analysis (TG-DTA) was performed with Linseis STA1600, (Linseis Messgeraete GmbH, Germany) with heating rate of 8 °C/min up to 800 °C in air.

Results and discussion

The thermal stability was studied on 4 ternary chalcogenide perovskites, namely $BaZrS_3$, β-$SrZrS_3$, $BaHfS_3$ and $SrHfS_3$. Their stability was compared with two representative HPs, $MAPbI_3$ ($MA = CH_3NH_3^+$, methylammonium) and $CsPbI_3$. Thermal analysis was done on all samples. Results are shown in the Figure 1 [17]. The results for HPs show that the initial mass loss for both materials is observed in the temperature range 250–320 °C where they are

decomposing to binary halides. The results for CPs show that they are stable up to 550 °C, where they start to oxidize. The resulting product is composed from binary oxides and sulfates.

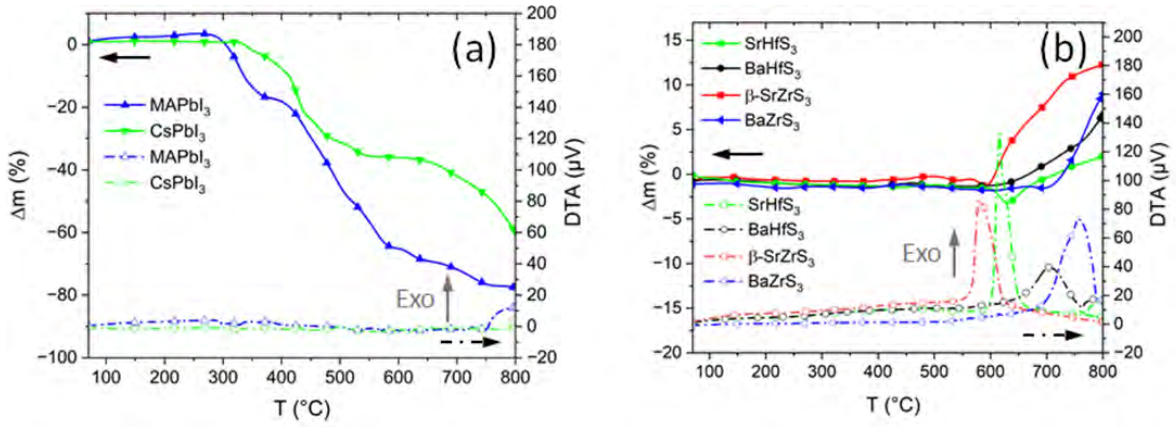

Fig. 1 Mass change and DTA of prepared HPs (a) CPs (b) as a function of temperature. The heating rate was 8 °C/min. Measurements were done in air [17].

The HT XRD of CPs comfirmed the results of thermal analysis. In the Figure 2a results of representative CP $BaZrS_3$ are shown [17]. At around 520 °C, splitting of peaks at around 37, 43 and 51° is clearly visible, which was assigned to the phase transition from the distorted perovskite phase (orthorhombic, *Pnma*) to a pseudo-cubic (tetragonal, $I4_1/acd$) phase. At 570 °C $BaZrS_3$ starts to oxidize accompanied by emerging new set of peaks. The peaks belonging to $BaZrS_3$ are continuously disappearing and they are completely undetectable at ~670 °C.

The effect of heating on the optical properties of CPs was investigated by diffuse reflectance (DR) spectroscopy. The results of representative CP $BaZrS_3$ are summarized in Figure 2b [17]. It shows the comparison of the reflectance (as 1-R%) for the as-prepared $BaZrS_3$, sample heated at 100 °C in air for 1 week (168 hrs.), sample heated 800 °C in air for 30 min. and a control $BaZrO_3$ sample. The DR spectra of the as-prepared sample shows a distinct onset of the signal in the range 500–800 nm. The DR spectra of the $BaZrS_3$ heated at 100 °C for 1 week is very similar to the as-prepared sample. Following the heating of the CPs at 800 °C the sharp band-edge onsets disappear altogether and a 50 – 60% increase in reflectance (decrease in 1-R %) is observed. The DR spectra of the oxidized $BaZrS_3$ is similar with the control $BaZrO_3$. This difference is attributed primarily to the presence of $BaSO_4$, identified in the oxidation products by XRD analysis.

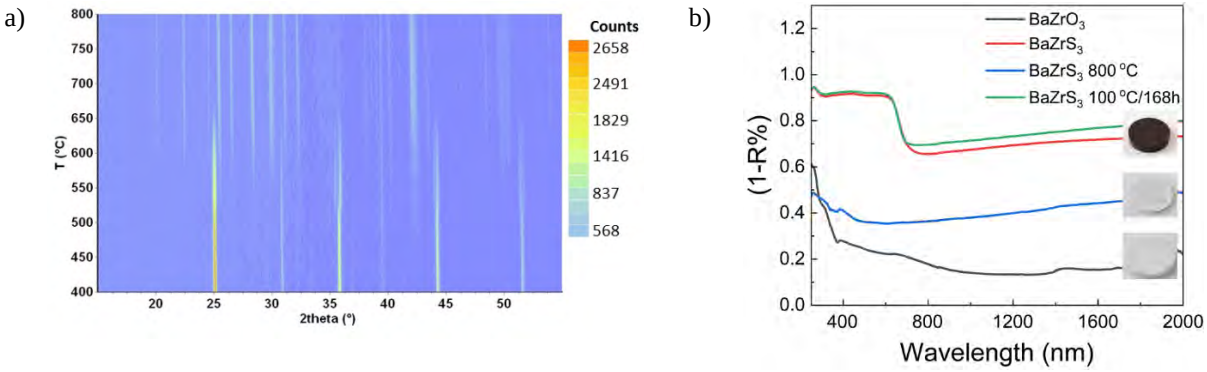

Fig. 2 a) HT XRD patterns of $BaZrS_3$ recorded in the temperature range 400–800 °C. Measurement was performed in air. The heating rate between the data collections was 8 °C/min. During the data collection, 60s, the temperature was held constant, b) diffuse reflectance of $BaZrS_3$ as-prepared (red trace), after heating in air at 100 °C for one week (green trace) and after heating in air at 800 °C for 30 min (blue trace). The DR spectra of the $BaZrO_3$ is shown as black trace for comparison. The insets show the photographs of the CP pellets, overlaid with the corresponding DR spectra [17].

Conclusions

Thermal stability of 4 ternary CPs was studied in the temperature range 25–800 °C and was compared with thermal stability of representative HPs. It was found that the CPs are stable up to 550 °C while the HPs are decomposing at around 300 °C. HT XRD of $BaZrS_3$ showed the phase transition at around 520 °C and oxidation above 550 °C. The results of diffuse reflectance measurements showed that the diffuse reflectance of the $BaZrS_3$ heated at 100 °C for 1 week is very similar to the as-prepared sample. Following the heating of the $BaZrS_3$ at 800 °C the sharp band-edge onsets disappear altogether and a 50 – 60% increase in reflectance (decrease in 1-R %) is observed. The diffuse reflectance spectra of the oxidized $BaZrS_3$ is similar with the control $BaZrO_3$.

Acknowledgements

This work was supported by the European Union's Horizon 2020 research and innovation programme under grant agreement no. 810701 and by the Slovak Research and Development Agency under grant agreement no. APVV-19-0410 and APVV-23-0202.

References

[1] M. A. Green, A. Ho-Baillie, and H. J. Snaith, "The emergence of perovskite solar cells," *Nature Photonics*, vol. 8, no. 7, pp. 506-514, 2014, doi: 10.1038/nphoton.2014.134.

[2] C. Bi, Q. Wang, Y. Shao, Y. Yuan, Z. Hiao, and J. Huang, " Non-wetting surface-driven high-aspect-ratio crystalline grain growth for efficient hybrid perovskite solar cells," *Nature Comm.* vol. 6, pp. 7747, 2015, doi: 10.1038/ncomms8747.

[3] T. Zhang, M. Yang, Y. Zhao, K. Zhu, "Controllable Sequential Deposition of Planar $CH_3NH_3PbI_3$ Perovskite Films via Adjustable Volume Expansion," *Nano Lett.*, vol. 15, no. 6, pp. 3959-3963, 2015, doi: 10.1021/acs.nanolett.5b00843.

[4] Q. Dong, Y. Fang, Y. Shao, P. Mulligan, J. Qiu, L. Cao, and J. Huang, "Electron-hole diffusion lengths 175 μm in solution-grown $CH_3NH_3PbI_3$ single crystals," *Science*, vol. 347, no. 6225, pp. 967-970, 2015, doi: 10.1126/science.aaa5760.

[5] H. Zhu, Y. Fu, F. Meng, X. Wu, Z. Gong, Q. Ding, M. V. Gustafsson, M. T. Trinh, S. Jin, and X. Y. Zhu, "Lead halide perovskite nanowire lasers with low lasing thresholds and high quality factors," *Nature Mater.* vol. 14, no. 6, pp. 636-642, 2015, DOI: 10.1038/nmat4271.

[6] Best Research-Cell Efficiency Chart. https://www.nrel.gov/pv/cell-efficiency.html.

[7] X. K. Liu, W. D. Xu, S. Bai, Y. Z. Jin, J. P. Wang, R. H. Friend, and F. Gao, "Metal halide perovskites for light-emitting diodes," *Nat. Mater.*, vol 20, no. 1, pp. 10−21, 2021.

[8] L. Lei, Q. Dong, K. Gundogdu, and F. So, "Metal Halide Perovskites for Laser Applications," *Adv. Funct. Mater*., vol. 31, 2021, 2010144, doi: 10.1002/adfm.202010144

[9] H. Kim, J. S. Han, J. Choi, S. Y. Kim, and H. W. Jang, "Halide Perovskites for Applications beyond Photovoltaics," Small Methods, vol. 2, 2018, 1700310, doi: 10.1002/smtd.201700310

[10] M. Buffiere, D. S. Dhawale, and F. El-Mellouhi, "Chalcogenide Materials and Derivatives for Photovoltaic Applications," *Energy Technology*, vol. 7, no. 11, 2019, 1900819, doi: 10.1002/ente.201900819.

[11] K. V. Sopiha, C. Comparotto, J. A. Márquez, and J. J. S. Scragg, "Chalcogenide Perovskites: Tantalizing Prospects, Challenging Materials," *Adv. Opt. Mat.*, vol. 10, no. 3, 2021, 2101704, doi: 10.1002/adom.202101704.

[12] Y. Y. Sun, M. L. Agiorgousis, P. Zhang, and S. Zhang, "Chalcogenide perovskites for photovoltaics," *Nano Lett. vol. 12, no. 1*, **2015**, pp. 581-585, doi: 10.1021/nl504046x.

[13] S. Niu, H. Huyan, Y. Liu, M. Yeung, K. Ye, L. Blankemeier, T. Orvis, D. Sarkar, D. J. Singh, R. Kapadia, and J. Ravichandran, "Bandgap Control via Structural and Chemical Tuning of Transition Metal Perovskite Chalcogenides," *Adv. Mater*., vol. 29, no. 9, 2017, 1604733, doi: 10.1002/adma.201604733

[14] Y. Nishigaki, T. Nagai, M. Nishiwaki, T. Aizawa, M. Kozawa, K. Hanzawa, Y. Kato, H. Sai, H. Hiramatsu, H. Hosono, H. Fujiwara, "Extraordinary Strong Band-Edge Absorption in Distorted Chalcogenide Perovskites," *Solar RRL*, vol. 4, no. 5, 2020, 1900555, doi: 10.1002/solr.201900555.

[15] T. Gupta, D. Ghoshal, A. Yoshimura, S. Basu, P. K. Chow, A. S. Lakhnot, J. Pandey, J. M. Warrender, H. Efstathiadis, A. Soni, S. Zhang, T.-M. Lu, and N. Koratkar, "An Environmentally Stable and Lead-Free Chalcogenide Perovskite," *Adv. Funct. Mater.*, vol. 30, no. 23, 2020, 2001387, doi: 10.1002/adfm.202001387.

[16] S. Niu, J. Milam-Guerrero, Y. Zhou, K. Ye, B. Zhao, B. C. Melot, and J. Ravichandran, "Thermal stability study of transition metal perovskite sulfides," *J. Mater. Res.*, vol. 33, no. 24, 2018, pp. 4135-4143, doi: 10.1557/jmr.2018.419.

[17] R. Bystrický, S. K. Tiwari, P. Hutár, M. Sýkora, "Thermal Stability of Chalcogenide Perovskites," Inorg. Chem., vol. 63, no. 28, 2024, pp. 12826-12838, doi: 10.1021/acs.inorgchem.4c01308

Microstructure and Phase Analysis of Zn-Ag Alloys

V. Čákyová[a]*, R. Oriňaková[a], M. Kupková[b], T. Sopčák[b], M. Džupon[b]

[a] Department of Physical Chemistry, Faculty of Science, P. J. Šafárik University in Košice, Moyzesova 11, 041 54, Košice, Slovak republic
[b] Slovak Academy of Sciences, Institute of Materials Research, Košice, Slovakia
*viktoria.cakyova@student.upjs.sk

As society has progressed, bone injuries, deformities, and other challenges caused by population aging, diseases, and accidents have increased the requirement for orthopaedic implant materials [1]. Recently, biodegradable metallic materials have become a focus of orthopaedic material research. We tend to divide biodegradable metallic compounds into following categories: magnesium, iron, zinc and its alloys. Despite substantial research, Mg-based alloys are limited in their uses due to their fast corrosion in physiological settings and the hydrogen produced during degradation. Conversely, iron alloys have a lower corrosion rate than clinical standards, prolonging tissue contact with metals. The rate of zinc degradation is between that of magnesium and iron. Degradation products of zinc are fully bioresorbable without hydrogen gas evolution [2]. Zinc is the second most prevalent trace element in the human biological system, following iron, and is crucial for enzymes to carry out their regulatory and catalytic functions. Also, zinc inhibits osteoclast bone internalization and promotes osteoblast development, making it necessary for osteogenesis and mineralization [3]. Although Zn-based alloys are promising materials for biomedical applications due to their excellent biodegradability and biocompatibility, however, their mechanical properties, such as strength and ductility, can be a limitation for load-bearing applications in the body. The addition of magnesium, copper, silver, calcium, strontium, aluminium, and lithium to zinc increases the alloys' mechanical strength [4].

In this study, three binary alloys with a composition of 98 wt. % Zn and 2 wt. % Ag (Zn-2Ag), 96 wt. % Zn and 4 wt. % Ag (Zn-4Ag), 94 wt. % Zn and 6 wt. % Ag (Zn-6Ag) and pure Zn were produced by a powder metallurgy process. The Zn and Ag powders were manually mixed in the correct ratio to obtain a homogeneous mixture with uniformly dispersed particles. Next, cylindrical samples with a diameter of 13 mm and a weight of 2 g were prepared using a hydraulic press operating at a pressure of 600 MPa. The resulting green compacts were sintered at a temperature of 350°C for 60 minutes in a ceramic furnace under argon atmosphere. Ag was used as an alloying element to enhance the strength and ductility of Zn. A microstructural examination was conducted utilizing optical microscopy, scanning electron microscopy (SEM) coupled with energy dispersive X-ray analysis (EDX), and X-ray diffraction (XRD) to investigate the morphology and phase composition of the materials. To carry out optical microscope examination, the conventional metallographic techniques were used, which included griding, polishing, and etching.

The microstructure of implants determines the performance, corrosion properties, and characteristics of the implants. Therefore, it is crucial to thoroughly investigate it. The microstructure is influenced by processing techniques, alloying elements, design choices, impurities, and thermal treatments. Figure 1 presents a XRD spectrum, which revealed the presence of Zn in all the Zn-Ag samples. Values of diffraction angle of the Zn peaks were 36.34 (002), 39.06 (100), 43.28 (101), 54.36 (102), 70.68 (110), 77.04 (004), 82.16 (112), and 86.58 (201) [5]. Within all samples, we identified the existence of zinc oxide (ZnO) with 2 θ values of 31.84 (100), 34.52 (002), 36.38 (101), 47.64 (102), 56.7 (110), and 68.1 (112) [6]. Ag exhibits distinct peaks at 2 θ 38 (111), 44 (200), 77 (311), and 81 (222) [7]. The absence of Ag peaks in the samples suggests the formation of a bimetallic phase between silver and zinc. The presence of a bimetallic phase AgZn with a 2 θ value of 28.27 (210) was observed in samples Zn-2Ag and Zn-4Ag. The Zn-6Ag sample exhibited a prominent peak at 2 θ of 41. The observed peak could be assigned to the AgZn phase, which exhibits a peak at 2 θ of 40.95 (221), or the $AgZn_3$ phase, which displays a peak at 2 θ of 41.83 (002). $AgZn_3$ was present in all Zn-Ag samples at characteristic peaks with 2 θ values of 35.9 (100) and 42.58 (101) [8].

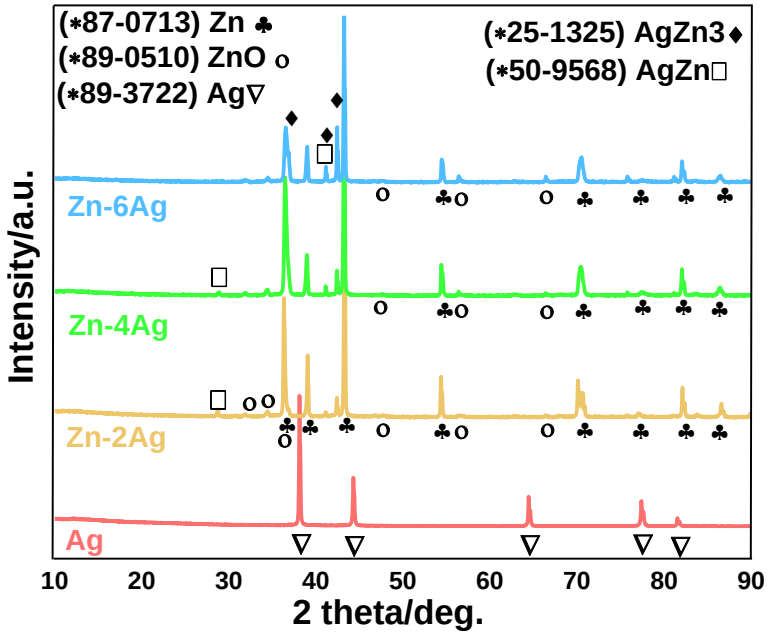

Fig. 2 XRD analysis of Zn-Ag samples.

Small globular Zn grains and a second phase of asymmetric large grains can be seen in the microscopic structure of Zn-Ag samples (Figure 2 A). With increasing Ag content, the second phase shows more asymmetric clusters of grains. Zn atoms create AgZn or $AgZn_3$ phases inside the Ag crystal structure. The Kirkendall effect is a classical phenomenon in materials science, and it is referred to as a nonreciprocal interdiffusion process through an interface of two metals with strikingly different atomic diffusivities, leading to a formation of vacancies called Kirkendall voids [9]. Figure 2 B) illustrates the process of formation of new phases. The Zn-Ag samples were produced by sintering at 350°C, with the melting temperature of Zn being 419.5°C and the melting point of Ag being 961.8°C. This resulted in faster movement of Zn atoms during sintering and their diffusion into the interior of Ag particles to form an intermetallic phase. This phase can consist of AgZn, $AgZn_3$ or their mixture. At the same time, the movement of vacancies into Zn has the potential to induce the formation of cracks in the Zn phase. The presented results show that, the addition of Ag as and alloying element led to the formation of AgZn and $AgZn_3$ phases. The study also found that Zn-Ag samples had both small globular Zn grains and large asymmetrical grains. The grain clustering was stronger when there was more Ag in the sample. The sintering process at 350°C made it easier for Zn atoms to move into Ag.

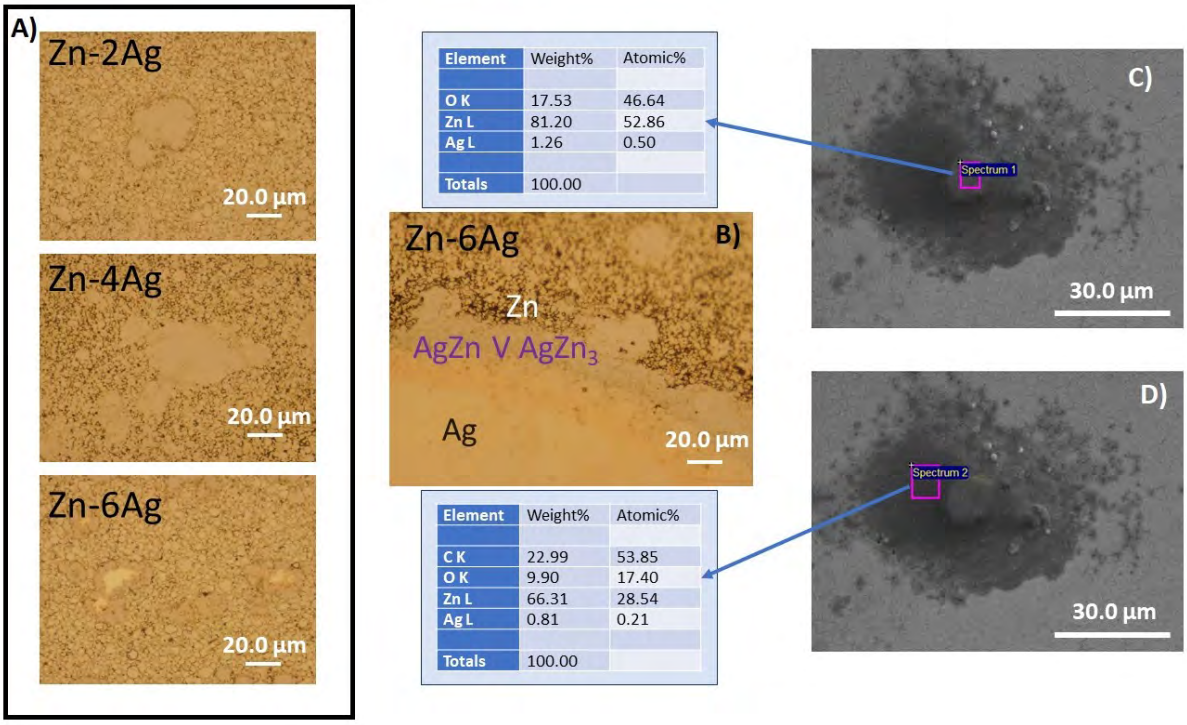

Fig. 3 Microstructure of Zn-Ag samples A); microstructure of Zn-6Ag; SEM picture of the Zn-6Ag with EDX analysis C) and D).

Acknowledgements

This work was supported by the Slovak Research and Development Agency under the project APVV-20-0278 and Visegrad grants from the International Visegrad Fund (project no. 22310096).

References

[1] X. Tong *et al.*, "Microstructure, mechanical properties, biocompatibility, and in vitro corrosion and degradation behavior of a new Zn–5Ge alloy for biodegradable implant materials," *Acta Biomater*, vol. 82, pp. 197–204, Dec. 2018, doi: 10.1016/j.actbio.2018.10.015.

[2] X. Tong *et al.*, "Biodegradable Zn–Dy binary alloys with high strength, ductility, cytocompatibility, and antibacterial ability for bone-implant applications," *Acta Biomater*, vol. 155, pp. 684–702, Jan. 2023, doi: 10.1016/j.actbio.2022.10.053.

[3] A. D. Akinwekomi and F. Akhtar, "Tunability of mechanical and biodegradation properties of zinc-based biomaterial with calcium Micronutrient alloying," *J Mech Behav Biomed Mater*, vol. 140, Apr. 2023, doi: 10.1016/j.jmbbm.2023.105724.

[4] H. Kabir, K. Munir, C. Wen, and Y. Li, "Recent research and progress of biodegradable zinc alloys and composites for biomedical applications: Biomechanical and biocorrosion perspectives," Mar. 01, 2021, *KeAi Communications Co.* doi: 10.1016/j.bioactmat.2020.09.013.

[5] A. C, P. K. Shetty, and M. M G, "Investigation on structural, optical and electrical properties of Zn doped indium oxide thin film for gamma dosimetry," *Mater Chem Phys*, vol. 302, Jul. 2023, doi: 10.1016/j.matchemphys.2023.127712.

[6] A. Yahyaoui, T. Bouarroudj, and K. Houssem, “Mohammed-Réda Djebar,” 2017. [Online]. Available: https://www.researchgate.net/publication/323586692

[7] Y. Meng, “A sustainable approach to fabricating ag nanoparticles/PVA hybrid nanofiber and its catalytic activity,” *Nanomaterials*, vol. 5, no. 2, pp. 1124–1135, Jun. 2015, doi: 10.3390/nano5021124.

[8] T. C. Hsuan and K. L. Lin, “Microstructural evolution of ε-AgZn3 and η-Zn phases in Sn-8.5Zn-0.5Ag-0.01Al-0.1Ga solder during aging treatment,” *J Alloys Compd*, vol. 469, no. 1–2, pp. 350–356, Feb. 2009, doi: 10.1016/j.jallcom.2008.01.121.

[9] W. Wang, M. Dahl, and Y. Yin, “Hollow nanocrystals through the nanoscale Kirkendall effect,” Apr. 23, 2013. doi: 10.1021/cm3030928.

8th International Conference on Novel Materials Fundamentals and Applications
High Tatras, 13.-16.10.2024

Effect of Manufacturing Parameters on Mechanical Properties of Zinc Foams

W. Du[a]*, C. Wiener[a,b]

[a] Department of Materials Science and Engineering, Budapest University of Technology and Economics, Műegyetem rkp. 3., H-1111 Budapest, Hungary
[b] MTA–BME Lendület "Momentum" High-performance Composite Metal Foams Research Group, Műegyetem rakpart 3., H-1111 Budapest, Hungary
*duwanrong@edu.bme.hu

Introduction

Recently, due to the influence of the aging population and the prevalence of sports activities, the incidence of bone-related diseases and accidents has been high [1]. In response to this tendency, bone implant therapy has become a major clinical procedure [2]. Bone implants can be used to support, replace, or stabilize damaged bones to assist in the recovery of the body, and their performance affects the treatment [3-5]. Biodegradable metals (Zn, Mg, Fe, and their alloys [6-8]) can be used as bone implant materials. Implants made of biodegradable material degrade in the body and thus, do not need to be taken out. Whereas other short or long-term implants have to be removed after the recovery of the body causing secondary damage to the human body [9].

Zinc plays a vital role in the body and it stimulates osteoclast differentiation, meanwhile, inhibiting bone resorption and resulting in increased bone strength [10]. Thus, biodegradable zinc alloys show significant advantages in orthopedic applications [11]. Also, compared to other biodegradable metals, zinc has a favorable degradation rate and low melting point, making the manufacturing process simpler [12].

Zinc foams have many advantages compared to the dense material when applied as biomedical implants. They have a similar structure as bone and their mechanical properties can be adjusted by changing their relative density. Zinc foams can be manufactured by a variety of methods, such as casting, powder metallurgy, and electrodeposition [13-15]. One way to make Zn foam is to add foaming agent evenly to the molten Zn, and then cool down to obtain a metal foam. Highly porous zinc foams can be obtained; the density of these foams is less than 20 % of the density of the bulk zinc. An often-used manufacturing method is the space holder method, both casting and powder metallurgy can be applied. In the case of the powder metallurgy, zinc powder and space holder are evenly mixed, and binder material is added. The mixture is then compacted in a mold into a desired shape, then sintered, and finally, the space holder is removed [13-15]. Sadighikia et al. [13] prepared open-cell zinc foams with 74-92 % porosity with this method using spherical urea particles of 0.5-2 mm in diameter [13]. They used ethanol as a binder to ensure that the zinc powder adhered to the urea particles. The mixture was then compacted uniaxially at 200, 300, and 400 MPa to form cylindrical samples with a diameter of 20 mm. The urea was leached out from the green body in cold water for 5 hours. After drying at 90 °C, the sample was sintered in a tube furnace at different temperatures (320 °C, 360 °C and 410 °C) for 2-4 hours under argon protective atmosphere. The results show that the compressive yield strength and elastic modulus decrease with increasing porosity and the changes can be described with the Gibson-Ashby model [16]. The optimum structural and mechanical properties of the zinc foam were obtained by compaction at 300 MPa and sintering at 410°C for 2 h. The results showed that the zinc foam had good compressive yield strength and elastic modulus.

The advantage of powder metallurgy compared to casting in the case of the space holder technique is that foams with higher porosity can be obtained. The goal of this study is to investigate the mechanical properties of zinc foam using a modified powder metallurgical method. Instead of making the foam sample in 3 steps (cold compression – leaching – sintering), we wanted to confirm if the samples can be produced in only two steps: hot pressing and then leaching out the space holder without lowering the stiffness and the compressive strength of the zinc foam. Therefore, we investigated the effects of manufacturing parameters on the compressive properties of Zn foams produced with the hot-pressing technique.

Experimental

99.5% pure zinc powder and NaCl particles in a volume ratio of 20:80 were thoroughly mixed. Subsequently, the mixture was poured into a mold coated with graphite. The blend was hot-pressed with a Teach-Line Platen Press 200E machine (Dr. Collin GmbH, Munich, Germany). The maximum temperature and pressure of the machine were 300 °C and 15 MPa, respectively. We chose for compression time for 10 min and 30 min and compression pressure for 5 MPa, 10 MPa, and 15 MPa. With each parameter set, 3 samples were produced, a total of 18 samples. After hot-pressing the blend, the outer skin of the samples was removed with grinding, and finally, the NaCl particles were then leached out from the samples to obtain the final foam structure. The average pore size was about 1 mm.

An Instron 5965 type universal testing machine (Instron Corporation, Norwood, MA, USA) was used to carry out the uniaxial compression tests at room temperature. Cylindrical specimens with a height of 10 ± 0.24 mm and a diameter of 13 ± 0.05 mm were compressed at a crosshead speed of 0.3 mm/min. The corresponding load and displacement were recorded using the Bluehill 3 software (Instron Corporation, Norwood, MA, USA).

The structure of the zinc foams was investigated by an Olympus SZX16 stereo microscope (Olympus Corporation, Tokyo, Japan) and ZEISS EVO MA 10 scanning electron microscope (SEM) (Carl Zeiss AG, Oberkochen, Germany).

The density of each foam sample was calculated as the ratio of mass to volume. The volume was obtained by measuring the height and the diameter of the foam sample with a caliper.

Results

The structure of Zn foam can be seen in Fig. 4. The pores are homogenously distributed throughout the sample.

Fig. 4 A stereomicroscope image of a sample.

Tab. 1. contains the average density of the foam samples produced with different manufacturing parameters (pressure, time). It can be seen that the density of the sample is the highest when the compression pressure is 15 MPa. When the compression time is 10 min and the compression pressure is 5 MPa, the density is the lowest. And with the same compression time, as the compression pressure increases, the density also increases slightly. Similarly, when the compression pressure is constant and the compression time is extended, the density of the sample will also increase. Compared to the sample processed for 10 minutes, the sample subjected to 30 minutes of processing shows a higher density.

Tab. 1 The properties of the samples at different compression time and compression pressure.

Parameters		Density/ (g/cm^3)	Peak stress (MPa)
10 min	5 MPa	1.5 ± 0.2	0.6 ± 0.2
	10 MPa	1.6 ± 0.2	1.1 ± 0.2
	15 MPa	1.7 ± 0.1	2.1 ± 0.4
30 min	5 MPa	1.6 ± 0.1	1.6 ± 04
	10 MPa	1.7 ± 0.2	1.9 ± 0.4
	15 MPa	1.7 ± 0.1	2.1 ± 0.4

Figure 2. shows the characteristic stress-strain curves of Zn foam produced with different compression pressures (5MPa, 10 MPa, and 15 MPa) and compression times (10 min and 30 min). The curves differ from the usual plastically deformed foams, where the quasi-linear stage is followed by a smooth plateau stage. However, the curves show similar behavior. First, the stress increases linearly with the strain to a peak stress. After the first stage, there is a stress drop in the compression curves. In the second region, erratic stress fluctuations can be observed.

The changes of the surface during compression of selected samples were video recorded (Figure 3.) Figure 3a. shows the original sample, while Fig. 6b. the sample at the end of the quasi-linear stage. It is visible, that a crack initiates at this point (see arrow in Figure 3b.). Figure 3c. shows that due to the propagation of this crack, a part of the sample starts to disintegrate and fall out. Thus, the stress drop indicates fracture in the sample. In the second region, stress fluctuations can be observed due to the brittle fracture of the cell struts (Fig. 6c-3f).

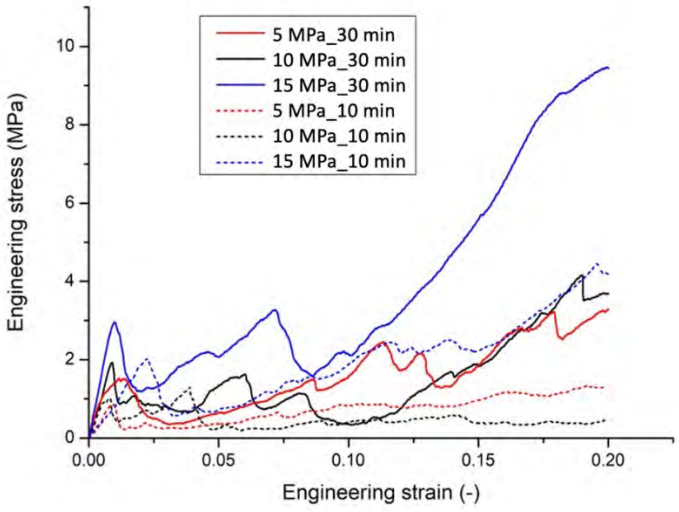

Fig. 5 Compression curves of samples up to 0.2 strain with 5 MPa, 10 MPa and 15 MPa compaction pressure.

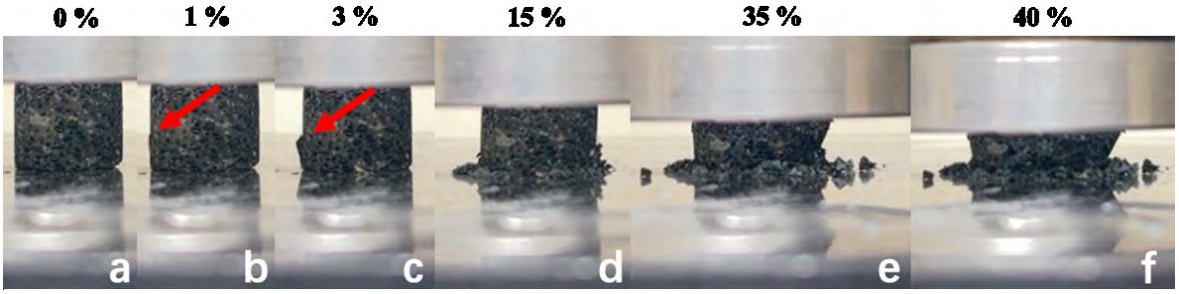

Fig. 6 Deformation of samples during compression, a) the initial state, b) at peak sress (1% strain), c)-f) during the second stage (at strain 3%, 15%, 35%, and 40%).

The scatter of the peak stress of the foams is large (Table 1), which is due to the scatter in relative density and the brittle fracture of the samples. However, the tendencies show that the higher the compression pressure, the higher the compression strength.

Discussion

Comparing the foam produced by Sadighikia et al. [13], it can be seen that the sample with a porosity of 82.3 % can reach a stress higher than 10 MPa. However, the highest peak stress we could achieve was 3 MPa. We investigated the possible reasons with SEM. Fig. 7. shows the SEM image of the zinc foam. According to the SEM images, the sintering process started, but was not as good as in the case of sintering at 410 °C for 2 hours [13]. This led to the premature fracture of the struts lowering the peak stress. It is also the cause of the wavy character of the stress-strain curve in the second stage. Another reason for the lower stresses is that by using salt particles with sharp edges, we introduced many stress-raisers into our structure.

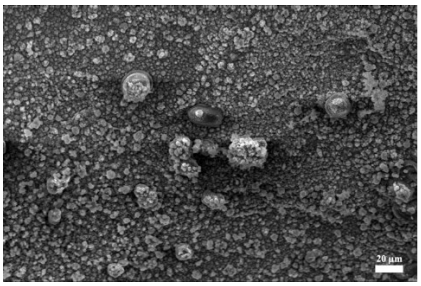

Fig. 7 The surface of Zn foam was analyzed using the SE detector at magnifications of 860x.

In some cases, we found that the time for leaching out was insufficient, as there were some salt remnants in the crumbs of some samples after compression. These remnant salt particles could cause an increase in stress at around 0.2 strain (e.g. in the case of 15MPa_30min sample in Figure 2.) However, we believe that since the salt particles found after compression were smaller than the originally used, only a few small particles could have remained in the structure. (The leaching process was not complete and not all of the salt was dissolved in the water.) Thus, their influence on the stiffness and the peak stress can be neglected.

Conclusion

We found that hot-pressing is a very promising method to make zinc foams within a short period (10 min.) and with a low energy cost compared to other powder metallurgical or casting methods. The highest compressive strength was obtained when applying 15 MPa of pressure for 30 minutes at 300 °C. The highest strength was partly due to the increased density of the foam. The compressive strength can be increased by increasing the sintering temperature or extending the compression time to fully complete the sintering of the zinc powder.

Acknowledgements

This work was supported by the Visegrad Grant from the International Visegrad Fund (project no. 22310096).

References

[1]L. Zhu, X. Tong, Z. Ye, Z. Lin, T. Zhou, S. Huang, Y. Li, J. Lin, C. Wen, and J. Ma, "Zinc phosphate, zinc oxide, and their dual-phase coatings on pure Zn foam with good corrosion resistance, cytocompatibility, and antibacterial ability for potential biodegradable bone-implant applications," *Chemical Engineering Journal,* vol. 450, pp. 137946, 2022.

[2]C. Gao, S. Peng, P. Feng, and C. Shuai, "Bone biomaterials and interactions with stem cells," *Bone research,* vol. 5, no. 1, pp. 1-33, 2017.

[3]S. H. Jariwala, G. S. Lewis, Z. J. Bushman, J. H. Adair, and H. J. Donahue, "3D printing of personalized artificial bone scaffolds," *3D printing and additive manufacturing,* vol. 2, no. 2, pp. 56-64, 2015.

[4]M. Z. Ibrahim, A. A. Sarhan, T. Kuo, M. Hamdi, F. Yusof, C. Chien, C. Chang, and T. Lee, "Advancement of the artificial amorphous-crystalline structure of laser cladded FeCrMoCB on nickel-free stainless-steel for bone-implants," *Materials Chemistry and Physics,* vol. 227, pp. 358-367, 2019.

[5]M. Kurian, R. Stevens, and K. M. McGrath, "Towards the development of artificial bone grafts: combining synthetic biomineralisation with 3D printing," *Journal of functional biomaterials,* vol. 10, no. 1, pp. 12, 2019.

[6]A. Yusop, A. Bakir, N. Shaharom, M. Abdul Kadir, and H. Hermawan, "Porous biodegradable metals for hard tissue scaffolds: a review," *International journal of biomaterials,* vol. 2012, no. 1, pp. 641430, 2012.

[7]Y. Xie, L. Zhao, Z. Zhang, X. Wang, R. Wang, and C. Cui, "Fabrication and properties of porous Zn-Ag alloy scaffolds as biodegradable materials," *Materials Chemistry and Physics,* vol. 219, pp. 433-443, 2018.

[8]L. Zhao, Z. Zhang, Y. Song, S. Liu, Y. Qi, X. Wang, Q. Wang, and C. Cui, "Mechanical properties and in vitro biodegradation of newly developed porous Zn scaffolds for biomedical applications," *Materials & Design,* vol. 108, pp. 136-144, 2016.

[9]Y.-J. Park, Y.-H. Song, J.-H. An, H.-J. Song, and K. J. Anusavice, "Cytocompatibility of pure metals and experimental binary titanium alloys for implant materials," *Journal of dentistry,* vol. 41, no. 12, pp. 1251-1258, 2013.

[10]M. Yamaguchi, "Role of zinc in bone formation and bone resorption," *The Journal of Trace Elements in Experimental Medicine: The Official Publication of the International Society for Trace Element Research in Humans,* vol. 11, no. 2‐3, pp. 119-135, 1998.

[11]X. Xiao, B. Wang, E. Liu, H. Liu, L. Liu, W. Xu, S. Ge, and J. Shao, "Investigation of zinc-silver alloys as biodegradable metals for orthopedic applications," *Journal of Materials Research and Technology,* vol. 26, pp. 6287-6303, 2023.

[12]Y. Su, J. Fu, J. Zhou, E. Georgas, S. Du, Y.-X. Qin, Y. Wang, Y. Zheng, and D. Zhu, "Blending with transition metals improves bioresorbable zinc as better medical implants," *Bioactive Materials,* vol. 20, pp. 243-258, 2023.

[13]S. Sadighikia, S. Abdolhosseinzadeh, and H. Asgharzadeh, “Production of high porosity Zn foams by powder metallurgy method,” *Powder Metallurgy*, vol. 58, no. 1, pp. 61-66, 2015.

[14]L. Pan, Y. Yang, M. U. Ahsan, D. D. Luong, N. Gupta, A. Kumar, and P. K. Rohatgi, “Zn-matrix syntactic foams: Effect of heat treatment on microstructure and compressive properties,” *Materials Science and Engineering: A*, vol. 731, pp. 413-422, 2018.

[15]K. Jayasayee, S. Clark, C. King, P. I. Dahl, J. Richard Tolchard, and M. Juel, “Cold sintering as a cost-effective process to manufacture porous zinc electrodes for rechargeable zinc-air batteries,” *Processes*, vol. 8, no. 5, pp. 592, 2020.

[16]M.F. Ashby, A. Evans, N.A. Fleck, L.J. Gibson, J.W. Hutchinson, H.N.G. Wadley, "*Metal Foams: a design guide*", Butterworth-Heinemann, 2000.

Refinement of Electrochemical Deposition Methods for Hydroxyapatite on Zinc-Based Biodegradable Materials

R. Gorejová[a]*, I. Mojžišová[a], R. Oriňaková[a]

[a] Department of Physical Chemistry, Faculty of Science, P.J. Šafárik University in Košice, Moyzesova 11, 041 54, Košice, Slovakia
*radka.gorejova@upjs.sk

Introduction

Typical representatives of the group of biodegradable medical devices are metals (Mg, Fe, Zn, e.g. [1]), ceramics (tricalcium phosphates (TCPs), hydroxyapatite (HA), bioglass, e.g. [2]), and synthetic or natural polymeric materials (polyglycolic acid (PGA), polylactic acid (PLA), collagen, gelatin, e.g.) [2,3]. Each of the groups of these materials has advantages as well as disadvantages, which can be minimized by preparing composite materials using the leading properties of the individual components. Recently, zinc (Zn) gained attention as a biodegradable metal for bone implants and cardiovascular stents [4]. Zn is an essential trace element that is involved in numerous cellular processes, including bone metabolism. In bone tissue engineering, zinc has been shown to enhance osteoblast (bone-forming cell) differentiation and mineralization, and to promote bone formation. However, pure Zn showed significant toxicity to normal human osteoblast cells with cell viability drop to lower than 50% after 7 days' culture with pure Zn extracts [5]. For these reasons, it is necessary to prepare modified materials that address these shortcomings. Hydroxyapatite (HAp) is a bioactive ceramic with great chemical structural resemblance with the human bone known for supporting cell proliferation, bone ingrowth and osseointegration. It consists mainly of calcium (Ca) phosphorus (P), which are both essential elements crucial for homeostasis retention. huge advantage of the use of HAp also lays in the extensive ability to be doped with various therepautical components (Ag, antibiotics, anti-inflammatory agents, etc.). The combination of metal and ceramic components is one of the frequent approaches used in biomaterial research. Electrochemical deposition was chosen in this work as a versatile and controllable method for depositing hydroxyapatite onto conductive zinc substrates.

Materials and Methods

Electrochemical deposition of the hydroxyapatite was carried out using an Autolab PGSTAT 302N potentiostat. The solid polished Zn sample was used as the working electrode, Ag/AgCl/KCl (3 mol/L) as the reference electrode and Pt as the auxiliary electrode. The electrolyte solution used for electrolytic deposition of the HAp layer composed of 2.5×10^{-2} mol/l $NH_4H_2PO_4$ and 4.2×10^{-2} mol/l $Ca(NO_3)_2$. Cathodic deposition was performed at a current density of 0.4 mA/cm^2 for 30 min. To address the problem of unsufficient adhesion of Hap layer onto substrate, EDTA component was used. In the first step, the chelating agent EDTA-2Na (7.5×10^{-4} mol/dm^{-3}) was added to the electrolyte solution while the HAp coating was applied under unchanged conditions (Zn-HAp/EDTA 1). In the second step, in addition to the use of EDTA-2Na, the deposition time was extended from 30 to 120 min at the original current density of 0.4 mA/cm^{-2} (Zn-HAp/EDTA 2). In the third step, the deposition current density was changed to 1.25 mA/cm^{-2} (Zn-HAp/EDTA 3). Subsequently, the coated samples were soaked in a 1 mol/l NaOH solution at a temperature of 65 °C for 2 hours, washed in distilled water and dried at a temperature of 80 °C for 2 hours.

Results

Figure 1 shows 3 types of coatings prepared during the optimization of HAp electrochemical deposition conditions under a scanning electron microscope. The figure shows images of the surface of individual samples at 50× (a, d, g), 1,000× (b, e, h) and 5,000× (c, f, i) magnifications. The hydroxyapatite coating deposited from the electrolyte enriched with EDTA-2Na (Zn-HAp/EDTA 1) formed needle-shaped crystals, between which there were irregular spherical

structures (Fig. 1c). The hydroxyapatite coating on the Zn-HAp/EDTA 2 samples consisted of formations with an irregular spherical shape (Fig. 1f). At the smallest magnification, we can see that the most homogeneous HAp coating was formed on the surface of the Zn-HAp/EDTA 3 samples, but the thickness of this coating was not even. Individual HAp crystals formed bump-like clusters in some places (Fig. 1h). Considering the homogeneity, adhesion and shape of the hydroxyapatite crystals, the coating on Zn-HAp/EDTA 3 appears to be the most suitable for further use.

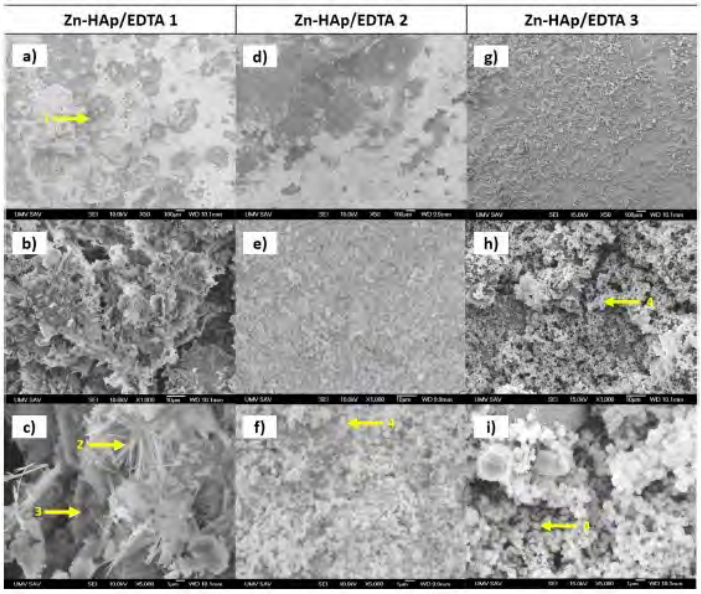

Fig. 1 SEM images of HAp coatings of samples Zn-HAp/EDTA 1 (a,b,c), Zn-HAp/EDTA 2 (d,e,f) and Zn-HAp/EDTA 3 (g,h,i), 1- disk-like structures , 2- needle-like crystals, 3- spherical formations, 4- spherical formations.

Acknowledgements

Funded by the EU NextGenerationEU through the Recovery and Resilience Plan for Slovakia under the project ZETA no. 09I03-03-V04-00010 and by the project APVV-20-0278 of the Slovak Research and Development Agency.

References

[1] Y. Liu et al. “Fundamental theory of biodegradable metals—definition, criteria, and design” *Adv. Funct. Mater.*, vol. 29, no. 18, 1805402, 2019.

[2] S. Wei et al. “Biodegradable materials for bone defect repair” *Mil. Med. Res.*, vol. 7, p. 1-25, 2020.

[3] P. Rai et al. “Recent advances in the sustainable design and applications of biodegradable polymers” *Bioresource technology*, vol. 325, 124739, 2021.

[4] J. Qian et al. “Osteogenic and angiogenic bioactive collagen entrapped calcium/zinc phosphates coating on biodegradable Zn for orthopedic implant applications” *Biomaterials Advances*, vol. 136, 212792, 2022.

[5] H. Yang et al. “In vitro and in vivo studies on zinc-hydroxyapatite composites as novel biodegradable metal matrix composite for orthopedic applications” *Acta Biomater*., vol. 71, p. 200-214, 2018.

Transition Metal Phosphides as Efficient Catalysts for Enhanced Water Splitting

A. Gubóová[a]*, M. Strečková[a], R. Oriňaková[b]

[a] Institute of Materials Research, Slovak Academy of Science, Watsonova 47, Kosice, Slovak Republic
[b] Institute of Chemistry, Faculty of Science, P.J. Safarik University, Moyzesova 11, 040 01 Kosice, Slovak Republic
*aguboova@saske.sk

Hydrogen is considered efficient renewable energy source due to its gravimetric energy density and low emissions. Among the various methods of hydrogen production, electrochemical water splitting, which involves the hydrogen evolution reaction (HER) and the oxygen evolution reaction (OER), is one of the most promising.. Currently, catalysts based on precious metals such as platinum on carbon (Pt/C), iridium oxide (IrO_2) , and ruthenium oxide (RuO_2) are considered the most effective electrocatalysts for HER and OER [1]. However, their high cost and limited availability pose significant challenges to their widespread application. In contrast, catalysts based on transition metals offer comparable catalytic performance while substantially reducing costs and minimizing environmental impact [2].Transition metals, particularly iron and molybdenum, have emerged as attractive alternatives due to their natural abundance, low cost, and excellent catalytic properties [3]. Phosphorus plays a crucial role in catalysis by modulating the electronic structure of transition metals, enhancing their catalytic activity, and improving stability. Phosphorus incorporation can significantly boost HER and OER performance by increasing electrical conductivity, optimizing binding energies, and providing a more favorable environment for the evolution reactions [4]. This combination of transition metals with phosphorus represents a promising strategy for designing cost-effective and high-performance catalysts for sustainable hydrogen production.

Bimetallic transition metal phosphides were synthesized using a scalable sol-gel method, involving the dissolution of precursor salts in citric acid followed by drying and sintering of the resulting solution. The synthesized MoFeP powder was then utilized to prepare a catalytic ink, composed of finely ground catalytic powder, Nafion, and isopropyl alcohol, which was subsequently drop-cast onto a working electrode.

Scanning electron microscopy (SEM) analysis revealed a regular structure with agglomerated particles, while energy-dispersive X-ray (EDX) spectroscopy confirmed the presence of molybdenum, iron, and phosphorus. Transmission electron microscopy (TEM) images indicated irregular particle morphology.

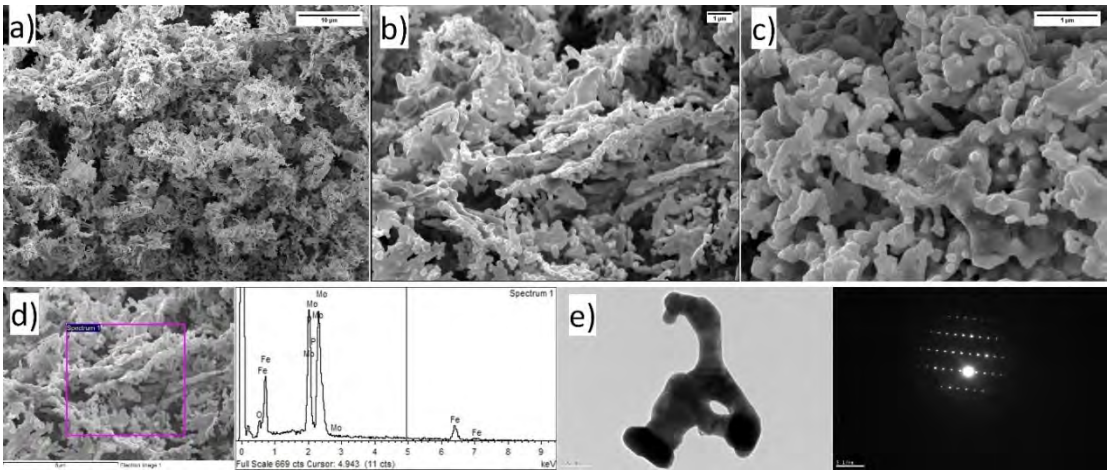

Fig. 1 Catalytic sample MoFeP a) b) c) SEM images at 2k, 10k, and 20k agnification, d) EDX analysis, e) TEM analysis.

The electrocatalytic performance of MoFeP catalytic ink for both the hydrogen evolution reaction (HER) and oxygen evolution reaction (OER) was evaluated using simulated electrolyzer measurements in an electrochemical cell, with the catalyst-coated electrode serving as both the cathode and anode. The polarization curves were recorded without iR compensation in alkaline (1 M KOH) and acidic (0.5 M H_2SO_4) environments. In alkaline media, the overpotentials required to achieve current densities of 10 mA cm^{-2} and 20 mA cm^{-2} were 1.61 V and 1.72 V, respectively, indicating favorable activity for water splitting. In acidic media, the corresponding overpotentials were 1.67 V at 10 mA cm^{-2} and 1.75 V at 20 mA cm^{-2}, suggesting that while bifunctional use may be more effective in alkaline conditions, performance at higher current densities remains comparable between the two environments.

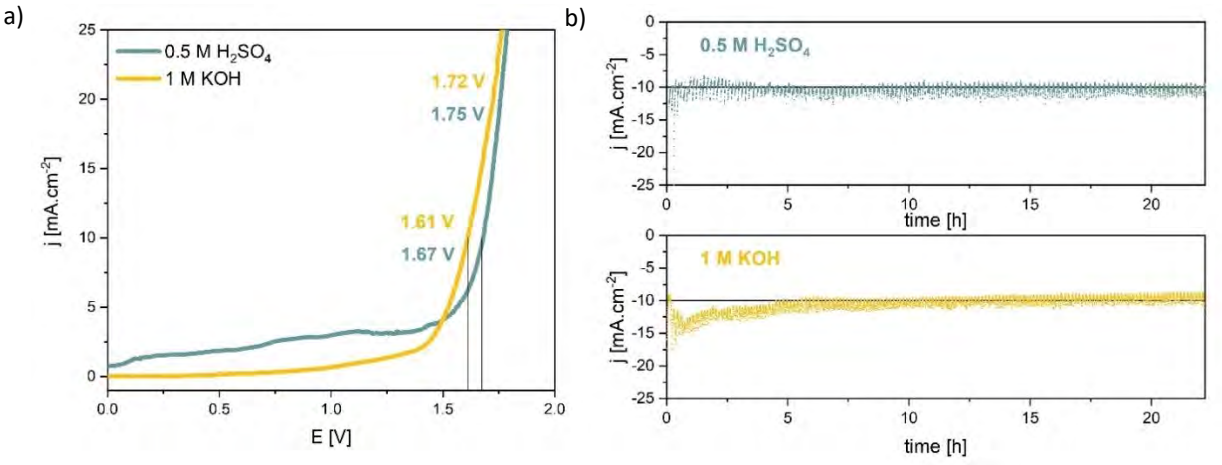

Fig. 2 a) Polarization curves of simulated electrolyser set-up in acidic and alkaline medium and b) long-term stability tests for MoFeP catalyst in acidic and alkaline medium.

Stability was assessed using chronopotentiometric measurements at -300 mV vs. RHE in 0.5 M H_2SO_4 and -500 mV vs. RHE in 1 M KOH over a period of 20 hours. The potential remained stable throughout, indicating the catalyst's robust durability. An initial drop in current density observed in the alkaline environment, followed by stabilization, suggests possible electrode activation during the initial hours. Post-stability SEM analysis confirmed minimal morphological changes, likely due to vigorous gas bubbling during the measurement process.

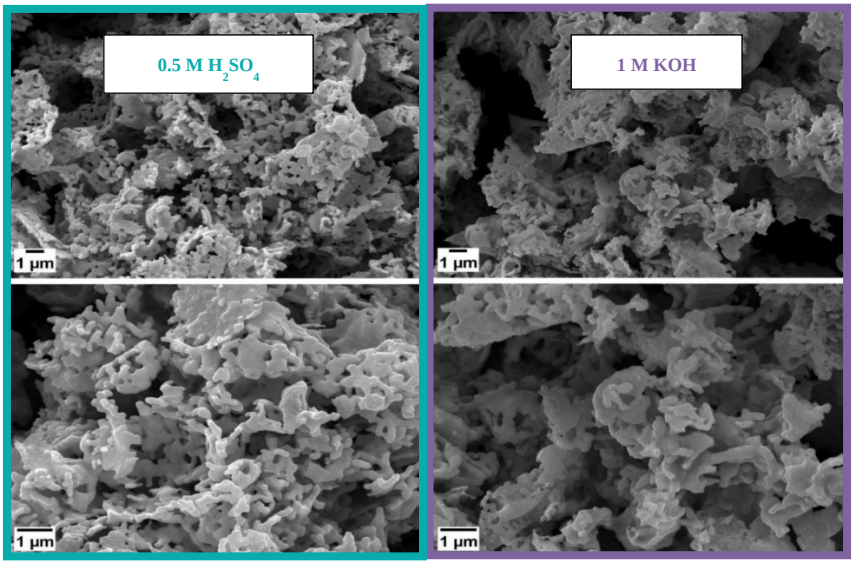

Fig. 3 SEM images of MoFeP after stability testing in 0.5 M H_2SO_4 and 1 M KOH.

In conclusion, the synthesized MoFeP bimetallic phosphide demonstrated promising electrocatalytic performance for both HER and OER in alkaline and acidic environments, with notable activity at overpotentials suitable for practical water splitting applications. Stability testing revealed that the catalyst maintained structural integrity and performance over extended operation, with minimal morphological changes observed. The results indicate that MoFeP is a robust and efficient bifunctional catalyst, particularly suited for alkaline conditions, and holds potential for integration into practical electrolyzer systems.

Acknowledgements

This work was supported by Slovak Research and Development Agency under the contract no. APVV-20-0299, and the Scientific Grant Agency of the Ministry of Education, Science, Research and Sport of the Slovak Republic no. VEGA 1/0095/21 and no.VEGA 2/0027/23.

References

[1] C. Fan, Z. Zang, X. Zhang, "Non-metal doping regulation in transition metal and their compounds for electrocatalytic water splitting," Int. J. Hydrogen Energy, vol. 56, pp. 1273-1283, 2024, doi:10.1016/j.ijhydene.2023.12.256

[2] Y. Mu, R. Ma, S. Xue, H. Shang, W. Lu, L. Jiao, "Recent advances and perspective on transition metal heterogeneous catalysts for efficient electrochemical water splitting," Carbon Neutralization, vol. 3, no.1, pp. 4-31, 2024, doi:10.1002/cnl2.105

[3] X. Peng, C. Pi, X. Zhang, S. Li, K. Huo, P. K. Chu, "Recent progress of transition metal nitrides for efficient electrocatalytic water splitting," Sustainable Energy Fuels, vol. 3, pp. 366-381, 2019, doi:10.1039/C8SE00525G

[4] C. Huang, H. Xu, T. Shuai, Q. Zhan, Z. Zhang, G. Li, "A review of modulation strategies for improving catalytic performance of transition metal phosphides for oxygen evolution reaction," Appl. Catal. B, vol. 325, p. 122313, 2023, doi: 10.1016/j.apcatb.2022.122313

Electrochemical Sensor for Cholesterol Determination

F. Chovancová[a]*, I. Šišoláková[a], M. Cvek[b], J. Shepa[a], P. Sáha[b], R. Oriňaková[a,b]

[a] Department of Physical Chemistry, Faculty of Science, Pavol Jozef Šafárik University, Moyzesova 11, 040 11 Košice, Slovak Republic
[b] Centre of Polymer Systems, Tomáš Baťa University in Zlín, Třída Tomáše Bati 5678, 760 01 Zlín, Czech Republic
*frederika.chovancova1@student.upjs.sk

Cholesterol, a crucial sterol synthesised by animal cells, is not just a passive component of our bodies. It plays a vital role in maintaining cellular membrane structure and function, influencing permeability and fluidity, and serving as a precursor for steroid hormones, bile acids, and vitamin D. This underscores the significance of our research in understanding and managing cholesterol levels. Cholesterol is transported in the bloodstream to cells by lipoproteins. There are two types of lipoproteins, high-density lipoprotein (HDL) and low-density lipoproteins (LDL), which play the key role in transporting cholesterol into cells in the blood. LDL, often called "bad" cholesterol, is associated with the plaque deposition in blood vessels, and increased blood levels indicate various vascular diseases. HDL, known as "good" cholesterol, can help reduce the risk of heart disease when it increases in the human blood [1,2].

Conversely, having higher HDL cholesterol levels can help lower the risk of heart disease. It is crucial to monitor cholesterol levels as part of managing one's health, and it is generally recommended to maintain a total cholesterol level below 200 mg/dL for optimal health. Furthermore, the level of cholesterol in the blood can serve as an indicator of various diseases, including stroke, hypertension, myocardial infarction, anaemia, brain thrombosis, arteriosclerosis or diabetes mellitus [2,3].

Traditional cholesterol measurement methods are often expensive and time-consuming, highlighting the urgent need for more simple, non-invasive alternatives. Studies in the literature utilise conventional techniques for determining cholesterol, such as High-Liquid Performance-Chromotography Ultraviolet (HPLC-UV), infrared spectroscopy, Nuclear Magnetic Resonance Spectroscopy (NMR) or Raman spectroscopy and more. However, these techniques have some drawbacks, including their relatively high cost, long analysis time, requirement for trained personnel and inability to perform on-site analysis. Therefore, new techniques need to be developed that are cost-effective, sensitive, specific, easy to apply, and have a short analysis time [4]. Electrochemical sensors show potential for these types of analysis. They offer several advantages over conventional methods, including fast and accurate response, enabling sensitive and selective analysis, achieving low detection limits, requiring small amounts of analyte, and being portable. Electrochemical sensors are small analytical devices that can specifically detect target analytes and enable selective analysis. Various cholesterol sensors have been developed in the last decade, including enzymatic and nonenzymatic sensors. Enzymatic sensors, which utilise enzymes such as cholesterol oxidase (ChOx) or cholesterol esterase (ChE), offer high sensitivity and selectivity. However, they are prone to enzyme denaturation, have limited lifespans, and are sensitive to temperature, pH, and toxic substances. On the other hand, nonenzymatic cholesterol sensors address these limitations by employing electrode surfaces modified with metals, metal oxides, or composites as electrocatalysts. These sensors introduce nanomaterials with high surface-to-volume ratios, facilitating strong interaction with external reagents, high conductivity, and excellent biocompatibility, making them promising components for the miniaturisation of electrochemical devices [3,5,6].

In this study, screen-printed carbon electrodes (SPCEs) were modified by nickel particles (Ni(PLA)/SPCE). The nickel particles were produced using Pulse Laser Ablation (PLA) and then subjected to 40 minutes of ultrasonication in a phosphate buffer solution (PBS) with chitosan. 10 μL suspension of the particles was applied on the surface of working carbon electrode, then left to air dry at room temperature for 1 hour. The nickel particles were activated under alkaline conditions (0.1 M NaOH) via Cyclic Voltammetry (CV) for eight cycles within a potential window between 0.1 V to 0.7 V. The electrooxidation process of cholesterol at the nickel-modified SPCE involves the electrochemical oxidation

of cholesterol to cholestenone with the assistance of NiOOH, which is simultaneously reduced to NiO. Using Cyclic Voltammetry (CV), we delved into the electrochemical determination of various cholesterol concentrations. For the experiments, different concentration levels of cholesterol were prepared in Human Fetal Serum to simulate physiological conditions. The experimental conditions for CV were carefully set up: the potential window was maintained at - 1.5 V to 1.5 V, and the scan rate was set up at 50 mV/s (Fig.1A). Data analysis reveals that cholesterol undergoes oxidation at a potential of -0.16 V on the modified SPCE. The reduction peaks at a potential of 0.86 V were observed during our study. The current peak versus cholesterol concentration at -0.16 V potential was fitted with a colleration coefficient $R^2 = 0.97$, indicating excellent cholesterol detection (Fig.1B). Based on this data, the analytical characteristics for Ni(PLA)SPCE for cholesterol oxidation were calculated. The limit of detection (LOD) is 0.27 mM, with a linear range from 2 mM to 10 mM, and selectivity is 8.37E-6 A/mM. The correlation coefficient values for the current peak at potential 0.86 V were determined as $R^2 = 0.99$ (Fig. 1C). Screen-printed carbon electrodes modified by Nickel particles prepared by PLA demonstrate excellent analytical properties for direct and fast cholesterol detection in Human Fetal Serum.

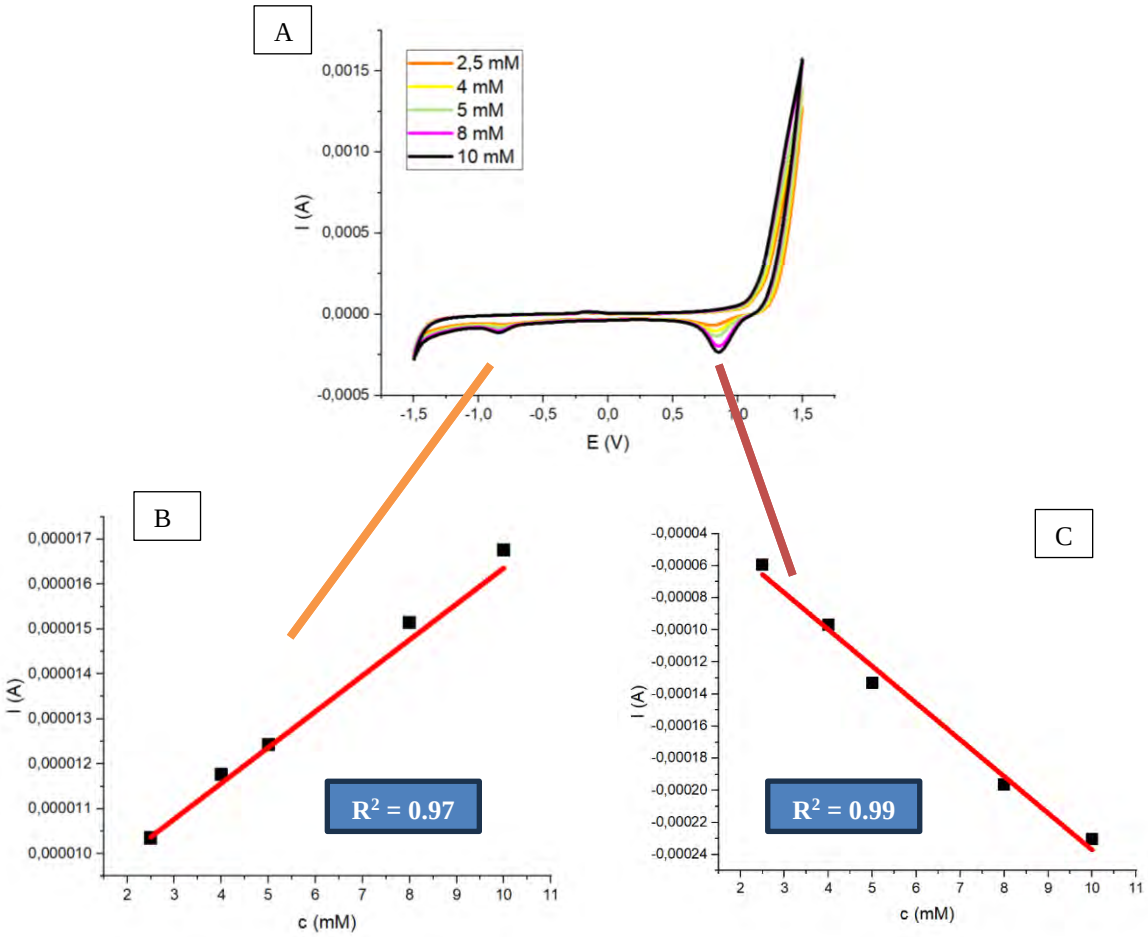

Fig. 8 Cyclic voltammetry of electrochemical cholesterol oxidation in various concentrations at Ni(PLA)SPCE. Scan rate at 50 mV/s and potential window from – 1.5 V to 1.5 V (A). Linear fitted anodic peaks vs concentration (B) and cathodic peaks vs concentration (C).

Acknowledgements

This work has been supported by project number G6106 by NATO Science for Peace and Security programme and Funded by the EU NextGenerationEU through the Recovery and Resilience Plan for Slovakia under the project No. 09I03-03-V05-00008 through International Scientific Grant System – ESGD Program of Pavol Jozef Šafarik University in Košice (vvgs-2023-2803).

References

[1]O. Domínguez-Renedo, A. M. Navarro-Cuñado, and M. A. Alonso-Lomillo, "Electrochemical devices for cholesterol detection," *J pharm Biomed Anal.,* vol. 224, Feb. 2023, doi: 10.1016/j.jpba.2022.115195.

[2]A. N. Sekretaryova, V. Beni, M. Eriksson, A. A. Karyakin, A. P. F. Turner, and M. Y. Vagin, "Cholesterol self-powered biosensor," *Anal Chem.*, vol. 86, no. 19, pp. 9540–9547, Oct. 2014, doi: 10.1021/ac501699p.

[3]V. Narwal, R. Deswal, B. Batra, V. Karla, R. Hooda, M. Sharma, J.S. Rana, "Cholesterol biosensors: A review," *Steroids.,*vol. 143, pp. 6-17, Mar. 2019, doi: 10.1016/j.steroids.2018.12.003.

[4]K. Pramanik, P. Sarkar, D. Bhattacharyay, and P. Majumdar, "One Step Electrode Fabrication for Direct Electron Transfer Cholesterol Biosensor Based on Composite of Polypyrrole, Green Reduced Graphene Oxide and Cholesterol Oxidase," *Electroanalysis,* vol. 30, no. 11, pp. 2719–2730, Nov. 2018, doi: 10.1002/elan.201800318.

[5]A. Wisitsoraat, C. Karuwan, K. Wong, D. Phokharatkul, P. Sritongkham, and A. Tuantranont, "High sensitivity electrochemical cholesterol sensor utilizing a vertically aligned carbon nanotube electrode with electropolymerized enzyme immobilization," *Sensors,* vol. 9, no. 11, pp. 8658–8668, Nov. 2009, doi: 10.3390/s91108658.

[6]H. M. Yadav, J. D. Park, H. C. Kang, and J. J. Lee, "Recent development in nanomaterial-based electrochemical sensors for cholesterol detection," *Chemosensors.,* vol. 9, May. 2021, doi: 10.3390/chemosensors9050098.

Mixed Matrix Membranes Based on Polyimide 6FDA-BisP - Preparation, Characterization and Mathematical Modelling

K. Iablochkin[a], V. Fila[a]*

[a] Department of Inorganic Technology, University of Chemistry and Technology Prague, Technicka 5, Prague 6, Czech Republic
*Vlastimil.Fila@vscht.cz

Introduction

Membrane technologies offer an alternative to conventional separation methods for gas separation. CO_2 separation from gas mixtures is used in processes such as biogas purification or raw natural gas treatment. The incorporation of fillers into the polymer matrix improves the gas separation performance of polymeric materials, leading to an increase in overall process efficiency.

The development of novel mixed matrix membranes based on 6FDA-BisP with fillers such as UiO-66 and ZIF-8 and the development of a mathematical model of the membrane separation module are the main objectives of this contribution. Methods such as XRD, BET, FTIR, TGA, DSC, SEM and EDS were used to characterize the prepared MMMs and their nanoparticles. The effects of mass content and type of inorganic fillers on the separation characteristics and morphology of the prepared membranes were investigated. Permeation measurements were performed with a gas mixture containing CO_2/CH_4 at different ratios (1/1; 3/1; 1/3) under different pressures (2, 4, 6 and 8) bar.

Experimental

A classical two-step polymerization method was used to synthesize 6FDA-BisP polyimide. In the first step, the diamine and dianhydride were reacted in a polar solvent under an N_2 atmosphere to give the poly(amic acid) solution (PAA). In the second step, the imidization process of the PAA through thermal annealing at 250 ^oC was realized. Dense membranes were prepared from 1 wt.% solution using chloroform as solvent. The obtained solution was stirred on a magnetic stirrer for 24 h. The homogeneous solution was then poured onto a Petri dish and dried under laboratory conditions for 2 days. Finally, the membranes were dried at 110 °C for 24 h.

The mathematical model of the membrane separation module with co-current flow arrangement was developed based on the mass balances of the retentate and permeate compartments. The plug flow pattern is assumed for both compartments of the module. The solution diffusion model is used to describe the mass transfer across the membrane and the permeability values calculated from experimental measurements are used. The final macrohomogeneous model is described by a set of ordinary differential equations (ODEs). The sensitivity analysis allows us to evaluate the effect of membrane area, feed composition and operating conditions (retentate and permeate side pressures) on the module performance.

Results and discussion

FTIR, TGA-DSC, EDS, SEM and XRD methods were used to analyze the chemical composition, temperature stability and morphology of the prepared particles and membranes. Furthermore, the influence of the used filler, of the composition of the feed mixture and the pressure in the range from 2 to 8 bar on the separation efficiency of the membranes are discussed. The thickness of the prepared membranes ranged from 20 to 25 μm. For the 6FDA-BisP matrix polymer with 15 wt.% ZIF-8 filler, the permeability value increased by 335 % compared to the neat membrane, while maintaining the original selectivity. For the membrane with 15 wt.% UiO-66 particles, the permeability value

increased by 155 %, maintaining the same selectivity as the neat membrane. The best permeability value was shown by the membrane with 15 wt.% ZIF-8 particles - 135 Barrer and selectivity 43. A membrane separation model is developed to design membrane separation processes, optimize operating conditions and predict behavior. The implementation of this model in the universal simulation program Aspen Plus provide us the basic view on the applicability of the developed membrane in the real industrial application, allow us to realize sensitivity analysis, optimise the design of the module and the unit.

8th International Conference on Novel Materials Fundamentals and Applications
High Tatras, 13.-16.10.2024

Electrochemical Detection of Viruses

N. Jašňáková[a]*, J. Shepa[a], I. Šišoláková[a]

[a]Department of Physical Chemistry, Faculty of Science, Pavol Jozef Šafárik University, Moyzesová 11, 04011 Košice, Slovak Republic
*nikola.jasnakova@student.upjs.sk

Introduction

Electrochemical detection techniques are crucial for accurate virus identification and the prevention of pathogen transmission, particularly during pandemics such as COVID-19 [1]. Given the rapid spread of biological components of viruses in a highly mobile world, it is essential to develop new sensors with high sensitivity, speed, accuracy, and early detection capabilities to mitigate future pandemics [2]. Current sensors are enhanced with various nanomaterials and biomolecules. Streptavidin, a biomolecule noted for its strong interaction with biotin, has gained prominence in recent years. This interaction is leveraged in aptasensors, which can create efficient charge transfer complex [3]. Aptamers, short nucleotide sequences with high specificity and stability, are increasingly used in detection due to their ability to selectively bind target molecules, which enhances detection accuracy and sensitivity. Electrochemical sensors are chosen for their ability to provide rapid, sensitive measurements with low cost and ease of application in practical settings. The interaction between aptamer sequences and streptavidin allows for the creation of efficient charge transfer complexes, improving sensor performance.This research focuses on the development of an advanced electrochemical biosensor for the detection of SARS-CoV-2, utilizing an aptamer immobilized on screen-printed carbon electrodes (SPCE) functionalized with streptavidin-modified surfaces.

Experiment

The study employed screen-printed carbon electrodes (SPCE) from Metrohm DropSens, featuring a three-electrode system printed on a ceramic substrate with dimensions 3.4 cm x 1 cm x 0.05 cm and a working electrode diameter of 4 mm. These electrodes were pre-modified with streptavidin. To next modified the electrodes, 10 µl of aptamer solution was added and the creating bind process took one hour at 5 °C. Three aptamers were tested: Apt CoV2-RBD-1, Apt CoV2-RBD-1 5AA, and Apt CoV2-RBD-4C 5AA. Electrochemical measurements were performed using a 5 mM solution of $K_3[Fe(CN)_6]/K_4[Fe(CN)_6]$ in 1M KCl, with a solution volume of 50 µl.. After initial measurements, spike protein was introduced in varying concentrations (5 µl, 2 µl, 1 µl, 0.5 µl, 0.2 µl, 0.05 µl) and measurements were repeated. Creating bind process took half hour at 5 °C. Additionally, bovine serum albumin (BSA) was used to evaluate potential interference.

Discussion

The sensor development involved aptamers immobilized on SPCEs functionalized with streptavidin-modified surfaces. Among the aptamers tested, Apt CoV2-RBD-4C 5AA was identified as the most suitable, with the sequence [Btn]TATCCAGAGTACGCAGCACCGACCTTGTGCTTTGGGAGTGCTGGTCCAAGGGCGTTAATGGACA.
The effective binding of the aptamer to the streptavidin-modified SPCE was confirmed using atomic force microscopy (AFM) and quantified by the Randles-Sefcik equation.

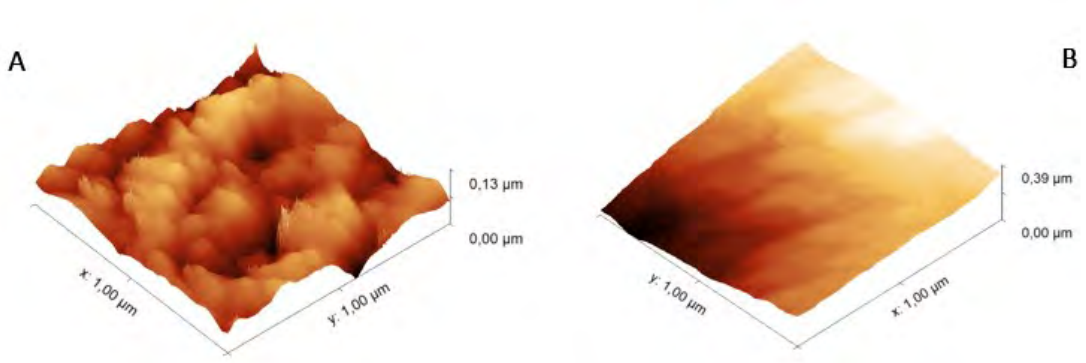

Fig. 2 AFM images of streptavidin electrode before modification(A) and after modification with aptamer and spike protein (B).

AFM images (Fig. 1) show that the streptavidin electrode has a slightly jagged surface, whereas the modified electrodes with aptamers or spike protein exhibit a rougher texture with grainy coverage (Tab. 1).

Tab. 2 Electrode surface morphology described by AFM.

	roughness	max hight	surface area
SPCE + str.	56.3 nm	133.2 nm	1.932 µm^2
SPCE + str. + apt. 3	142.3 nm	209.5 nm	1.916 µm^2
SPCE + str. + apt. 3 + spike protein	214.1 nm	388.4 nm	1.185 µm^2

The active area of the most effective sensor, Apt CoV2-RBD-4C 5AA, in the presence of spike protein was 16.1 mm².

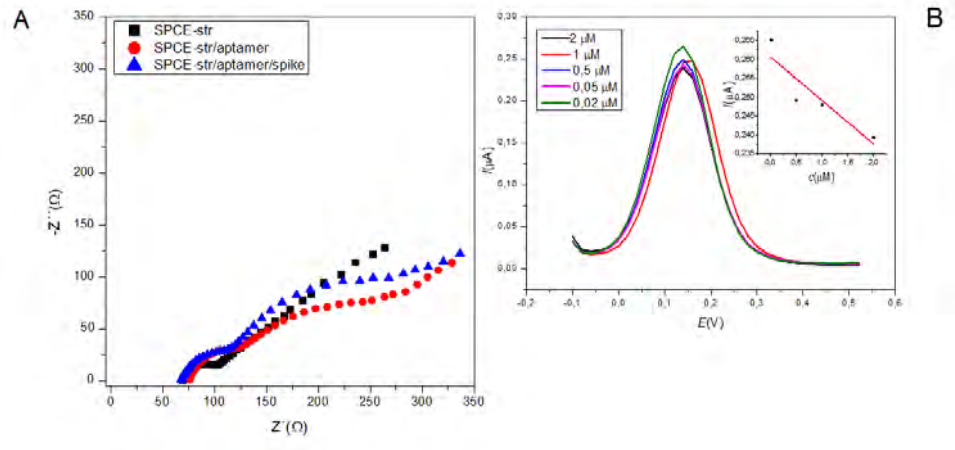

Fig. 3 A) Nyquist diagram for 3 electrode modifications. B) DPV graphs for different spike protein concentration, Inset: Calibration curve.

Electrochemical impedance spectroscopy (EIS) and differential pulse voltammetry (DPV) were employed for characterization. Results indicated a significant decrease in electrode active area following spike protein binding, attributed to the size of the spike proteins, which reduced conductivity and blocked electron transfer. From the graph (Fig. 2A), it is evident that after binding of the spike protein to the streptavidin SPCE with aptamer, the active area of the electrode decreased significantly. This phenomenon occurred due to the size of the spike proteins that occupied the surface of the electrode, thereby reducing the conductivity and blocked the active electron transfer at the phase interface. The calibration curve (Fig. 2B) shows a linear range from 20 nM to 2 μM with a sensitivity of 0.011 μA/μM. Sensor stability was assessed at 7 and 14 days. Bovine serum albumin (BSA) testing showed negligible interference with spike protein detection. Future work will involve testing the sensor with real human samples.

Acknowledgements

This work was supported by the Slovak Research and Development Agency (project PP-COVID-20-0036) and NATO SPS Call for Proposals 2023-1, G6106.

References

[1]A. Gowri, N. Ashwin Kumar, and B. S. Suresh Anand, "Recent advances in nanomaterials based biosensors for point of care (PoC) diagnosis of Covid-19 – A minireview," *TrAC Trends in Analytical Chemistry*, vol. 137, p. 116205, Apr. 2021, doi: 10.1016/J.TRAC.2021.116205.

[2]Z. Rahmati, M. Roushani, H. Hosseini, and H. Choobin, "Label-free electrochemical aptasensor for rapid detection of SARS-CoV-2 spike glycoprotein based on the composite of Cu(OH)2 nanorods arrays as a high-performance surface substrate," *Bioelectrochemistry*, vol. 146, 2022, doi: 10.1016/j.bioelechem.2022.108106.

[3]J. Shepa, I. Šišoláková, M. Panigaj, D. Bilá, P. Jarčuška, and R. Oriňaková, "Electrochemical Biosensors for Soluble Epidermal Growth Factor Receptor Detection," *Electrocatalysis*, vol. 13, no. 5, 2022, doi: 10.1007/s12678-022-00740-8.

8th International Conference on Novel Materials Fundamentals and Applications
High Tatras, 13.-16.10.2024

Development of a Novel Bifunctional, pH-Responsive Bone Implant Based on a Zeolite-Chitosan-Bisphosphonate Complex for Osteoporotic Fracture Treatment

P. Kazimierczak[a]*, A. Wójcik[a], J. Matusiak[b], R. Panek[b], M. Trzaskowska[a], M. Wójcik[a], W. Franus[b], A. Przekora[a]

[a] Department of Tissue Engineering and Regenerative Medicine, Medical University of Lublin, Chodzki 1 Street, 20-093 Lublin, Poland
[b] Department of Construction Materials Engineering and Geoengineering, Faculty of Civil Engineering and Architecture, Lublin University of Technology, Nadbystrzycka 40 Street, 20-618 Lublin, Poland
*paulina.kazimierczak@umlub.pl

Introduction and aim of study

Bone is a dynamic tissue that undergoes continuous remodeling, where osteoclasts (bone-resorbing cells) remove damaged or old bone, and osteoblasts (bone-forming cells) subsequently replace it with new tissue. When the balance between bone resorption and bone formation is disrupted, osteoporosis can develop. Bisphosphonates are widely used antiresorptive drugs that inhibit osteoclast recruitment, differentiation, and induce osteoclast apoptosis. These drugs are primarily administered orally, however, long-term use is associated with serious complications such as gastrointestinal issues, hypocalcemia, and kidney failure [1], [2].

The aim of this study was to develop a novel, bifunctional, pH-responsive zeolite-chitosan-bisphosphonate complex-based implant for osteoporotic fracture treatment. To enhance bone formation, Ca^{2+} and Mg^{2+} ions were introduced into the zeolite structure through an ion-exchange process, replacing Na^{+} ions. These ions are known to promote osteoblast adhesion and bone-forming activity. Bisphosphonate (risedronate sodium) was incorporated into the zeolite structure using chitosan molecules as a linker. After implantation, the acidic pH (~4.0-4.5) that occurs during osteoclast-mediated bone resorption will dissolve the chitosan linker and trigger the release of the drug into the bone environment, thereby inhibiting osteoclast activity. As a result, the developed bifunctional pH-responsive bone implant is designed to simultaneously reduce bone resorption by osteoclasts and support bone regeneration at the implantation site.

Materials and methods

Synthesis of pH-responsive zeolite-chitosan-bisphosphonate complex

Firstly, zeolite Na-X was synthesized from Si and Al-rich solution obtained during hydrothermal reaction of sodium hydroxide aqueous solution with fly ash. Synthesis process was performed on existing laboratory stand for zeolite synthesis (Patent No. 224734). The synthesis process was carried out at the temperature 70-90°C for 24-48 hours using 2-3M sodium hydroxide solution. The synthesized zeolite representing Na ionic form (the main cation exchangeable in the structure) was subjected to the ion exchange process with calcium and magnesium ions using $CaCl_2$ and $MgCl_2$ solutions. Then, the zeolite was functionalized with chitosan and bisphosphonate molecules (risedronate sodium) were attached. The production method of pH-responsive zeolite-chitosan-bisphosphonate complex is described in Polish patent application no. P.449563.

Fabrication of bone implant

Bone implant containing a zeolite-chitosan-bisphosphonate complex was produced based on Polish patent application no. P.449565 by application of sodium bicarbonate ($NaHCO_3$) as porogen (gas-foaming agent) and freeze-drying technique. Briefly, chitosan was dissolved in acetic acid, then appropriate amounts of agarose, hydroxyapatite,

$NaHCO_3$, and zeolite-chitosan-bisphosphonates complex were added and mixed. Obtained foam-like paste was transferred into mold, and then subjected to freezing followed by the lyophilization process.

Evaluation of surface topography

Surface topography of the fabricated bone implant was visualized using a stereoscopic microscope (Olympus SZ61TR, Olympus Polska Sp. z o. o., Poland) and a scanning electron microscope (SEM, JEOL JCM-6000Plus, Japan).

Evaluation of stability and pH-responsive behaviour of zeolite-chitosan-bisphosphonate complex in bone implant

Stability and pH-responsive behaviour of zeolite-chitosan-bisphosphonate complex in bone implants were determined using PBS with pH 7.4 and citrate buffer of pH 4.0, respectively. Biomaterials weighing ~100 mg were incubated in 20 ml of PBS or citrate buffer at 36.6 ℃, then samples were collected at determined time intervals to evaluate drug concentration by measuring absorbance at 262 nm.

Evaluation of biocompatibility in vitro

Normal human fetal osteoblast cell line (hFOB 1.19, ATCC-LGC Standards, UK) was used to assess the biocompatibility of the fabricated bone implant. hFOB 1.19 cells were cultured in a 1:1 mixture of DMEM/Ham's F12 medium without phenol red (Sigma-Aldrich Chemicals, Poland), supplemented with 10% foetal bovine serum (Pan-Biotech GmbH, Germany), 1% antibiotic solution (100 U/mL penicillin and 100 µg/mL streptomycin), and 0.3 mg/mL G418 (Sigma-Aldrich Chemicals, Poland), and maintained at 34 ˚C with 5% CO_2 in an air atmosphere.

The cytotoxicity of the bone implant was evaluated in direct contact with the osteoblasts through LIVE/DEAD fluorescent staining of the cells cultured on the biomaterial, followed by observation with a confocal laser scanning microscope (CLSM). Cell proliferation was assessed qualitatively by CLSM observation after fluorescent staining of the cytoskeleton with AlexaFluor® 635 phalloidin and cell nuclei with DAPI on the 3rd and 7th days of culture on the bone implant surface.

Results

Evaluation of surface topography

The surface topography of fabricated bone implant was visualized using a stereoscopic microscope and SEM (Figure 1). The stereoscopic microscope image showed that the biomaterial possessed a rough and ragged microstructure with high surface roughness (Figure 1a). In turn, the SEM image revealed the highly macroporous microstructure of the fabricated bone implant (Figure 1b), comparable to cancellous bone.

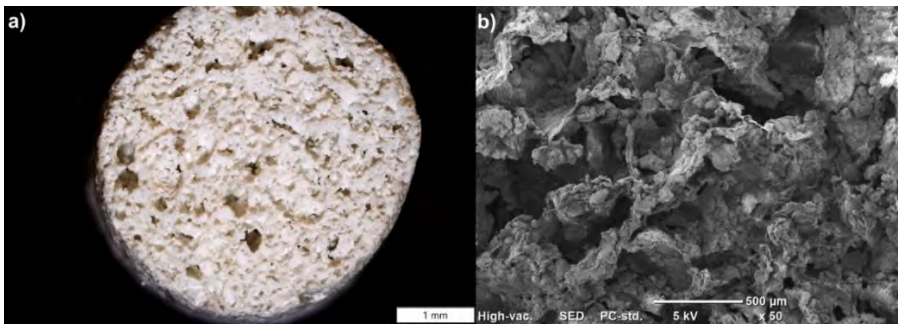

Fig. 1 Surface topography of the fabricated bone implant visualized by a) a stereoscopic microscope and b) a scanning electron microscope.

Evaluation of stability and pH-responsive behaviour of zeolite-chitosan-bisphosphonate complex in bone implant

The zeolite-chitosan-bisphosphonate complex in bone implants demonstrated high stability at pH 7.4, as no release of risedronate sodium from the biomaterials was detected. Conversely, a slow release of the drug from the fabricated bone implants was observed at pH 4, indicating the pH-responsive behaviour of the zeolite-chitosan-bisphosphonate complex.

Evaluation of biocompatibility in vitro

To evaluate the biological response to a bifunctional, pH-responsive bone implant , the biomaterial was subjected to a cytotoxicity test and assessment of osteoblast growth on its surface (Figure 2). Figure 2a shows live/dead staining of osteoblasts cultured on the biomaterial surface for 48 hours. The obtained CLSM image revealed numerous viable cells (green fluorescence) and only single dead cells (red fluorescence), confirming the non-toxicity of the biomaterial. Osteoblast growth on the surface of the developed bone implant was qualitatively assessed using fluorescent staining of cell cytoskeleton and nuclei (Figure 2b). A significant increase in cell number over time was observed, demonstrating that the biomaterial supports cell proliferation.

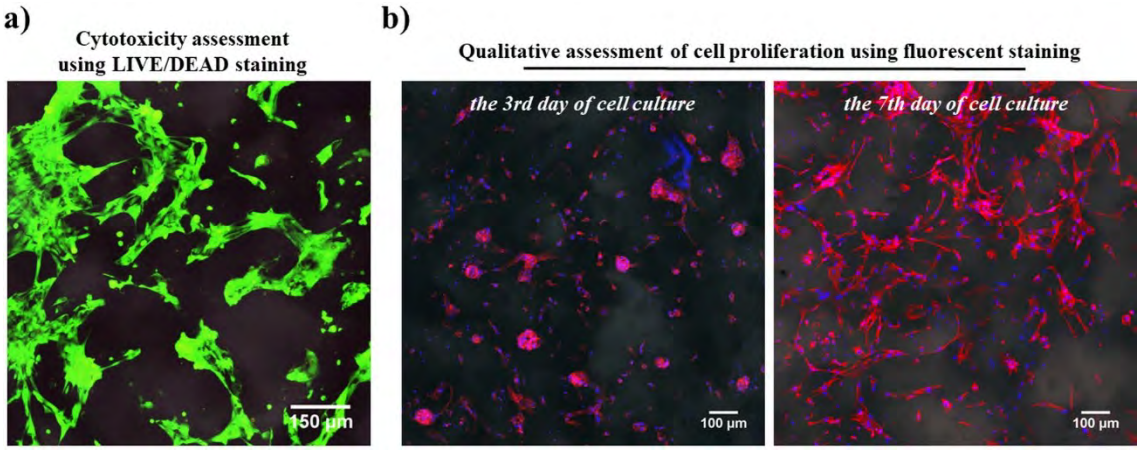

Fig. 2 Assessment of biomaterial biocompatibility *in vitro*: a) CLSM image showing LIVE/DEAD staining of hFOB 1.19 cells cultured on the surface of the bone implant for 48 hours (viable cells – green fluorescence, dead cells – red fluorescence); b) CLSM images showing the growth of hFOB 1.19 cells cultured on the surface of the bone implant for 3 and 7 days (nuclei – blue fluorescence, cytoskeleton filaments – red fluorescence).

Conclusions

The obtained results showed that the developed novel, bifunctional, pH-responsive zeolite-chitosan-bisphosphonate complex-based implant has a macroporous microstructure with high surface roughness, promoting good osseointegration of the bone implant with host tissue and enabling effective oxygenation. Additionally, the bonding between zeolite and risedronate sodium in the zeolite-chitosan-bisphosphonate complex is pH-responsive, as it is stable at physiological pH 7.4, however chitosan is soluble at pH 4, releasing the drug into the environment. Moreover, the developed bone implant is highly biocompatible, making it a promising candidate for use as a bifunctional smart bone implant containing a pH-responsive zeolite-chitosan-bisphosphonate complex for osteoporotic fracture treatment. The implant can reduce osteoclast activity through the release of bisphosphonate and, due to the presence of Ca^{2+} and Mg^{2+} ions, enhance bone formation at the implantation site

Acknowledgements

This research was funded by the National Science Centre (NCN) in Poland within OPUS 22 grant no. UMO-2021/43/B/NZ7/00447.

References

[1]H. Bi et al., "Key triggers of osteoclast-related diseases and available strategies for targeted therapies: A review," *Front Med (Lausanne)*, vol. 4, pp. 1–10, 2017, doi: 10.3389/fmed.2017.00234.

[2]T. Sozen, L. Ozisik, and N. Calik Basaran, "An overview and management of osteoporosis," *Eur J Rheumatol*, vol. 4, no. 1, pp. 46–56, 2017, doi: 10.5152/eurjrheum.2016.048.

Friction Welding of Hybrid Composite Metal Foam-filled Tubes

A. Kemény[a,b]*, G. Pados[a,b], I.N. Orbulov[a,b]

[a] Department of Materials Science and Engineering, Faculty of Mechanical Engineering, Budapest University of Technology and Economics, Műegyetem rkp. 3., H-1111 Budapest, Hungary
[b] MTA-BME Lendület "Momentum" High-performance Composite Metal Foams Research Group, Műegyetem rkp. 3., H-1111 Budapest, Hungary
*kemeny.alexandra@gpk.bme.hu

Introduction

Nowadays, sandwich panels with solid face panels are typically produced instead of simple metal foam sheets, or functional structures are made in the form of closed hollow sections or hollow castings, which are supported from the inside by the foam core [1]. An example is a developed foam-filled bumper, which protects passengers in the event of an accident, reducing the damage and the associated repair costs [2].

It is known that composite metal foams (CMFs) have higher strength properties than their 'conventional' counterparts, as the cells are typically formed by ceramic or metallic hollow particles, providing support in the event of mechanical impact [3]. It may be practical to create high-strength bonds between such structures, but the ceramic fillers significantly reduce their weldability and solderability properties. There are few publications on the welding of metal foams in the literature [4]. For the welding of composite metal foams, publications can be found in which the filler and matrix material are nearly identical [5]. As a consequence, the filler does not cause significant problems in the bond formation, but the strength increase cannot be achieved as high as when using ceramic filler.

In this research, the weldability of hybrid composite metal foam structures using a low-cost ceramic filler was evaluated. The fabricated hybrid metal foams were joined by friction welding and its structural properties were investigated.

Materials and methods

Production of foam-filled tubes

The hybrid composite metal foam-filled tubes (FFTs) were produced by low-pressure infiltration method. Using this process, the authors have already successfully produced in-situ foam-filled tubes with high wall thickness from the detailed aluminium alloys in one step [6], and in-situ foam-filled steel tubes with low wall thickness [7]. Low-cost ceramic fillers (~Ø3 mm lightweight expanded clay aggregate particles (LECAPs)) were used to create the composite structure and similar sized salt particles were used to locally create a dense open cell structure which latter can be dissolved with water after the infiltration. The FFTs with such a hybrid structure (partly filler and partly open cell) were produced in AlMgSi0.5 precipitation hardening thin-walled (1.5 mm) tubes with outer dimensions of Ø25×160 mm by placing the fillers inside the tube, and preparing the steel mould around them by filling up the empty spaces with casting sand in order to prevent the aluminium infiltration around the tubes. The prepared mould was pre-heated in a ProThermo Hofmann B-70 box furnace at 530°C and an IND IF-10 induction heating furnace was used to melt the AlSi12 quasi-eutectic alloy. The infiltration occurred by pouring the 650°C AlSi12 into the mould and applying 3.5 kPa Ar gas pressure for 5 seconds. Figure 1. shows the produced FFTs, indicating the open and closed cell regions of the specimens. The open-cell side of the fabricated aluminium alloy matrix FFT structures are more easily weldable, in addition to retaining the higher strength properties of composite metal foams.

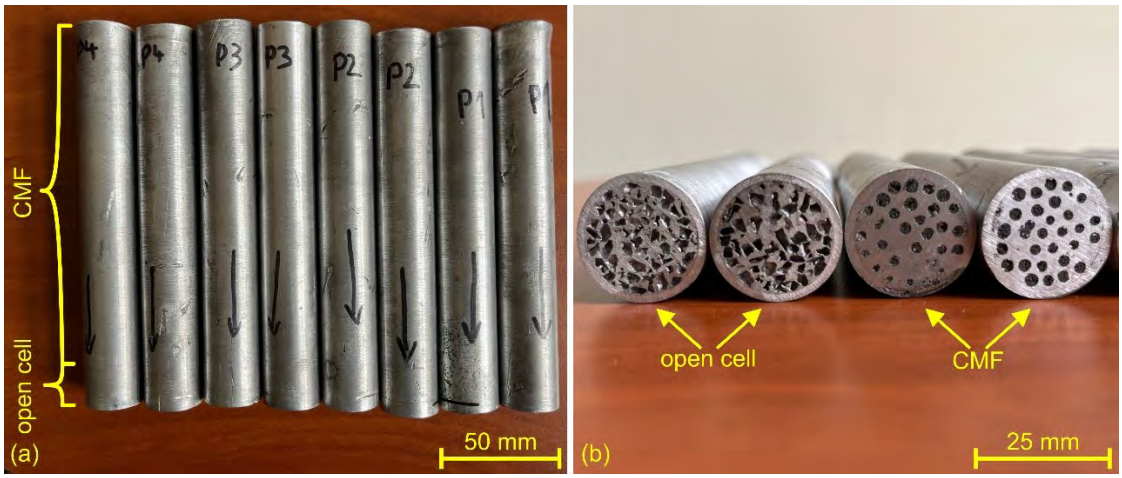

Fig. 1 In-situ produced hybrid composite metal FFTs for friction welding, showing the inner structural layout (a) and cut surfaces with open cell and CMF structures (b).

Welding

The cohesive connection between the specimens were created by friction welding, at the Harlo Ltd., using a custom DHL-100-3 type equipment of the company. The axial force of the welding machine can be set between 14 kN and 140 kN. The welding setup and the process parameter changes are shown in Figure 2.

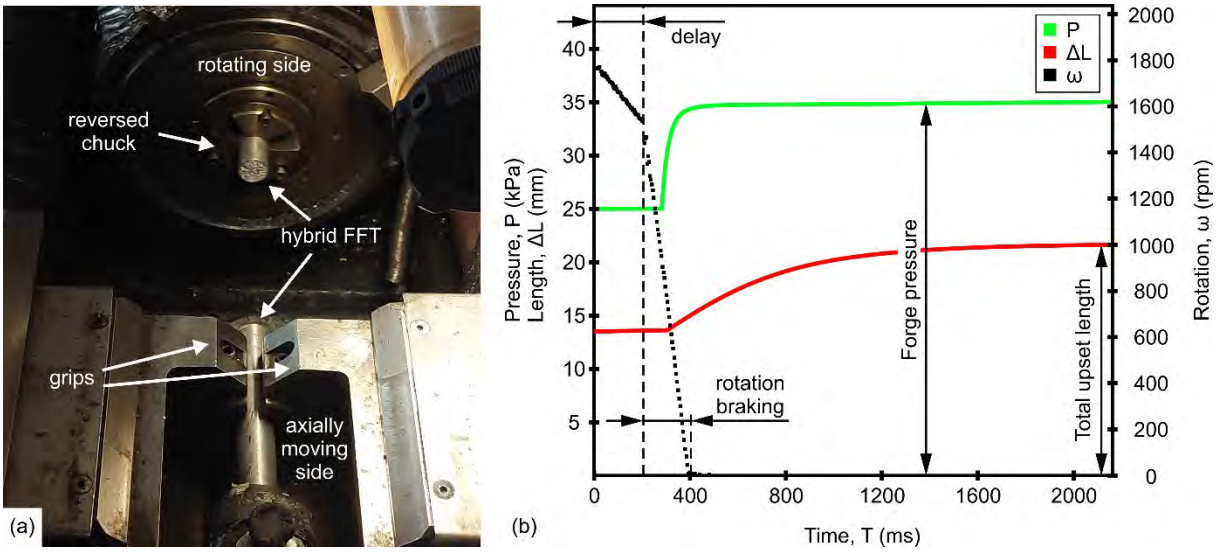

Fig. 2 Layout of the specimens before welding (a) and parameter changes during the friction welding procedure (b).

The bond was created between the heated sides by localised ductile deformation caused by the rotation of one FFT part, and pressure applied through the other FFT part. The outer tube helped with the gripping and also participated in the formation of the weld. The friction pressure was 25 kPa, while the forge pressure was 35 kPa. The rotation of the

specimens was 1800 rpm, and the length of the offset was set to 7 mm each side. The final specimen length was mainly dependent on the applied pressure.

Results and discussion

The friction welding of the FFTs was successful, creating a strong bond between foam-filled structures (Figure 3.). The impression of the clamping mechanism is seen on both sides, which can be reduced or even eliminated by altering the parameters or heat-treating the FFTs to increase the hardness of the outer tubes. The total length has been reduced to 198 mm, corresponding to the total upset length.

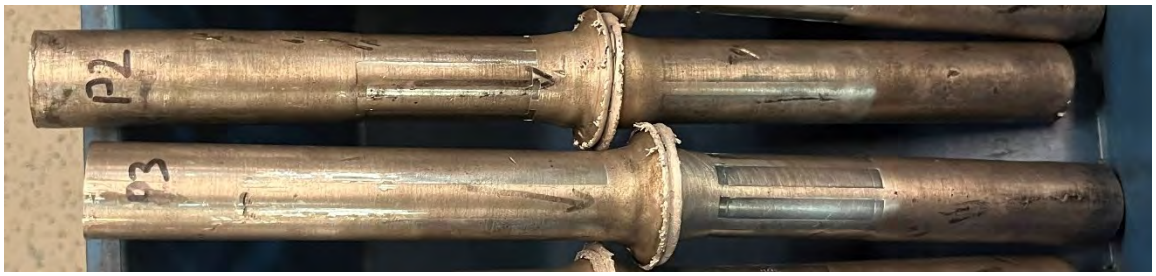

Fig. 3 Friction welded FFT.

The welded FFTs were evaluated via computed tomography before machining the welded region to the original diameter. The results shown that the open cell contact part deformed and a cohesive bond was created. Further investigations will be conducted to evaluate the microstructural changes in the material, as well as precipitation hardening heat-treatment will be used to increase the hardness and the strength of the tube material. Furthermore, the mechanical testing of the joint will be conducted, and the welding parameters will be optimized.

Conclusion

The authors have successfully joined hybrid composite metal foam-filled tubes with friction welding which is a forward-looking aspect within the widespread application of metal foams as structural elements and energy absorbing materials.

Acknowledgements

The authors thank András Kulcsár from Harlo Ltd. for the opportunity to friction weld such novel materials. A.K. was supported by the by the EKÖP-24-4-II-BME-20 University Researcher Scholarship Program of the Ministry for Culture and Innovation from the source of the National Research, Development and Innovation Fund. This work was partially supported by the Hungarian Scientific Research Fund under Grant agreement OTKA FK_21 138505 and partialy supported by the Visegrad grants from the International Visegrad Fund (project no. 22310096).

References

[1]F. García-Moreno, “Commercial Applications of Metal Foams: Their Properties and Production,” *Materials (Basel).*, vol. 9, no. 2, p. 85, Jan. 2016, doi: 10.3390/ma9020085.

[2]J. Banhart, “Metal foams - From fundamental research to applications,” in *Frontiers in the design of materials*, Taylor & Francis, 2007, pp. 279–289.

[3]A. Kemény, G. Pados, D. Károly, and I. N. Orbulov, “The Effects of Various Adhesives on Multiple Types of Quasi-Static Mechanical Properties of Rectangular and Square Aluminum Hollow Sections Filled with Composite Metal Foam Cores,” *Adv. Eng. Mater.*, vol. 26, no. 9, p. 2302066, May 2024, doi: 10.1002/adem.202302066.

[4]M. Feng, L. Ren, Z. Wang, D. Meng, S. Wang, and P. Wang, “Recent research progress of foam metals welding: a review,” *Int. J. Adv. Manuf. Technol.*, vol. 127, no. 7–8, pp. 3135–3156, Aug. 2023, doi: 10.1007/s00170-023-11709-2.

[5]A. Rabiei, J. Cance, and Z. Chacko, “A Study on Welding of Porous Metals and Metallic Foams,” *Adv. Eng. Mater.*, vol. 26, no. 4, p. 2301430, 2024, doi: 10.1002/adem.202301430.

[6]A. Kemény, B. Leveles, D. B. Kincses, and D. Károly, “Manufacturing and Investigation of In Situ and Ex Situ Produced Aluminum Matrix Foam-Filled Tubes,” *Adv. Eng. Mater.*, vol. 24, no. 1, p. 2100365, Jan. 2022, doi: 10.1002/adem.202100365.

[7]G. Pados, A. Kemény, B. Szovák, D. Károly, and I. N. Orbulov, “Fabrication of In-situ Syntactic Aluminium Foam-Filled Steel Tubes,” *Acta Mater. Transylvanica*, vol. 6, no. 1, pp. 38–41, 2023, doi: 10.33924/amt-2023-01-07.

MOF-74 Frameworks for Energy Storage in Li-S Batteries

N. Király[a]*, D. Capková[b], A. Straková-Fedorková[c], M. Almáši[a]

[a] Department of Inorganic Chemistry, Faculty of Sciences, Pavol Jozef Šafárik University in Košice, Moyzesova 11, 041 54, Košice, Slovak Republic
[b] Department of Chemical Sciences, Bernal Institute, University of Limerick, V94 T9PX Limerick, Ireland
[c] Department of Physical Chemistry, Faculty of Sciences, Pavol Jozef Šafárik University in Košice, Moyzesova 11, 041 54, Košice, Slovak Republic
*nikolas.kiraly@upjs.sk

Porous coordination polymers, specifically metal-organic frameworks (MOFs), have emerged as highly efficient catalysts for Li-S batteries due to their large surface area, customizable pore size, and distinctive porous structure. MOFs are hybrid materials composed of metal ions or clusters linked by organic molecules, forming strong and stable frameworks. These unique structures make MOFs versatile, with applications spanning various research fields, including drug delivery, gas adsorption and separation, heterogeneous catalysis, and ion exchange. They have been extensively studied as additives in cathode materials for Li-S batteries, with the zeolitic imidazole framework (ZIF) being one of the most commonly employed MOFs in this application [1-3]. Among MOFs, MOF-74, also known as CPO-27 (coordination polymer of Oslo), stands out as one of the most promising due to its high density of open metal sites within its one-dimensional hexagonal channels along the *c*-axis. It also boasts high porosity, substantial surface area, and exceptional CO_2 adsorption capabilities under typical atmospheric conditions, outperforming many other MOFs. MOF-74(M) (where M represents a transition metals) features an isostructural framework with the formula $\{[M_2(DOBDC)(H_2O)_2]\cdot 8H_2O\}_n$, where DOBDC stands for 2,5-dioxido-1,4-benzenedicarboxylate. In this structure, metal atoms act as vertices that connect organic linkers to form hexagonal arrangements. When heated under vacuum, M-MOF-74 reveals Lewis acidic sites (coordinately unsaturated metal sites) that enable strong binding of molecules such as CO_2, CH_4, and S_x, which act as Lewis bases [4, 5].

MOF-74(Ni), MOF-74(Fe), and MOF-74(Mg) were synthesized, characterized, and evaluated as functional hosts for sulfur in Li-S batteries. The study explored the impact of different metal ions in the MOF structures on the performance of Li-S battery cells. Among these, S/MOF-74(Ni) demonstrated enhanced electrochemical activity, promoting redox kinetics of lithium polysulfides and exhibiting strong adsorption capabilities. The porous architecture of MOF-74(Ni) effectively confines and encapsulates sulfur, accommodates volumetric expansion during cycling, and prevents the diffusion of lithium polysulfides, resulting in an extended cycle life. The S/MOF-74(Ni) cathode delivered a capacity of 614 mAh g^{-1} at 0.2 C and 315 mAh g^{-1} at 2 C, while maintaining exceptional cycling stability over 200 cycles at 0.5 C, with a capacity decay of just 0.001% per cycle. This outstanding electrochemical performance is attributed to the unique porous structure of MOF-74 and the high catalytic properties of Ni. On the other hand, the S/MOF-74(Mg) cathode displayed respectable electrochemical performance, with a capacity of 526 mAh g^{-1} at 0.2 C. However, its stability at higher currents was lower, with a capacity of 280 mAh g^{-1}, and cycling stability over 200 cycles at 0.5 C showing a capacity decay of 0.110%. The S/MOF-74(Fe) electrode exhibited the poorest long-term cycling stability at 0.5 C among the MOF-74 materials tested. The investigation of different metal ions in the MOF structures and their effects on Li-S battery performance offers valuable insights for selecting appropriate metal ions in MOF materials.

Acknowledgements

This work was supported by APVV SK-CZ-RD-21-0068, APVV-23-0097, VVGS-2023-2724 and funded by the EU NextGenerationEU through the Recovery and Resilience Plan for Slovakia under the project No. 09I03-03-V05-00008.

References

[1] J.-M. Huang *et al.*, "MOF-based materials for electrochemical reduction of carbon dioxide," *Coordination Chemistry Reviews*, vol. 494, p. 215333, 2023. doi:10.1016/j.ccr.2023.215333

[2] J. L. Obeso *et al.*, "The role of dynamic metal-ligand bonds in metal-organic framework chemistry," *Coordination Chemistry Reviews*, vol. 496, p. 215403, 2023. doi:10.1016/j.ccr.2023.215403

[3] W. Li *et al.*, "Rational design and general synthesis of multimetallic metal–organic framework nano-octahedra for enhanced Li–S Battery," *Advanced Materials*, vol. 33, no. 45, 2021. doi:10.1002/adma.202105163

[4] I. Choi *et al.*, "Facile synthesis of M-MOF-74 (M=Co, Ni, Zn) and its application as an electrocatalyst for electrochemical CO_2 conversion and H_2 production," *Journal of Electrochemical Science and Technology*, vol. 8, no. 1, pp. 61–68, 2017. doi:10.5229/jecst.2017.8.1.61

[5] H. Wu, W. Zhou, and T. Yildirim, "High-capacity methane storage in metal−organic frameworks M_2(dhtp): The important role of open metal sites," *Journal of the American Chemical Society*, vol. 131, no. 13, pp. 4995–5000, 2009. doi:10.1021/ja900258t

8th International Conference on Novel Materials Fundamentals and Applications
High Tatras, 13.-16.10.2024

Textural Characteristics of Biochar

M. Lhotka[a]*

[a] Department of Inorganic Technology, Faculty of Chemical Technology, University of Chemistry and Technology, Prague, Technická 5, 166 28, Prague 6, Czech Republic
*miloslav.lhotka@vscht.cz

Biochar is a high porous, fine, carbon rich material produced by pyrolysis from different feedstock material of organic origin. The difference between biochar and char is in their subsequent use: the biochar is designed for soil application and char for combustion [1]. Plant biomass can be transferred into biochar via pyrolysis and can be further used as a soil sorbent agent. The aim of this study was to generalize the influence of agriculture residues and temperature of pyrolysis on biochar yield, surface properties and pore composition. The plant biomass for pyrolysis was harvested in the relatively small area close to Příbram region (Czech Republic, 60km from Prague). Plants from the Saliceae family were chosen as the bark wood biomass. Then the soft deciduous bark-free poplar wood, with low content of risk elements, purchased from J.Rettenmaier&Söhne GmbH, was used to determine the influence of the bark presence and low risk element content on the properties of final biochar. The crops originated from a generally designed crop rotation agriculture system were used. In the first year, whole above ground biomass of maize was harvested and pyrolyzed, the second year, winter wheat in full maturity was used, and therefore, the grains and straw were pyrolyzed separately. Meadow grass was harvested in autumn as second growth harvest near the plantation growing the wood biomass. Biomass of herbaceous and wood plants was treated by slow pyrolysis at 5 temperatures (400 – 600°C) to prepare biochar. All types of feedstock materials provided biochar yield ranged from 30-10% (w/w) of entry dry biomass, when higher yields were obtained at herbaceous materials and at lower temperature of pyrolyses. Positive linear correlation and logarithmic relationship between yield, specific surface area (respectively) and final temperature were determined [2]. The specific surface area (S_{BET} and $S_{t\text{-}plot}$), micropore analysis and distributions of volume mezopores were measured on an ASAP 2020 and 3Flex surface analysers (Micromeritics, Norcross, GA, USA) using the gas sorption technique (N_2 at 77 K). The adsorption isotherms were fitted by using the Brunauer-Emmett-Teller (BET) method for specific surface area the micropore volume by the t-plot method and the pore-size distribution by the Barrett-Joyner-Halenda (BJH) method. Skeletal density was measured on a He-pycnometry 1305 analyser (Micromeritics, Norcross, GA, USA). Mercury porosimetry measurements were made using an Autopore IV 9500 porosimeter (Micromeritics, Norcross, GA, USA). The S_{BET} generally increased logarithmically (bark-free wood excluding value of S_{BET} at 600°C: R^2=0.98 bark wood: R^2=0.98; maize: R^2=0.89; meadow grass: R^2=0.99; winter wheat straw: R^2=0.94, winter wheat grain: R^2=0.55) with temperature of pyrolysis, e.g. for bark wood values increased from 124.4 $m^2\ g^{-1}$ to 428.1 $m^2\ g^{-1}$, for maize from 4.75 – 105.05 $m^2\ g^{-1}$. The highest surface area was found in biochar from bark-free wood (511 $m^2\ g^{-1}$); the herbaceous material, provided specific surface area of 192 $m^2\ g^{-1}$ (wheat straw). Total pore volume was higher at wood biomass (0.08 – 0.296 $cm^{-3}\ g^{-1}$). Microporous structure was predominant for biochars (predicting possible sorption abilities), prepared at increasing pyrolysis temperature, the volume of micropores was more developed. Mercury porosimetry results have confirmed nitrogen adsorption results. There are no mesopores in the system; macropores can be found only in the interval of pore radius 0.2-7 μm. The SEM analysis confirmed previous determination and showed a significant macropores of the biochar, particularly the in range of radius from 2 to 10 μm. Porosity of biochar is feedstock dependent but is not affected by pyrolysis temperature, e.g. bark wood porosity is in interval 54-58% over all temperatures. Maize biochar contains less pores than bark wood biochar, volumes of mesopores and micropores are four times lower. On the other hand overall macropores volume is about 10% higher. Meadow grass biochar has similar characteristic as maize biochar, bark wood biochar has comparable properties with bark-less wood. Skeletal density was < 1 $cm^{-3}g^{-1}$, while envelope density did not exceed 1$cm^{-3}\ g^{-1}$. High mechanical resistance was observed in bark-wood biochar pellets.

References

[1] J. Lehmann, J. Joseph, "Biochar for environmental management: science and technology," Earthscan, London (2009).

[2] K. Břendová, J. Száková, M. Lhotka, T. Krulikovská, M. Punčochář, P. Tlustoš, "Biochar physicochemical parameters as a result of feed-stock material and pyrolysis temperature: predictable for the fate of biochar in soil? " *Environ Geochem Health* vol. 39, pp. 1381–1395, 2017.

8th International Conference on Novel Materials Fundamentals and Applications
High Tatras, 13.-16.10.2024

Magnetite Modification as a Booster of Antimicrobial Activity of Natural Clays

A. Maciejczyk[a]*, M. Trzaskowska[a], J. Matusiak[b], W. Franus[b], A. Przekora[a]

[a] Department of Tissue Engineering and Regenerative Medicine, Medical University of Lublin, Chodzki 1, 20- 093 Lublin, Poland
[b] Department of Construction Materials Engineering and Geoengineering, Faculty of Civil Engineering and Architecture, Lublin University of Technology, Nadbystrzycka 40, 20-618 Lublin, Poland
*aleksandramaciejczyk@umlub.pl

Introduction

Clays are mineral raw materials that occur naturally in most regions of the world. It is well known that clay has been used as a natural remedy since prehistoric times. The focus was mainly on the healing and soothing properties, but recently it has been proven that natural clays also have antibacterial properties [1]. This is a very important feature, as natural antimicrobials are needed to fight infections. The most popular applications of clay minerals are mainly cosmetics, but they are now gaining attention in tissue engineering as a matrices for stem cell growth and differentiation [2, 3].

Due to divergence in their natural composition, the antimicrobial activity of clays can be totally different. However, their general biological activity can be modulated by many parameters, such as magnetite modification. The aim of this study was to modify natural clays with magnetite to boost their antimicrobial properties.

Materials and Methods

To synthesize different magnetite-clay complexes based on kaolinite, glauconite, montmorillonite, and bentonite, the chemical co-precipitation method was used. The synthesis was carried out at room temperature in an air atmosphere. In short, to a homogeneous aqueous suspension of the chosen clay in a capped laboratory flask placed on a magnetic stirrer the specific volume of degassed aqueous NaOH solution added to adjust the pH to 10-10.5. Then iron(II) and iron(III) chloride salts dissolved in degassed water (in a ratio of 2:3) was added quickly to the alkaline clay suspension. The resulting black colloid was mixed for 45 minutes and then the solid residue was magnetically separated and washed with water, ethanol, and acetone to remove any residual synthesis impurities. The obtained powder was dried at 70°C for 24 hours.

Then, X-ray diffraction (XRD) was carried out to confirm the crystalline structure of the materials. Determination of the size of the primary magnetite nanoparticles was carried out using transmission electron microscopy (TEM) combined with energy dispersive spectroscopy (EDS).

Synthesized different types of Fe_3O_4-clay complexes were subjected to microbiological tests on *E. coli*, *S. aureus*, *P. aeruginosa*, and *C. albicans* and cytotoxicity test *in vitro* towards normal human skin fibroblasts (BJ cell line, ATCC) according to ISO 10993-5 standard dedicated for medical devices. Fibroblast viability was assessed using MTT test (according to ISO 10993-5, cell viability must exceed 70% to consider biomaterial as non-cytotoxic).

Results and Discussion

TEM/EDS analysis revealed a high quantity of iron and oxygen in the synthesized Fe_3O_4, indicating high product quality (Fig. 1a). Additionally, the particles were under 20 nm in size, which is important for catalytic applications. X-ray diffraction confirmed the formation of Fe_3O_4-clay complex materials (Fig 1b).

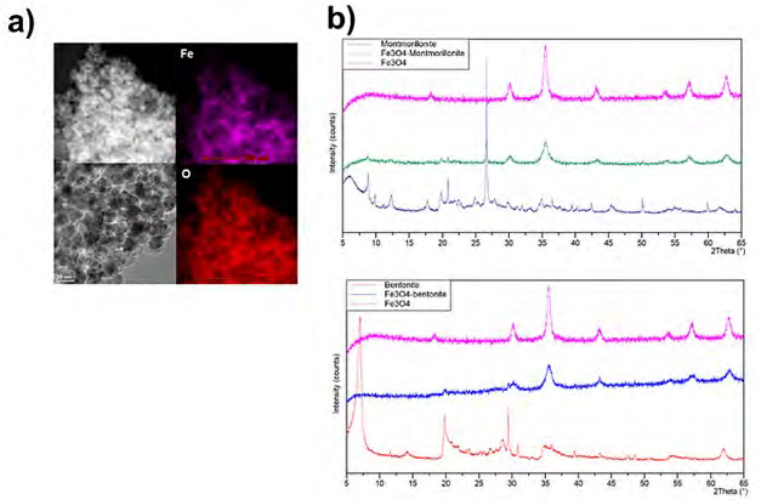

Fig. 1 (a) TEM-EDS of synthesized Fe_3O_4 nanoparticles; (b) Exemplary XRD diffractograms of Fe_3O_4-montmorillonite and Fe_3O_4-bentonite.

The experiments clearly revealed that modification of natural clays with magnetite significantly boosted their antimicrobial properties without meaningful negative effect on viability of human skin cells (Table 1). Fe_3O_4-montmorillonite and Fe_3O_4-bentonite showed the strongest antimicrobial activity. It should be noted that although bentonite is a clay consisting mostly of montmorillonite, antimicrobial activity of the unmodified bentonite was significantly higher compared to unmodified montmorillonite. This may be due to the fact that bentonite contains other minerals in addition to montmorillonite, which show an additional positive synergistic influence on antimicrobial activity.

Tab. 1 Preliminary biological tests' results: antimicrobial activity and cytotoxicity against human skin fibroblasts of the clays and magnetite-clay complexes.

Tested clay mineral	MIC (minimum inhibitory concentration) [mg/mL]				Viability [%] of human skin fibroblasts
	E. coli	*P. aeruginosa*	*S. aureus*	*C. albicans*	
kaolinite	ND	ND	5	5	101
Fe_3O_4- kaolinite	10	10	5	5	93
glauconite	ND	ND	2.5	20	105
Fe_3O_4-glauconite	20	20	1.25	5	96
montmorillonite	ND	ND	10	20	76
Fe_3O_4- montmorillonite	**0.156**	**0.156**	**0.156**	**1.25**	**82**
bentonite	10	20	0.313	5	91
Fe_3O_4-bentonite	**5**	**5**	**2.5**	**2.5**	**84**

ND – not determined (no antimicrobial activity detected)

Conclusions

Magnetite modification clearly enhances the antimicrobial activity of the clays we tested. Moreover, visibly enhances the antibacterial activity against gram negative bacteria, while natural clays in most cases have no antibacterial activity detected against them. Preliminary results of *in vitro* studies reveal that modified clays do not have negative effect on viability of human skin cells. To confirm biomedical potential of analized clays it is necessary to conduct further research to assess their physico-chemical and mechanical properties.

Acknowledgements

Research was financed by The the Ministry of Higher Education and Science in Poland within the statutory activity of the Medical University of Lublin (DS 630 project) and partialy supported by the Visegrad grants from the International Visegrad Fund (project no. 22310096).

References

[1] N.N. Azmi, N.A. Mahyudin, W.H. Wan Omar, N.K. Mahmud Ab Rashid, C.F. Ishak, A.H. Abdullah, G.J. Sharples, "Antibacterial Activity of Clay Soils against Food-Borne Salmonella typhimurium and Staphylococcus aureus," *Molecules* vol. 27, pp. 170, 2020, https://doi.org/10.3390/molecules27010170

[2] G. Sandri, M.C. Bonefori, S. Rossi, F. Ferrari, C. Aquzzi, C. Viseras, C. A. R. L. A. Caramella, "Clay minerals for tissue regeneration, repair, and engineering, Wound healing biomaterials," pp. 385-402, 2016, https://doi.org/10.1016/B978-1-78242-456-7.00019-2

[3] L.B. Williams, D.W. Metge, D.D. Eberl, R.W. Harvey, A.G. Turner, P. Prapaipong, A.T. Poret-Peterson, "What makes a natural clay antibacterial?," *Environmental science & technology*, vol. 45(8), pp. 3768-3773, 2011, doi: 10.1021/es1040688

Surface Modification of Nickel for Biosensor Applications

F. Märzweiler[a]*, J. Huber[a], G. Fafilek[a]

[a] TU Wien, Institute of Chemical Technologies and Analytics, EC, Vienna, Getreidemarkt 9, 1060 Vienna, Austria
*florian.maerzweiler@tuwien.ac.at

From the field of catalysis, it is known that certain surface orientations can favor the kinetics of a desired reaction and enhance its rate. Consequently, the more of such favorable surfaces are present, the more the reaction rate can be increased. Examples for such catalytic surfaces are nanocubes [1] or petals [2].

In this work, we present the modification of the metallic surface of nickel electrodes to increase the amount of such desired surface orientations using cyclic voltammetry. The modification was tested for various electrolytes, potential ranges and scan rates. In order to test the catalytic properties of the yielded modifications, the cyclic voltammogram of glucose in the negative potential range will be observed.

Employing surface modified nickel as a sensing element in biosensors would, in this case, offer a possibility for non-enzymatic glucose detection [3]. Furthermore, measurements in a negative potential range could ensure stability of the modified nickel surfaces, which are free from overlap with other oxidation peaks.

References

[1] F. Roberts, K. Kuhl and A. Nilsson, “High Selectivity for Ethylene from Carbon Dioxide Reduction over Copper Nanocube Electrocatalysis”, *Angew. Chem*, vol. 54, no. 17, pp. 5179-5282, Apr. 2015, doi: 10.1002/anie.201412214
[2] G. Tong, F. Liu, W. Wu, J. Shen, X. Hu and Y. Liang, “Polymorphous a- and b-Ni(OH)2 complex architectures: morphological and phasal evolution mechanisms and enhanced catalytic activity as non-enzymatic glucose sensors”, *CrystEngComm*, vol. 14, no.18, pp. 5963-5973, Jun. 2012, doi: 10.1039/c2ce25622c
[3] F. Franceschini, I. Taurino, “Nickel-based catalysts for non-enzymatic electrochemical sensing of glucose: A review”, *Physics in Medicine*, vol. 14, Sep. 2022, doi: 10.1016/j.phmed.2022.100054

The Influence of Hydroxyapatite Coating on Degradation Rate of Zinc

I. Mojžišová[a]*, R. Oriňaková[a]

[a] Department of Physical Chemistry, Faculty of Science, P. J. Šafárik University in Košice, Moyzesova 11, 041 54, Košice
*ivana.mojzisova@student.upjs.sk

Introduction

Numerous fractures and bone injuries require only temporary support for their regeneration, which can replace the function of natural bone for a limited duration. Currently, various materials are being intensively studied to prepare a biodegradable material capable of completely dissolving within the body without eliciting adverse reactions. In recent years, significant attention has been given to zinc and its alloys due to its important role in the human body, especially in bone metabolism [1]. In addition, zinc with an electrode potential value of – 0.762 V has the most suitable degradation rate among other metals studied for these purposes, such as iron and magnesium [2].

Biocompatibility and degradation of zinc-based biodegradable materials can be improved and modified by surface modifications. Appropriate surface treatment can prevent implant failure and increase its durability. It also significantly impacts the host's immune response to the implant and the course of the healing and osteogenesis process. Additionally, it can reduce the risk of infection caused by bacterial adherence to the implant surface [3, 4]. One of the frequently used substances for surface treatment of metal materials is synthetic hydroxyapatite. It is very close to the bone apatite structure, thereby improving the biological properties of implants [5].

Experiment

In this work, the degradation rate of zinc materials modified with 2 types of coatings was electrochemically studied. The zinc surface was modified by bare hydroxyapatite (Zn-HAp) and hydroxyapatite doped with silver as an antibacterial component (Zn-HAp-Ag). Metallic zinc samples were prepared from zinc powders by the powder metallurgy method at a pressure of 545 MPa and then sintered at 350°C in an inert atmosphere for 1 hour. The ceramic coatings were deposited on the samples electrochemically using a potentiostat at a current density of 0.4 mA/cm^2 for 30 minutes at a constant temperature of 65 °C maintained by external heating. The hydroxyapatite coating was deposited from an electrolyte containing $Ca(NO_3)_2 \cdot 4H_2O$ and $NH_4H_2PO_4$, while in the case of the coating doped with silver, $AgNO_3$ was added to the electrolyte. Coated samples were immersed in a 1 mol/dm^3 NaOH solution for 2 hours at a temperature of 65 °C, washed in distilled water, and dried for another 2 hours at a 80 °C.

The dynamic degradation test was performed by potentiodynamic polarization in Hanks' solution simulating body fluids at a temperature of 37 °C. Before corrosion tests, the open circuit potential (OCP) of each sample was measured to stabilize the system. Corrosion of samples was examined in a three-electrode circuit and values of corrosion potential (E_{corr}), corrosion current density (j_{corr}), and corrosion rate (CR) were determined by Tafel extrapolation.

Results and discussion

During the process of system stabilisation, the OCP potential decreased and stabilised at a certain value for all samples. The samples coated with ceramic coatings (Zn-HAp, Zn-HAp-Ag) achieved stabilisation at more negative OCP potential values in comparison to the uncoated zinc. The corrosion potential values determined by Tafel extrapolation from potentiodynamic polarization curves were also observed at more negative potential values in the case of Zn-HAp and Zn-HAp-Ag (Fig. 9). This indicates an increased susceptibility of coated samples to corrosion.

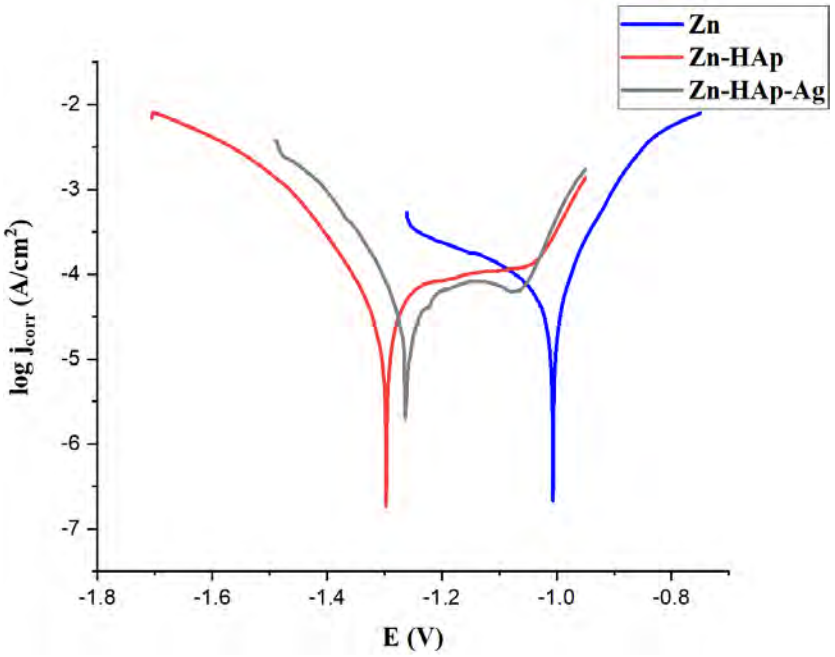

Fig. 9 Potentiodynamic polarization curves of Zn, Zn-Hap and Zn-Hap-Ag samples degradation.

The corrosion rates were calculated from the corrosion current density (j_{corr}), which represents the determining parameter for the corrosion rate. The Zn-HAp-Ag samples corroded the fastest and the uncoated Zn samples the slowest (Tab. 1). However, there was no significant difference observed between the corrosion rate values of coated and uncoated zinc.

Tab. 1 Values of E_{corr}, j_{corr}, corrosion rate and polarization resistance of Zn, Zn-HAp and Zn-HAp-Ag samples.

	Sample		
	Zn	Zn-HAp	Zn-HAp-Ag
E_{corr} (V)	-1.006	-1.297	-1.265
J_{corr} (V)	$2.91 \cdot 10^{-5}$	$2.94 \cdot 10^{-5}$	$3.38 \cdot 10^{-5}$
Corrosion rate (mm/year)	0.44	0.48	0.56
Polarization resistance (Ω)	569.88	914.08	777.8

The shift of the corrosion potential towards more negative values and the higher corrosion rate in the coated samples can be attributed to the presence of numerous pores within the coating observed by optical microscopy (Fig. 10). The pores formation was probably caused by the release of gaseous H_2, which is formed during the electrochemical deposition process. The uncoated regions of the zinc substrate were exposed to direct contact with the electrolyte, leading to the phenomenon of localized pitting corrosion. In this process the exposed area acts as the anode and the surrounding areas act as the cathode. The flow of electrons from the anodic site to the cathodic site results in the oxidative dissolution of the zinc substrate and leads to the acceleration of corrosion in the coated samples.

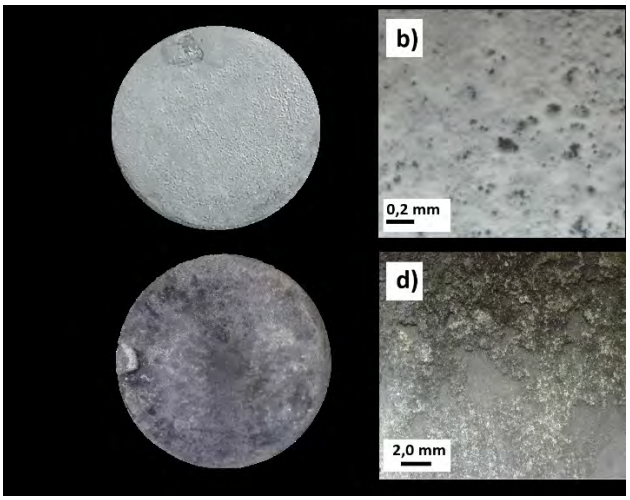

Fig. 10 Optical microscopy images of coated Zn-HAp (a,b) and Zn-HAp-Ag (c,d) samples.

Acknowledgements

This work was supported by the Slovak Research and Development Agency under the project APVV-20-0278 and Visegrad grants from the International Visegrad Fund (project no. 22310096).

References

[1] A. R. Khan, N. S. Grewal, C. Zhou, K. Yuan, H. J. Zhang, and Z. Jun, "Recent advances in biodegradable metals for implant applications: Exploring in vivo and in vitro responses," *Results in Engineering*, vol. 20, Dec. 2023, doi: 10.1016/j.rineng.2023.101526.

[2] M. Y. KOLAWOLE, J. O. AWEDA, S. ABDULKAREEM, and S. A. BELLO, "Biodegradable zinc alloys and composites for biomedical application: an overwiev of processing routes and possible future work," *European Journal of Materials Science and Engineering*, vol. 5, no. 3, pp. 115–132, Sep. 2020, doi: 10.36868/ejmse.2020.05.03.115.

[3] V. Vishwakarma, G. S. Kaliaraj, and K. K. Amirtharaj Mosas, "Multifunctional Coatings on Implant Materials—A Systematic Review of the Current Scenario," *Coatings*, vol. 13, no. 1, Jan. 2023, doi: 10.3390/coatings13010069.

[4] A. R. Amini, J. S. Wallace, and S. P. Nukavarapu, "Short-Term and Long-Term Effects of Orthopedic Biodegradable Implants," *J Long Term Eff Med Implants*, vol. 21, no. 2, pp. 93–122, 2011.

[5] S. Wei, J. X. Ma, L. Xu, X. S. Gu, and X. L. Ma, "Biodegradable materials for bone defect repair," *Mil Med Res*, vol. 7, no. 1, Dec. 2020, doi: 10.1186/s40779-020-00280-6.

Advanced Composite Cathode Material for Enhanced Stability and Capacity Retention

V. Niščáková[a]*, A. Straková Fedorková[a], A. Gubóová[b]

[a] Pavol Jozef Safarik University of Kosice, Department of Physical chemistry, Srobarova 2, 040 01, Kosice
[b] Institute of Materials Research, Slovak Academy of Sciences, Watsonova 47, 040 01, Kosice
*veronika.niscakova@upjs.sk

Since the Industrial Revolution, energy has been a pivotal catalyst for societal advancement, propelling development across diverse sectors. Secondary batteries, renowned for their efficiency, environmental friendliness, and safety, have found widespread application in domains ranging from consumer electronics to medical devices. While lithium-ion batteries (LIBs) have dominated the market, their high cost and theoretical capacity limitations hinder their suitability for applications demanding exceptional energy density. To address this pressing need, energy storage systems capable of delivering elevated energy densities are urgently sought. Lithium-sulfur (Li-S) batteries, widely considered as a potential successor to LIBs, have garnered significant attention from both academic and industrial communities [1]. Li-S batteries offer a theoretical capacity (1675 mAh g^{-1}) significantly exceeding that of conventional LIBs and other emerging battery technologies. Sulfur's abundance and environmental friendliness make it a promising candidate for large-scale energy storage. However, practical applications are hindered by challenges such as sulfur's low electrical conductivity, volume expansion during cycling, and the formation of unstable solid electrolyte interphase (SEI) layers on the lithium anode. Additionally, the dissolution and migration of polysulfides within the battery can lead to capacity fading and reduced performance [2]. To realize the commercial potential of Li-S batteries, it is essential to address their inherent challenges. A key focus of research has been on optimizing the cathode, where sulfur is often incorporated into carbon-based materials. These materials are designed to improve cathode performance by addressing key limitations such as the polysulfide shuttle effect and sulfur’s low electrical conductivity, thereby enhancing the overall efficiency and stability of the Li-S battery system [3].

Research efforts have been increasingly directed towards the conversion of biomass into functional carbon materials for energy storage applications. The selection of appropriate biomass precursors is paramount for the fabrication of biomass-based electrode materials, and an increasing number of agricultural wastes have been utilized for this purpose [4]. Biomass precursors possess several distinct benefits compared to other carbon sources. Their unique structures and morphologies, shaped by millennia of evolution, often result in hierarchical channel structures that are ideal for accommodating and adsorbing sulfur, mitigating cathode volume expansion. Additionally, the vast annual production of biomass from various industries ensures a low-cost supply of biomass-derived carbons, significantly reducing the commercial production cost of lithium-sulfur batteries [5].

A carbon-based conductive additive, derived from the carbonization of corn cobs in a tubular furnace, was incorporated into the cathode material of a Li-S battery. This novel additive was employed in conjunction with the conventionally used Super P carbon. The novel, low-cost, and sustainable carbon additive underwent thorough structural and electrochemical characterization.

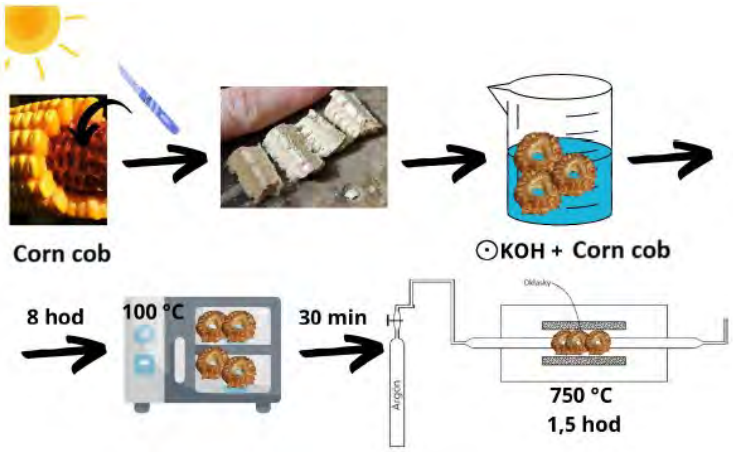

Fig. 11 Preparation of Carbon-Based Conductive Additive from Corn Cob Biomass.

Scanning electron microscopy was employed to investigate the surface morphology and structural characteristics of the fabricated electrode. Electrochemical characterization of the prepared electrodes was conducted using cyclic voltammetry and galvanostatic cycling techniques in three-electrode testing El-cell. Corn cob-derived carbon-modified sulfur electrodes were utilized as working electrodes (WE), while lithium metal served as both the counter electrode (CE) and reference electrode (RE). Both cyclic voltammetry and galvanostatic cycling measurements were performed within a potential window of 1.8 V to 2.8 V. Cyclic voltammetry analysis revealed two distinct reduction peaks, suggesting a multi-step reaction between sulfur and lithium ions. The first reduction peak, observed at 2.35 V, is indicative of elemental sulfur (S_8) being reduced to polysulfides. A second reduction peak at 2 V corresponds to the subsequent reduction of polysulfides to Li_2S_2 and Li_2S. Furthermore, two oxidation peaks were observed, attributed to the reverse reaction of polysulfides to elemental sulfur. These findings are in agreement with the established mechanism of lithium-sulfur batteries.

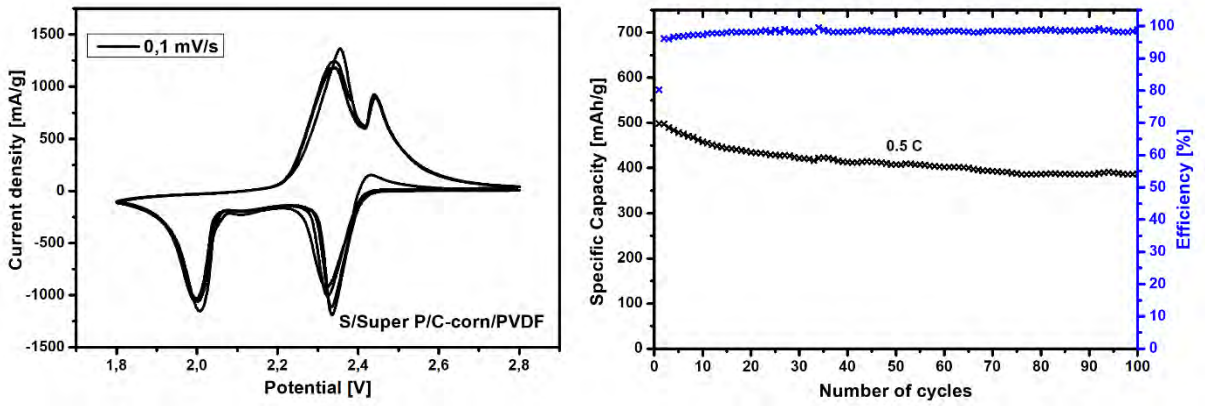

Fig. 12 Cyclic voltammogram of electrode at 0.1 mV/s and the long-term cycling performance at 0.5.

The initial capacity of electrode at 0.1 C and the real specific capacity was around 740 mAh g^{-1}, which represents 44 % of theoretical specific capacity of sulfur. To assess long-term stability, 100 cycles were conducted at a current rate of 0.5 C. The electrode demonstrated an initial discharge capacity of approximately 499 mAh g^{-1}, with a capacity

retention of approximately 387 mAh g^{-1} after 100 cycles. The electrode exhibited a coulombic efficiency of 98% and demonstrated exceptional stability over the entire cycling process. The observed stability can be attributed to the unique properties of the carbon derived from corn cob, which resulted in a relatively pure carbon material. Carbon plays a crucial role in lithium-sulfur batteries, primarily enhancing the electrical conductivity of sulfur, which is essential for efficient energy storage. The carbon obtained from corn cob offers both economic and environmental benefits, as it represents a valuable utilization of biomass waste.

The results presented in this study demonstrate the potential of corn cob-derived carbon as a promising conductive additive for lithium-sulfur batteries. The use of corn cob-derived carbon offers a sustainable and cost-effective approach for the development of high-performance lithium-sulfur batteries.

Acknowledgements

This work was supported by the projects APVV-20-0138 and APVV-20-0111, by the VEGA project No. 1/0095/21 and KEGA project 002UPJS-4/2024 and by IPCEI_IE_FLOW_BESS_012021.

References

[1]Y. Li, J. G. Shapter, H. Cheng, G. Xu, and G. Gao, “Recent progress in sulfur cathodes for application to lithium–sulfur batteries,” *Particuology*, vol. 58, pp. 1–15, Oct. 2021, doi: 10.1016/j.partic.2021.01.008.

[2]J. Li *et al.*, “Engineering Strategies for Suppressing the Shuttle Effect in Lithium–Sulfur Batteries,” Dec. 01, 2024, *Springer Science and Business Media B.V.* doi: 10.1007/s40820-023-01223-1.

[3]V. Niščáková *et al.*, “Novel Cu(II)-based metal–organic framework STAM-1 as a sulfur host for Li–S batteries,” *Sci Rep*, vol. 14, no. 1, Dec. 2024, doi: 10.1038/s41598-024-59600-8.

[4]K. Xie *et al.*, “Electrochemical Performance of Corn Waste Derived Carbon Electrodes Based on the Intrinsic Biomass Properties,” *Materials*, vol. 16, no. 14, Jul. 2023, doi: 10.3390/ma16145022.

[5]C. Ma *et al.*, “Green Production of Biomass-Derived Carbon Materials for High-Performance Lithium–Sulfur Batteries,” Jun. 01, 2023, *MDPI*. doi: 10.3390/nano13111768.

Use of Artificial Intelligence in Electricity Systems

A. Oriňak[a]*

[a] Department of Commercial Law and Business Law, Faculty of Law, P.J. Safarik University,
Kováčska 26, 040 75 Košice, Slovakia
*andrej.orinak@student.upjs.sk

To limit climate change and achieve net-zero emission targets, a transition to sustainable, efficient, competitive, and secure energy system is currently underway [1]. Thanks to widespread support for low-carbon energy policies and improved cost competitiveness, renewable energy, particularly wind and solar, has seen unprecedented growth over the past decade [2].

The second digital revolution and the need to quickly process large amounts of data lead to the use of artificial intelligence (AI) in electrical systems to facilitate and accelerate the energy transition. The artificial intelligence is defined as algorithms that mimic the cognitive functions of the human mind to make decisions without being supervised [3]. The data-driven AI techniques allow to address different issues in electricity systems associated with the increasing energy supply from dynamic renewable sources, such as the integration of renewable and more volatile energy sources, the increased use of the network due to the growing electrification, and a lack of network capacity [4]. AI adoption promises to streamline asset maintenance processes, increase transparency in pricing, maintain the affordability of electricity, efficiently manage intermittent renewables and balance supply and demand pressures on the grid. However, these technologies also raise certain concerns, as they may reduce transparency, violate privacy or lead to discrimination.

Along with the energy transformation, the concept of energy justice emerged as a new crosscutting social science and humanities research agenda that seeks to apply principles of justice to energy policy, energy production and systems, energy consumption, energy activism, energy security and climate change [5]. Although research in this area is constantly expanding, there are still many unanswered questions that arise in the use of AI technologies in the management of digitized and data-based electrical systems.

The aim of this paper is to study how the use of AI can affect energy justice. The analysis is based on a review of literature on AI technologies for management of electrical systems and the academic literature on energy justice.

The use of AI can have significant implications for energy justice, which is concerned with the fair distribution of the benefits and burdens of energy systems across society. AI's impact can either enhance or hinder energy justice, depending on how it is applied. Table 1 summarizes some of the key manners in which AI can impact energy justice.

Tab. 1 Impact of AI on energy justice.

Issue	Positive impact	Negative impact	Ref.
Energy access and affordability	AI can help optimize energy systems, improving efficiency, reducing costs, and promoting the use of renewable energy. By enhancing the operation of power grids and integrating decentralized energy sources like solar panels or wind turbines, AI can make energy more accessible and affordable, particularly for marginalized communities. AI-driven predictive maintenance can also reduce outages and lower operational costs.	If AI technologies are costly or implemented in a way that favors wealthy regions, they could increase inequality by concentrating energy access in wealthier communities while leaving low-income or rural areas behind. AI systems can also reinforce existing economic disparities by directing energy savings and benefits primarily to those who can afford new technologies.	[4-14]
Environmental Sustainability	AI can support the transition to renewable energy, crucial for achieving energy justice by reducing dependence on polluting energy sources that disproportionately harm vulnerable communities. AI can improve the efficiency of renewable energy integration into grids, optimize energy storage, and forecast demand more accurately, reducing waste and lowering emissions.	The environmental impact of AI itself is a concern. AI systems, especially those using energy-intensive machine learning models, require substantial computing power, which can lead to higher energy consumption if not properly managed. If this energy comes from non-renewable sources, it could exacerbate environmental injustice, particularly in areas already suffering from pollution or resource depletion.	
Decision-Making and Governance	AI can enable more transparent and data-driven decision-making in energy policy, potentially leading to more equitable outcomes. AI tools can help governments and organizations identify underserved communities and better allocate resources to improve energy infrastructure in these areas.	There is a risk of AI being used to centralize control over energy systems in the hands of a few powerful entities (e.g., large corporations or governments), which could marginalize local communities and reduce democratic participation in energy decision-making. AI algorithms could also perpetuate biases if they rely on flawed data, leading to unjust outcomes, such as energy price increases for already vulnerable groups.	
Energy Workforce and Jobs	AI can create new opportunities in the energy sector, especially in green tech, smart grids, and renewable energy fields. As AI facilitates the transition to more sustainable energy systems, it can generate jobs that help uplift communities affected by energy poverty or the decline of fossil fuel industries.	The automation of energy-related jobs due to AI could disproportionately affect workers in traditional energy sectors, such as coal or gas. These job losses could deepen economic inequality, particularly in regions reliant on fossil fuel industries, without adequate support for retraining or transitioning to new roles in the renewable energy economy.	
Energy Security and Resilience	AI can improve the resilience of energy systems by predicting and responding to demand fluctuations,	AI-driven energy systems, if not equitably distributed, could create disparities in who benefits from	

	optimizing grid stability, and preparing for disruptions from natural disasters or cyberattacks. This is especially important for vulnerable communities that often suffer more from energy disruptions.	improved energy resilience. Wealthier regions may have better AI-enabled systems in place, while poorer or rural areas could experience more frequent outages or vulnerabilities in the face of climate-related or cyber threats.	
Bias and Discrimination in Energy Distribution	-	AI algorithms can unintentionally embed biases in energy distribution decisions, particularly if they are trained on historical data that reflect existing inequalities. For example, AI may prioritize energy efficiency investments in wealthier areas, where customers are more likely to have smart meters or advanced technology, leaving low-income communities with outdated infrastructure.	

In summary, AI has the potential to promote energy justice by improving energy access, affordability, sustainability, and resilience. However, if not carefully managed and designed with equity in mind, it could exacerbate existing inequalities in the energy sector. Ethical considerations, inclusive policy frameworks, and proactive engagement with marginalized communities are essential to ensure that AI supports a just energy transition.

References

[1] S. Potrc, L. Cucek, M. Martin, Z. Kravanja, "Sustainable renewable energy supply networks optimization – the gradual transition to a renewable energy system within the European Union by 2050," *Renew. Sustain. Energy Rev.*, vol. 146, Article 111186, 2021, doi: 10.1016/j.rser.2021.111186.

[2] Y. Yang, S. Xia, P. Huang, J. Qian, "Energy transition: Connotations, mechanisms and effects," *Energy Strategy Rev.*, Vol. 52, Article 101320, 2024, doi: 10.1016/j.esr.2024.101320.

[3] T. Yigitcanlar, R Mehmood, J. M. Corchado, "Green Artificial Intelligence: Towards an Efficient, Sustainable and Equitable Technology for Smart Cities and Futures," *Sustainability,* Vol. 13, Article 8952, 2021, doi: 10.3390/su13168952.

[4] M. Noorman, B. Espinosa Apráez, S. Lavrijssen, "AI and Energy Justice," *Energies,* Vol. 16, Article 2110, 2023, doi: 10.3390/en16052110.

[5] K. Jenkins, D. McCauley, R. Heffron, H. Stephan, R. Rehner, "Energy justice: A conceptual review," *Energy Res. Soc. Sci.,* Vol. 11, pp. 174-182,2016, doi: 10.1016/j.erss.2015.10.004.

[6] J. Lee, J. Byrne, "Expanding the Conceptual and Analytical Basis of Energy Justice: Beyond the Three-Tenet Framework," *Front. Energy Res.*, Vol. 7, p. 99, (2019), doi: 10.3389/fenrg.2019.00099.

[7] R. J. Heffron, L. De Fontenelle, C. Basil, I. Del Guayo Castiella, S. Droubi, M. Hazrati, H. I. Hussein, D. Kraal, D. McCauley, A. Phillips, E. Santoire, X. Arnauld de Sartre, "Pathways of scholarship for energy justice and the social contract," *J. Energy Nat. Resources L.,* Vol. 41, no. 2, pp. 211-232, 2023, doi: 10.1080/02646811.2023.2190689.

[8] B. K. Sovacool, M. Burke, L. Baker, C. K. Kotikalapudi, H. Wlokas, "New Frontiers and Conceptual Frameworks for Energy Justice," *Energy Policy,* Vol. 105, pp. 677–691, 2017, doi: 10.1016/j.enpol.2017.03.005.

[9] D. McCauley, V. Ramasar, R. J. Heffron, B. K. Sovacool, D. Mebratu, L. Mundaca, "Energy Justice in the Transition to Low Carbon Energy Systems: Exploring Key Themes in Interdisciplinary Research," *App. Energy*, Vol. 233-234, pp. 916–921, 2019, doi: 10.1016/j.apenergy.2018.10.005.

[10] C. O'Neil, "Weapons of Math Destruction: How Big Data Increases Inequality and Threatens Democracy," *J.Decision Makers*, Vol. 44, no. 2, pp. 97–98, 2019. doi: 10.1177/0256090919853933.

[11] B. K. Sovacool, M. Martiskainen, A. Hook, L. Baker, "Decarbonization and its Discontents: A Critical Energy Justice Perspective on Four low-Carbon Transitions," *Clim. Change*, Vol. 155, no. 4, pp. 581–619, 2019, doi: 10.1007/s10584-019-02521-7.

[12] R. Machlev, L. Heistrene, M. Perl, K. Y. Levy, J. Belikov, S. Mannor, Y. Levron, "Explainable Artificial Intelligence (XAI) Techniques for Energy and Power Systems: Review, Challenges and Opportunities," *Energy AI*, Vol. 9, Article 100169, 2022, doi: 10.1016/j.egyai.2022.100169.

[13] M. Lacey-Barnacle, "Proximities of Energy Justice: Contesting Community Energy and Austerity in England," *Energy Res. Soc. Sci.*, Vol. 69, Article 101713, 2020, doi: 10.1016/j.erss.2020.101713.

[14] L. Cheng, T. Yu, "A New Generation of AI: A Review and Perspective on Machine Learning Technologies Applied to Smart Energy and Electric Power Systems," *Int. J. Energy Res.*, Vol. 43, pp. 1928–1973, 2019, doi: 10.1002/er.4333.

Highly Efficient MoFeP Catalysts for the Hydrogen Evolution Reaction

R. Oriňaková[a]*, A. Gubóová[a], M. Strečková[b], M. Paračková[a]

[a] Institute of Chemistry, Faculty of Science, P.J. Safarik University, Moyzesova 11, 040 01 Kosice, Slovakia
[b] Institute of Materials Research, Slovak Academy of Sciences, Watsonova 47, 040 01 Košice, Slovakia
*renata.orinakova@upjs.sk

As we shift to a Net Zero emission landscape, hydrogen continues to gain significant traction as an enabling technology for this transition [1]. Due to the abundant sources of raw materials (e.g., electricity and water), electrochemical water splitting has advantages over coal gasification and steam-methane reformation associated with large hydrogen production. In particular, alkaline water electrolysis has received considerable attention owing to its characteristics of simple architecture and low-cost electrode materials (non-precious metal-based electrocatalysts with high performance) [2]. Despite being feasible green hydrogen production method, water splitting suffers from sluggish kinetics of its half-reactions resulting in need of efficient electrocatalyst that would adequately increase the effectiveness of hydrogen evolution reaction (HER) and oxygen evolution reaction (OER) [3]. The high energy consumption connected with these electrode processes and OER hinders the wider use of this method. Therefore, the development of highly efficient and sufficiently stable electrocatalysts for reduction of HER and OER overpotential is the key to promoting the industrialization of clean hydrogen production [4]. Currently, platinum, iridium, ruthenium, and other precious metals are still dominating electrocatalysts for HER and OER in both acidic and basic environments [5]. These noble metals, however, possess a significant disadvantage in terms of their limited availability and high cost which prevents their widespread use on industrial level [6]. Considerable research has been focusing on transition metal phosphides (TMP) as effective electrocatalysts for hydrogen evolution reaction unveiling activity comparable with noble metal catalysts [7].

In this work the highly efficient catalysts for HER, based on Mo phosphides with different stoichiometric ratio of Mo:P, namely MoP and Mo_3P were produced by sol-gel method. To further enhance their catalytic activity, Fe was introduced into MoP, creating highly active and stable bimetallic MoFeP catalyst. The samples were prepared in two sintering steps. The first step was performed in an air environment, resulting in the formation of metal phosphates. This was followed by a reduction in a hydrogen atmosphere, where phosphides were formed.

The electrochemical activity of MoP, Mo_3P and MoFeP catalysts in 1M KOH was evaluated using potentiostat PGSTAT302N, (Metrohm Autolab, Netherlands) in a three-electrode set-up with silver chloride electrode (Ag/AgCl/3M KCl) as reference, a large area platinum foil (1 cm^2) as counter electrode, and stationary glassy carbon electrode (GCE) disk of 3 mm diameter coated with catalytic ink as working electrode. All potentials were converted to a reversible hydrogen electrode (RHE) scale.

The electrochemical performance of catalysts was assessed from polarisation curves depicted in Figure 1a and compared with bare GCE as reference and Pt/C as benchmark catalyst. Tafel slopes (Fig. 1b) were derived from polarization curves in alkaline environment. The onset potential and potentials needed to attain current density of 10 $mA.cm^{-2}$ and -100 $mA.cm^{-2}$ along with Tafel slope values and values of exchange current density are summarized in Table 1.

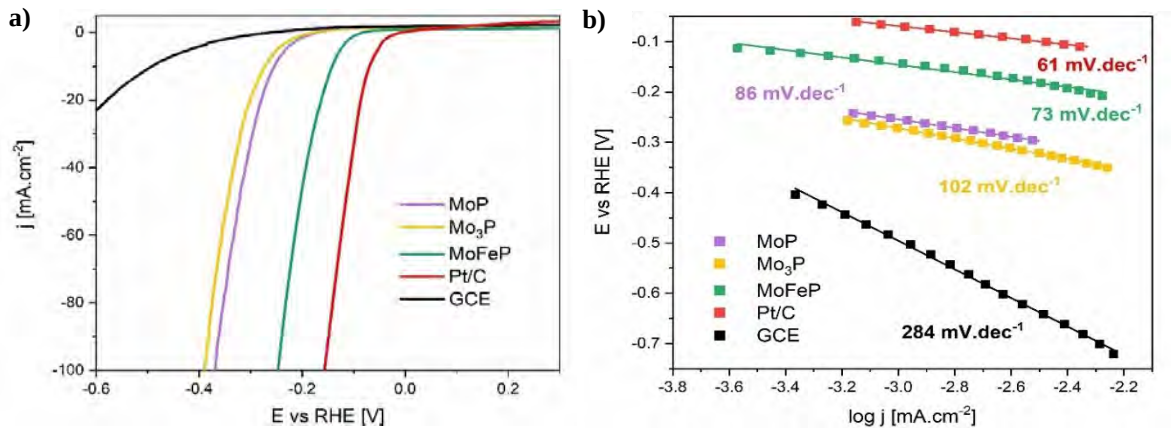

Fig. 1 a) polarization curves of catalytic inks on stationary GCE in 1 M KOH at scan rate 1 mV.s^{-1}, b) Tafel slopes.

Tab. 1 Values of onset potential, overpotentials at current densities of -10 mA.cm^{-2} and -100 mA.cm^{-2}; Tafel slopes, and exchange current densities for all samples in alkaline medium.

Sample	*-E_{onset}*	*η_{10} [mV]*	*η_{100} [mV]*	*b [mV.dec^{-1}]*	*j_0 [mA.cm^{-2}]*
MoP	170	253	369	86	1.2 10^{-6}
Mo_3P	181	271	389	102	2.0 10^{-6}
MoFeP	82	142	246	73	1.3 10^{-5}
Pt/C	7	69	157	61	7.9 10^{-5}
GCE	260	490	-	284	2.0 10^{-5}

The bimetallic phosphide MoFeP exhibited the lowest overpotentials (e.g. -142 mV at -10 mA.cm^{-2}) among the prepared samples. Activity of Mo phosphides was significantly worse as documented by HER overpotentials of -253 mV and -271 mV at -10 mA.cm^{-2} for MoP and Mo_3P, respectively. The lowest value of Tafel slope was recorded for MoFeP with only 73 mV.dec^{-1}, approaching Tafel slope value of commercial Pt/C with 61 mV.dec^{-1}. Binary phosphide was followed by MoP (86 mV.dec^{-1}) and then Mo_3P with value 102 mV.dec^{-1}.

The bimetallic catalyst exhibited superior electrocatalytic performance in terms of lower overpotentials and Tafel slopes in alkaline environment. This is due to the presence of Fe, which increased the number of active sites. The fact that MoFeP catalyst contains neither precious metals nor critical raw materials makes its relevant candidate for future larger scale application.

Acknowledgements

This work was supported by the Scientific Grant Agency of the Ministry of Education, Science, Research and Sport of the Slovak Republic (project VEGA 1/0095/21), and the Slovak Research and Development Agency (project APVV-20-0299 and no. APVV-20-0576).

References

[1] A. A. Feidenhans'l, Y. N. Regmi, C. Wei, D.g Xia, J. Kibsgaard, and L. A. King, " Precious Metal Free Hydrogen Evolution Catalyst Design and Application," *Chem. Rev.*, vol. 124, no. 9, pp. 5617−5667, 2024, doi: 10.1021/acs.chemrev.3c00712.

[2] H. Sun, X. Xu, H. Kim, W. C. Jung, W. Zhou, and Z. Shao, " Electrochemical Water Splitting: Bridging the Gaps Between Fundamental Research and Industrial Applications," *Energy Environ. Mater.*, vol. 6, no. 5, p. e12441, 2023, doi: 10.1002/eem2.12441.

[3] T. O. Ogundipe, L. Shen, YanShi, Z. Lu, and C. Yan, "Recent Advances on Bimetallic Transition Metal Phosphides for Enhanced Hydrogen Evolution Reaction," *ChemistrySelect*, vol. 7, no. 23, p. e202200291, 2022, doi: 10.1002/slct.202200291.

[4] A. Karmakar, K. Kannimuthu, S. S. Sankar, K. Sangeetha, R. Madhu, and S. Kundu,"Vast Exploration on Improvising Synthetic Strategies in Enhancing OER Kinetics of LDH Structures: a Review," *J. Mater. Chem. A*, vol. 9, no. 3, pp. 1314-1352, 2021, doi: 10.1039/D0TA09788H.

[5] Y. Long, Y. Shen, P. Jiang, H. Su, J. Xian, Y. Sun, J. Yang, H. Song, Q. Liu and G. Li, "Ultrafine Ru nanoparticles stabilized by V8C7/C for enhanced hydrogen evolution reaction at all pH," *Sci. Bull.*, vol. 69, no. 6, pp. 763-771, 2024, doi: 10.1016/j.scib.2024.01.014.

[6] M. I. Jamesh, "Recent progress on earth abundant hydrogen evolution reaction and oxygen evolution reaction bifunctional electrocatalyst for overall water splitting in alkaline media," *J. Power Sources*, vol. 333, pp. 213-236, 2016, doi: 10.1016/j.jpowsour.2016.09.161.

[7] C. Bera, M. Streckova, R. Orinakova, A. Guboova, T. Bystron, V. Girman, F. Kromka, M. Podobova, K. Bouzek, "NiCoP fibers as novel catalysts for hydrogen evolution in alkali and acidic environment," *Int. J. Hydrogen Energy*, vol. 60, pp. 118-132, 2024, doi: 10.1016/j.ijhydene.2024.02.195.

Conductive Biodegradable Bone Substitutes Consist of Metal-Polymer Composites

K. Ozaltin[a]*, R. Gorejova[b], C. Wiener[c], A. Przekora-Kusmierz[d], P. Saha[a]

[a] Centre of Polymer Systems, University Institute, Tomas Bata University in Zlín, Třída Tomáše Bati 5678, 76001 Zlín, Czech Republic
[b] Department of Physical Chemistry, Faculty of Science, P.J. Šafarik University in Košice, Moyzesova 11, 041 54, Košice
[c] Department of Materials Science and Engineering, Budapest University of Technology and Economics. Műegyetem rakpart 3., Budapest H-1111, Hungary
[d] Independent Unit of Tissue Engineering and Regenerative Medicine, Faculty of Biomedicine, Medical University of Lublin, Chodzki 1, 20-093 Lublin, Poland
*ozaltin@utb.cz

The use of biodegradable metals as an implant or fixation device is becoming attractive due to their biodegradation behavior in the body during healing. Besides their mechanical support, cellular compatibility and hemocompatibility are other important parameters to avoid complications and faster healing. Within this study, zinc (Zn) is used as a degradable metallic substrate, however, Zn alone was found toxic to human osteoblast cells and mouse fibroblast cells. Alloying Zn with a certain amount of Mg performed better cytotoxicity results, but was not in the range of cytocompatibility level. Therefore, the surface of Zn was coated with hydroxyapatite (HAp) via an electrochemical deposition technique (Figure 1). HAp is a bioactive ceramic and promotes cellular interaction, proliferation, and bone growth with osseointegration. As expected, cytocompatibility was achieved with HAp deposition. Introducing conductivity for improving the cell interactions was achieved by using gold nanoparticles embedded in Chitosan solution and layered on HAp-deposited Zn surface. Achieving the hemocompatible surface, marine-based Fucoidan immobilized on Chi-Au surface after activation by radio-frequency plasma (13.56 MHz) via carbodiimide chemistry.

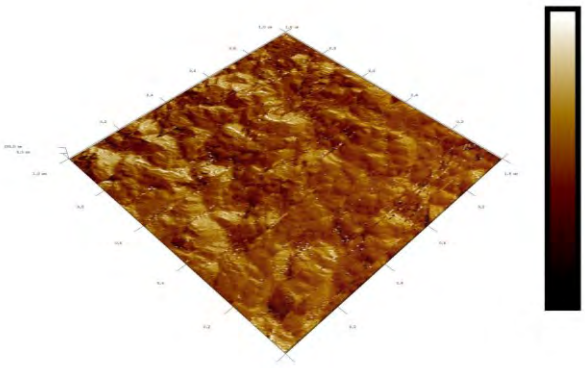

Fig. 1 AFM image of Zinc surface coated with hydroxyapetite via electrochemical deposition. (1x1 µm).

Acknowledgements

This work was supported by the Slovak Research and Development Agency under the project APVV-20-0278 and by the Visegrad Grant from International Visegrad Fund. (project no. 22310096)

8th International Conference on Novel Materials Fundamentals and Applications
High Tatras, 13.-16.10.2024

A Novel Multi-Metallic Electrocatalyst for the Hydrogen Evolution Reaction: Synthesis and Activity Testing

M. Paračková[a]*, R. Oriňaková[a], M. Strečková[b], A. Gubóová[a,b]

[a] Department of Physical Chemistry, Faculty of Science, P.J. Šafárik University in Košice, Moyzesova 11, 040 01 Košice, Slovakia
[b] Institute of Materials Research, Slovak Academy of Sciences, Watsonova 47, 040 01 Košice, Slovakia
*maria.parackova@student.upjs.sk

At present, the human race faces severe energy and environmental challenges, including climate change, industrial pollution and a growing global population demanding more energy. To build a sustainable future, the transition from fossil fuel-based energy sources to renewable alternatives is being pursued. As the cost of renewable electricity continues to decline, the production of basic chemical feedstocks by environmentally benign renewable energy-driven electrochemical synthesis is becoming financially attractive [1], [2], [3]. One of the feedstocks essential for industrial applications is hydrogen, which can be ecologically produced via water electrolysis. Although this process was first demonstrated in 1789, its application remains limited, and most hydrogen is currently derived from fossil fuels. To promote wider utilisation of this production method, developing cost-effective, stable and active electrocatalysts for both half-reactions of water electrolysis is crucial [4], [5], [6]. Recently, multi-metallic electrocatalysts have attracted significant attention due to their enhanced catalytic performance and stability [7], [8].

Therefore, this work focuses on the preparing a novel multi-metallic material and subsequent testing of its electrocatalytic activity for the hydrogen evolution reaction (HER). This catalyst was synthesized from 5 metal salts ($Cu(NO_3)_2 \cdot 3\ H_2O$; $Fe(NO_3)_3 \cdot 9\ H_2O$; $Ni(NO_3)_2 \cdot 6\ H_2O$; $(NH_4)_6Mo_7O_{24} \cdot 4\ H_2O$; $Zn(NO_3)_2 \cdot 6\ H_2O$) using sol-gel method. In addition to the metal precursors, citric acid was used as the complexing agent and ammonia solution was employed to maintain pH. The resulting mixture was evaporated, dried and sintered at 300 °C in a reducing atmosphere to obtain fine powder. This catalyst was then subjected to catalytic activity testing and its performance was compared with a bare glassy carbon electrode and commercial 10 wt% Pt/C. Electrocatalytic activity evaluations were conducted in both acidic and alkaline media using a three-electrode setup, with a glassy carbon rotating ring-disc electrode (GCE) as the working electrode. The catalyst powder and Pt/C were drop-casted onto the GCE in the form of ink, with a calculated powder loading of approximately 1 $mg \cdot cm^{-2}$. As can be seen from current-potential curves (Fig.1), the catalyst we prepared exhibited moderate activity towards HER in both environments.

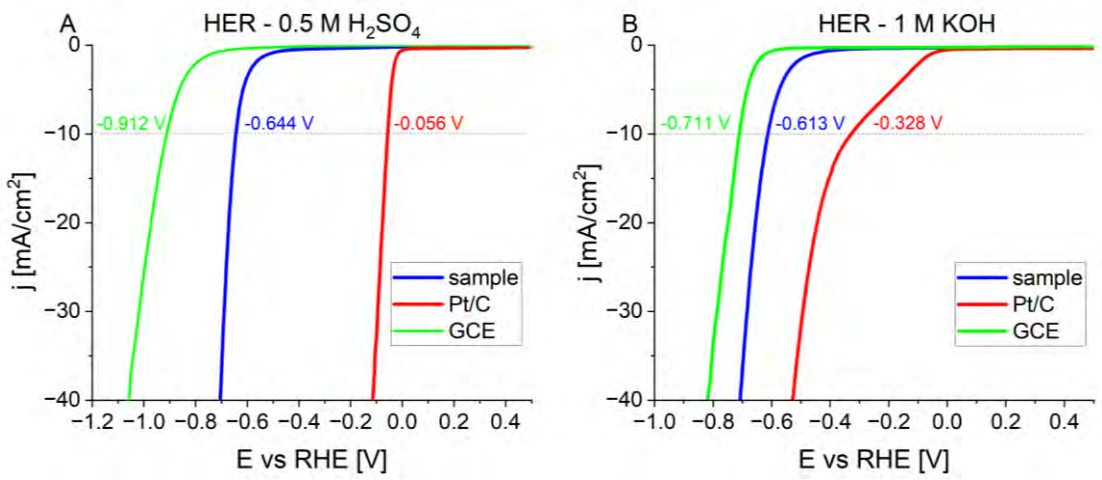

Fig. 13 HER current-potential curves for bare GCE, prepared material and Pt/C in A) acidic and B) alkaline media.

Acknowledgements

This work was funded by the EU NextGenerationEU through the Recovery and Resilience Plan for Slovakia under the project No. 09I03-03-V05-00008 through Internal Scientific Grant System - ESGD Program of Pavol Jozef Šafárik University in Košice (vvgs-2023-2957); Slovak Research and Development Agency under the No. APVV-20-0299 (Electrocatalysts for efficient hydrogen production for future electrolysers and fuel cells) and the Scientific Grant Agency of Ministry of Education, Science, Research and Sport of the Slovak Republic and the Slovak Academy of Sciences (VEGA) under project No. 1/0095/21 (Application of innovative nano catalysts and DFT simulations for efficient hydrogen production).

References

[1] F.-Y. Chen, Z.-Y. Wu, Z. Adler, and H. Wang, "Stability challenges of electrocatalytic oxygen evolution reaction: From mechanistic understanding to reactor design," *Joule*, vol. 5, no. 7, pp. 1704–1731, Jul. 2021. doi: 10.1016/j.joule.2021.05.005.

[2] G. Allegretti, M. A. Montoya, and E. Talamini, "Renewable energy for a sustainable future," *The Renewable Energy-Water-Environment Nexus: Fundamentals, Technology, and Policy*, pp. 1–36, Jan. 2024. doi: 10.1016/B978-0-443-13439-5.00001-6.

[3] P. Igeland, L. Schroeder, M. Yahya, Y. Okhrin, and G. S. Uddin, "The energy transition: The behavior of renewable energy stock during the times of energy security uncertainty," *Renewable Energy*, vol. 221, p. 119746, Feb. 2024. doi: 10.1016/J.RENENE.2023.119746.

[4] S. Zhang, X. Zhang, Y. Rui, R. Wang, and X. Li, "Recent advances in non-precious metal electrocatalysts for pH-universal hydrogen evolution reaction," *Green Energy & Environment*, vol. 6, no. 4, pp. 458–478, Aug. 01, 2021. doi: 10.1016/j.gee.2020.10.013.

[5] G. Chrisholm, T. Zhao, and L. Cronin, "Hydrogen from water electrolysis," *Storing Energy*, pp. 559–591, 2022. doi: 10.1016/b978-0-12-824510-1.00015-5.

[6] C. Bera *et al.*, "NiCoP fibers as novel catalysts for hydrogen evolution in alkali and acidic environment," *Int J Hydrogen Energy*, vol. 60, pp. 118–132, Mar. 2024. doi: 10.1016/J.IJHYDENE.2024.02.195.

[7] S. Chen *et al.*, "Multi-metal electrocatalyst with crystalline/amorphous structure for enhanced alkaline water/seawater hydrogen evolution," *J Colloid Interface Sci*, vol. 650, pp. 807–815, Nov. 2023. doi: 10.1016/j.jcis.2023.07.048.

[8] G. Borisov, V. Bachvarov, H. Penchev, R. Rashkov, and E. Slavcheva, "Multi-metallic electrodeposited catalysts applicable for oxygen evolution reaction in AEM water electrolysis," *Mater Lett*, vol. 286, p. 129248, Mar. 2021. doi: 10.1016/j.matlet.2020.129248.

The Processing and Microstructural Evolution of Reactive Sintered (Ti-Zr-Nb-Hf-Ta)B2 + (Ti-Zr-Nb-Hf-Ta)C High-Entropy Ceramics.

O. Petruš[a]*, A. Naughton-Duszová[a], P. Švec[b], M. Hrubovčáková[a], M. Vojtko[a], P. Hvizdoš[a], J. Dusza[a,c]

[a] Institute of Materials Research, Slovak Academy of Sciences, Watsonová 47, Košice, 040 01, Slovakia
[b] Institute of Physics, Slovak Academy of Sciences, Dúbravská cesta 9, Bratislava, 845 11, Slovakia
[c] Bánki Donát Faculty of Mechanical and Safety Engineering, Óbuda University, Népszínház Utca 8, Budapest, 1081, Hungary
*opetrus@saske.sk

Ultra-high temperature ceramics (UHTCs) are ceramic composites formed when boron, carbon, or nitrogen combine with early transition metals like Ti, Zr, Nb, Hf, or Ta, and exhibit melting points above 3000°C [1]. This emerging class of materials holds great promise for use in extreme environments such as aerospace, as well as in applications like advanced nuclear fission reactors, high-temperature electrodes for metal refining, and many other fields [2]. Recently, a new class of UHTCs, inspired by the success of high-entropy alloys, has been explored for the first time in the form of high-entropy ceramics. These materials were first reported in 2016 as a bulk boride-based system [3]. The development of advanced ceramic composite systems like the above-mentioned DPHE-UHTCs requires thorough and dedicated microstructural characterization. In recent years, extensive analyses using XRD, SEM, and STEM, combined with energy dispersive spectrometry, have been employed to examine the nano-scale and atomic-scale structure of high-entropy ceramics in several studies [4]. These investigations confirmed that the crystal structure's integrity remained intact after the incorporation of transition metal elements into the solid solution, which were found to be distributed across the boride and carbide phases. Structural and thermodynamic analyses validated the thermodynamic principles that govern the compositions of the boride and carbide phases at equilibrium, causing them to deviate from equimolar ratios—an essential factor in designing dual-phase high-entropy UHTCs [5]. It was also established that studying solid solution structures at the atomic scale, both within individual grains and at grain and phase boundaries, can enhance the understanding of the structure-property relationships in these new high-entropy ceramics. This offers a valuable experimental foundation for the design of new systems with exceptional properties in terms of composition and structure. The current investigation aims to conduct a focused and detailed study to analyze and characterize the microstructural development of the recently developed reactive-sintered (Ti-Zr-Nb-Hf-Ta)B_2 + (Ti-Zr-Nb-Hf-Ta)C high-entropy ceramic composite at the micro, nano, and atomic scales.

A novel high-entropy, compositionally complex composite consisting of dual-phase (Ti-Zr-Nb-Hf-Ta)B_2 and (Ti-Zr-Nb-Hf-Ta)C was synthesized using reactive spark plasma sintering with commercially available ZrB_2, NbB_2, HfB_2, TaB_2, and TiC powders. The resulting composite, characterized by high density, is primarily composed of boride (~39.7 vol%) and carbide (~56.4 vol%) phases, with a minor presence of (Hf-Zr)O_2. Due to the coupling effect of reactions and solid solution formation, the microstructure is homogeneous and relatively fine, with average grain sizes of 3.4 μm for the boride phase and 2.2 μm for the carbide phase. Large-area SEM analysis showed no evidence of microcracks, micropores, large grains, or clusters. Detailed investigation at the micro, nano, and atomic levels focused on the local chemical composition and element distribution, revealing that Ti primarily dissolves into the boride phase, while the other elements favor the carbide phase, forming a $(Ti_{0.82}Zr_{0.04}Nb_{0.08}Hf_{0.03}Ta_{0.03})B_2$ + $(Ti_{0.49}Zr_{0.12}Nb_{0.13}Hf_{0.11}Ta_{0.15})C$ system. Grain and phase boundary interface analysis showed a continuous segregation of Fe and Co impurity atoms, forming a layer less than 1.5 nm wide. Atomically flat basal interfacial termination planes (001), decorated with a monoatomic Zr-enriched layer in the boride phase, were also observed. Additionally, metal-rich compositions were detected at triple points at the grain and phase boundaries, attributed to impurities in the raw powders.

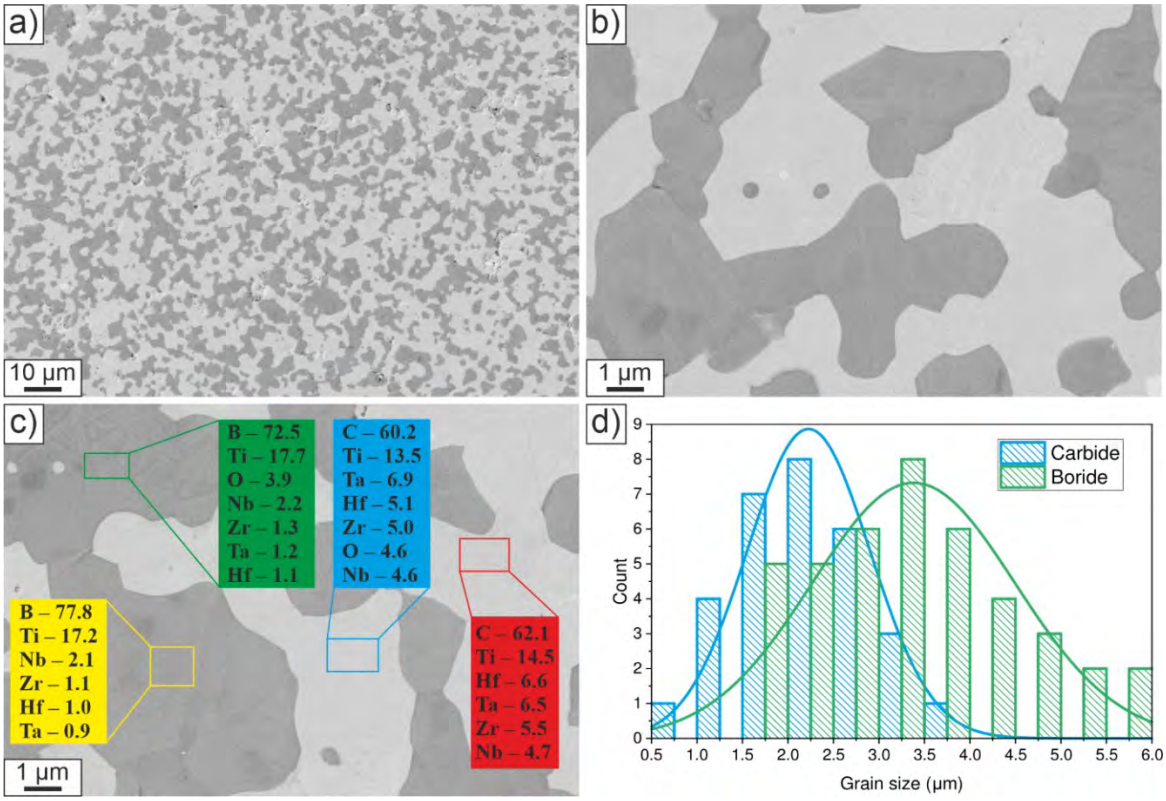

Fig. 1 SEM micrographs presenting typical spatial distribution of boride (darker) and carbide (lighter) grains (a,b), EDS results in indicated areas (c), grain–size distributions of the boride and carbide grains, (d).

Acknowledgements

Funding from the European Union's Horizon 2020 Research and innovation Programme was used for this Project on the basis of a Grant agreement under the Marie Skłodowska-Curie funding scheme No. 945478 and Slovak Research and Development Agency under the contract no. APVV 20-0229

References

[1]W. G. Fahrenholtz, E. J. Wuchina, W. E. Lee, and Y. Zhou, *Ultra-High Temperature Ceramics: Materials for Extreme Environment Applications,*. John Wiley & Sons Ltd, 2014.

[2]W. G. Fahrenholtz and G. E. Hilmas, "Ultra-high temperature ceramics: Materials for extreme environments," *Scr. Mater.*, vol. 129, pp. 94–99, 2017, doi: 10.1016/j.scriptamat.2016.10.018.

[3]J. Gild *et al.*, "High-Entropy Metal Diborides: A New Class of High-Entropy Materials and a New Type of Ultrahigh Temperature Ceramics," *Sci. Rep.*, vol. 6, no. October, pp. 2–11, 2016, doi: 10.1038/srep37946.

[4]A. Naughton-Duszová *et al.*, "On the phase and grain boundaries in dual phase carbide/boride ceramics from micro to atomic level," *J. Eur. Ceram. Soc.*, vol. 43, no. 15, pp. 6765–6773, 2023, doi: 10.1016/j.jeurceramsoc.2023.07.034.

[5]M. Qin *et al.*, "Dual-phase high-entropy ultra-high temperature ceramics," *J. Eur. Ceram. Soc.*, vol. 40, no. 15, pp. 5037–5050, 2020, doi: 10.1016/j.jeurceramsoc.2020.05.040.

8th International Conference on Novel Materials Fundamentals and Applications
High Tatras, 13.-16.10.2024

DFT Study of HER Reaction on MoP(101), (110) and (100) Surfaces

N. Podrojková[a]*, A. Guboová[b], M. Strečková[b], R. Oriňaková[a]

[a] Department of Physical Chemistry, Pavol Jozef Šafárik University, Moyzesova 11, 04001 Košice, Slovakia
[b] Institute of Materials Research, Slovak Academy of Science, Watsonova 47, 04001 Košice, Slovakia
*natalia.podrojkova@upjs.sk

Decreasing the use of fossil fuels and reliance on them while also creating a sustainable energy system are crucial global priorities today. Using hydrogen (H_2) as a fuel or energy carrier seems to be one of the most effective solutions.[1]

Water electrolysers (WE) provide a sustainable energy conversion option instead of fossil fuel-based technologies by effectively breaking down water to create environmentally friendly H_2 using the hydrogen evolution reaction (HER). Developing stable catalysts with both high activity and long-term durability is a common strategy to enhance the kinetics of water electrolysis. Currently, platinum (Pt) is the most efficient electrocatalyst, however, its scarcity and high price obstruct broad industrial application.[2]

Transition metal phosphides (TMPs) show impressive catalytic characteristics, strong stability, and bifunctional properties, which make them appealing catalysts for water splitting with potential as substitutes for Pt-group catalysts. This strong activity is inflicted due to the presence of phosphorus and metal sites, which behave as proton and hydride acceptor sites in the HER.[3] Molybdenum phosphide (MoP) is a type of non-oxide materials that is becoming increasingly popular as a catalyst for HER reaction due to the high electrocatalytic activity in bulk form. However, the crystallographic facets of catalytic surfaces are generally recognized for showing distinct activity in the HER. In addition, both theoretical and experimental studies have demonstrated that various facets, including those on the same catalyst or crystal material, can display significantly varying levels of HER activity, based on their crystallographic orientations.[4]

A comprehensive knowledge of the process through which HER catalysis takes place is essential fo the advancement of better catalysts. The relationship between HER activity and different facets could be examined and understood more deeply using density functional theory (DFT). Therefore, DFT as a quantum mechanical modelling method offers gaining additional insights into the electrolysis of water with phosphide-based catalysts. It can be utilized to calculate the activation energy, Gibbs free energy, specific transition states, or individual reaction steps of the processes and lead to experimentally improved catalytic MoP material.

Hence, we used Quantum ESPRESSO software to perform DFT calculations of hydrogen interaction on a MoP(101), (110) and (100) surfaces. The MoP hexagonal unit cell was optimized with lattice parameters a = 3.345 Å, c = 3.448 Å, $\alpha = \beta = 90°$, and $\gamma = 120°$. The Bridge (B), Top (T), and Hollow (H) sites of MoP(101), (110) and (100) facets were exposed to hydrogen adsorption. The most interesting sites according to Gibbs free energy values are MoP(101) B_1 (Fig. 1a, b), MoP(110) T_2 (Fig. 1c, d) and MoP(100) T_2 (Fig. 1e, f) sites with ΔG_{H^*} of -0.66, -0.23 and -0.15 eV, subsequently (Fig. 1g).

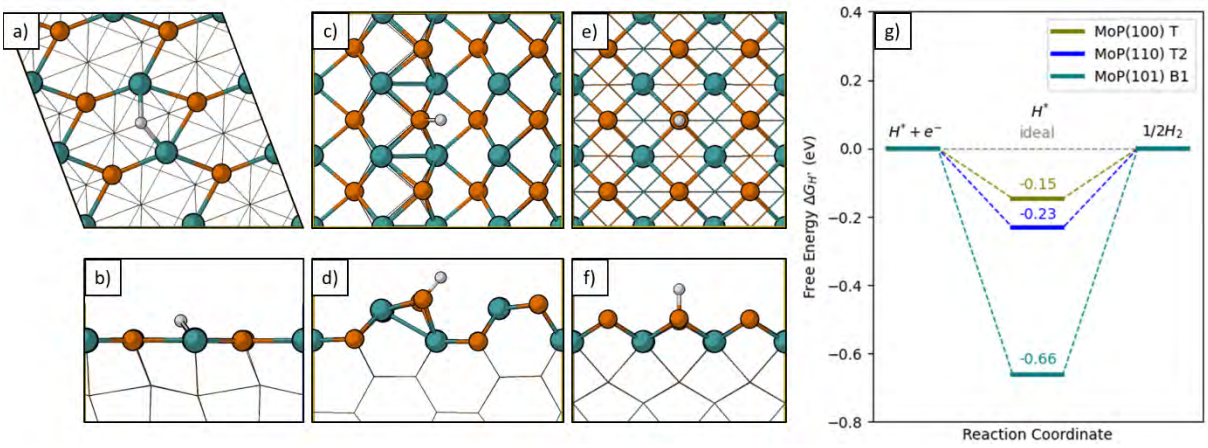

Fig. 1 Adsorbed H atom on a), b) MoP(101) B_1 site, c), d) MoP(110) T_2 site and e), f) MoP(100) T_2 site; g) diagram of calculated ΔG_{H^*} in eV for adsorbed H atom on MoP(101) B_1, MoP(110) T_2 and MoP(100) T_2 site.

The resulting outcomes will be used to identify transition states and compared to theoretical calculations of the hydrogen atom interaction with other transition metal phosphides. Theoretical investigations will also be compared with our experimental research on MoP material which will improve the understanding of HER reaction occuring on TMPs.

Acknowledgements

This work was supported by the Scientific Grant Agency of the Ministry of Education, Science, Research and Sport of the Slovak Republic (project VEGA 1/0095/21 and VEGA 2/0027/23), the Slovak Research and Development Agency (project APVV-20-0299 and no. APVV-20-0576), the European Regional Development Fund Project 'Fuel Cells with Low Platinum Content' (No. CZ.02.1.01/0.0/0.0/16_025/ 0007414) and the Scholarships for excellent researchers R2 from Recovery plan (09I03-03-V04-00086 project HERAQUAS).

References

[1] B. Sundén, "Hydrogen, Batteries and Fuel Cells," *1st ed. Elsevier, London: Academic Press*, 2019.

[2] S. Wang, L. Aolin, Ch.-J. Zhong, "Hydrogen production from water electrolysis: role of catalysts" *Nano Converg.*, vol. 8, no. 4, pp. 1-23, doi: 10.1186/s40580-021-00254-x.

[3] A. W. Bazeh, D. M. Kabtamu, Y.-Ch. Chang, T. H. Wondimu, H.-Ch. Huang, Ch.H. Wang, "Carbon and metal-based catalysts for vanadium redox flow batteries: a perspective and review of recent progress." *Sustain. Energ. Fuels*, vol. 5, pp. 1668-1707, doi: doi.org/10.1039/D0SE01723J.

[4] O. O. Dada, S. Karimzadeh, P. E. Imoisili, T.-Ch. Jen, "Theoretical insights of electrocatalytic hydrogen evolution on MoP nanocrystal." *Int. J. Hydrog. Energy*, vol. 48, no. 89, pp. 34634-34648, doi: 10.1016/j.ijhydene.2023.05.302.

Redox Flow Batteries – Materials and Components

E. Romadina[a]*, I. Derr[a], J. Asenjo[a], T. Kosicky[a], N. Podrojkova[b], A. Strakova Fedorkova[b], M. Palko[c], F. Dominik[c]

[a] INO-HUB Energy j.s.a., Tomášikova 30, 821 01 Bratislava, Slovakia
[b] Institute of Chemistry, Faculty of Science, Pavol Jozef Šafárik University in Košice, Moyzesova 11, 040 01 Košice, Slovakia
[c] Strojnícka fakulta, Technická univerzita v Košiciach, Park Komenského 12A, 042 00 Košice, Slovakia
*elena.romadina@inohub.sk

As the world shifts towards renewable energy, the safety and reliability of energy storage systems have become crucial. Vanadium Redox-Flow Batteries (VRFBs) are emerging as a leading solution for their efficiency and superior safety profile compared to other energy storage technologies.

One of VRFBs' key safety advantages is their non-flammable nature. Unlike lithium-ion batteries, which pose risks of thermal runaway and fires, VRFBs utilize aqueous electrolytes, making them inherently safer. This characteristic makes them an ideal choice for large-scale energy storage, where safety is paramount.

The operational benefits of VRFBs are manifold:

- Extended Lifespan: VRFBs offer up to 20,000 charge/discharge cycles, drastically reducing the need for frequent replacements.
- Maintenance Advantages: They require minimal maintenance, further lowering long-term operational costs.
- Energy Efficiency: VRFBs maintain a high level of efficiency throughout their lifespan, ensuring consistent energy storage and output.

Ino-Hub Energy, a Slovak company specializing in energy storage solutions, is at the forefront of developing Redox Flow Battery (RFB) technologies to integrate renewable energies into the grid and support grid balancing and peak shaving. In 2021, InoHub Energy was recognized by the European Commission as part of the Important Project of Common European Interest (IPCEI) for its design of an Energy Center based on flow battery concepts. The InoHub R&D team is currently researching various technologies, such as VRFB and All-Organic Redox Flow Batteries (AORFB), as well as battery stack design and testing of stack component materials.

Designing a new stack is a complex task. Ino-hub Energy chose to develop a sophisticated stack with a power density of at least 200 mW/cm² and 80% energy efficiency at the DC level, prioritizing higher power output over simplicity and lower cost.Electrode area was selected to be over 1000 cm², allowing each stack to generate more than 8 kW of power, thus reducing the number of stacks needed for megawatt-scale systems.

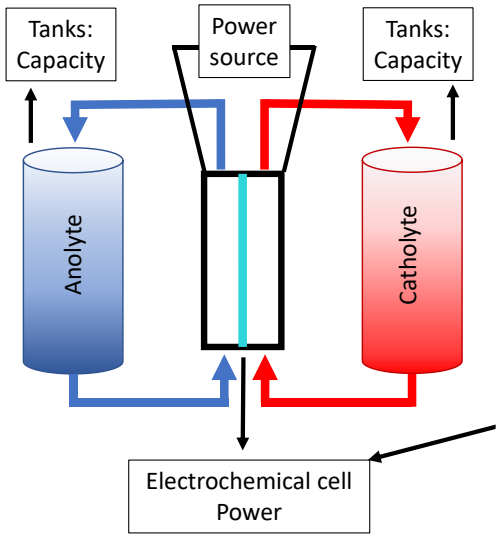

Fig. 1 Redox flow battery system.

Fabrication of Au-modified Pd Thin Films as Efficient ORR Catalysts in Acidic Media

F. D. Sanij[a]*, V. Latyshev[a], S. Vorobiov[a], H. You[b], D. Volavka[a], T. Samuely[a], V. Komanicky[a]

[a] Institute of Physics, Faculty of Science, P. J. Safarik University, Park Angelinum 9, Kosice 040 01, Slovak Republic.
[b] Materials Science Division, Argonne National Laboratory, Argonne, Illinois 60439, USA.
*fereshteh.dehghani.sanij@upjs.sk.

Introduction

Due to escalating climate change and decreasing fossil fuel resources, the development of environmentally friendly energy systems with high efficiency is essential. Fuel cells are an attractive option for renewable energy conversion technologies owing to their high efficiency, eco-friendliness, and affordability [1]. Nevertheless, the slow oxygen reduction reaction (ORR) kinetics of fuel cells severely hinder their effectiveness. Pt-based catalysts are most effective for improving ORR in acidic conditions. In spite of this, the prohibitive price and rarity of Pt prevent widespread commercialization [2]. Therefore, it is imperative to design low-cost oxygen reduction catalysts with activity comparable to Pt.

Bimetallic Pd-based systems have shown considerable potential under acidic circumstances because of the synergistic effects between Pd and additional elements that promote oxygen reduction kinetics [3], [4]. Specifically, Au/Pd catalysts have attracted enormous attention thanks to the modification of the electronic structures of Pd with Au, resulting in remarkable ORR performance [5].

In this study, Au films were deposited on various M (M = Pd, Pt, Rh, Ir, and Ru) electrode surfaces (Au/M) via the magnetron sputtering technique for oxygen reduction. Among the prepared Au/M catalysts, Au/Pd displayed the best performance for oxygen reduction electro-catalysis. In this regard, we synthesized Au-modified Pd (Au/Pd) thin films with a range of Au thickness (0.16, 0.24, 0.5, and 1 nm) to investigate their ORR electrocatalytic activities. Despite the inactivity of bulk Au, the ultrathin 0.16 nm Au film on Pd (0.16 nm Au/Pd) revealed markedly superior ORR activities. The enhanced performance of the optimum Au/Pd catalyst results from Au modification, the synergistic effects between the Pd and Au constituents, and the distinct electronic effects in bimetallic thin film systems.

Experimental section

Sample fabrication

Pt, Pd, Au, and Au/M thin films were deposited on the surface of glassy carbon (GC) electrodes utilizing the magnetron sputtering technique (Orion 8, AJA International sputtering system) from pure metal targets at room temperature. The sputtering deposition was performed at a pressure of 3 mTorr in the Ar atmosphere with a purity of 99.999%. The base pressure within the vacuum chamber was around 10^{-7} Torr. The Au/M thin films were prepared in a sequential manner, with Au on top of 20 nm pure metal (M) films. The deposition time of Au was controlled to achieve different Au thicknesses in Au/Pd catalysts.

Physical characterization

The surface morphology of the thin films was examined through atomic force microscopy (AFM, Bruker, ICON). The AFM images were recorded in tapping mode using silicon tips under ambient conditions. The X-ray photoelectron spectroscopy (XPS) measurements were conducted by the high-resolution spectrometer SPECS PHOIBOS 100/150 using an Al anode with a power of 200 W at room temperature. The pressure during the measurements was 10^{-8} mbar.

Electrochemical characterization

The electro-catalytic behaviors of fabricated thin films were assessed via a potentiostat (Autolab PGSTAT 302 N) coupled with a standard three-electrode electrochemical configuration. A glassy carbon electrode (GC, diameter: 6 mm) was used as the working electrode, and Pt wire and saturated Ag/AgCl (3 M NaCl) were used as the counter and reference electrodes, respectively. In all experiments, ultrapure (18 MΩ cm) deionized (DI) water (Elga Purelab Ultra) was employed to make aqueous solutions. The cyclic voltammetry (CV) measurements were carried out in 0.1 M $HClO_4$ solutions saturated with Ar in the potential range of -0.2 V~1 V and the scan speed of 50 mV/s. The ORR experiments were conducted by utilizing linear sweep voltammetry (LSV) on rotating disk electrodes (RDE) in O_2-purged 0.1 M $HClO_4$ solution at 10 mV/s with different rotation electrode speeds from 400 to 2025 rpm.

Results and discussion

Fig. 1 shows AFM images of pure Pd and 0.16 nm Au/Pd thin films. As can be seen in Figs. 1a and b, the synthesized thin films have a smooth surface. The average roughness of the 0.16 nm Au/Pd surface (0.244 nm) indicates a significant increase compared with that of the Pd thin film catalyst (0.181 nm).

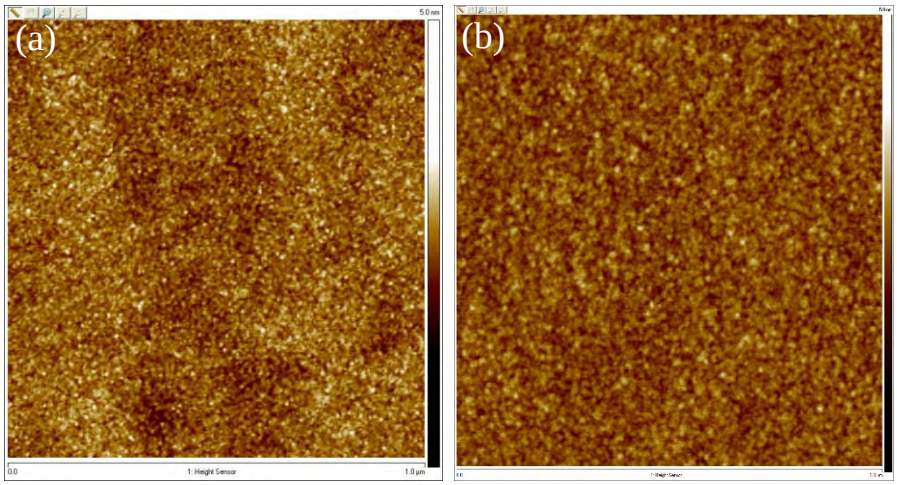

Fig. 1 AFM images of the pure Pd (a) and 0.16 nm Au/Pd (b) thin film samples.

The ORR catalytic behaviors of prepared thin films were evaluated in O_2-purged 0.1 M $HClO_4$ electrolytes. As illustrated in Fig. 2a, the oxygen reduction abilities of 0.16 nm Au/M (M = Pd, Pt, Rh, Ir, and Ru) thin films were investigated and compared with the Pt-alone catalyst. The oxygen reduction ability of the 0.16 nm Au layer on M electrodes progressed in the following order: Au/Ru < Au/Ir < Au/Rh < Au/Pt < Au/Pd. Fig. 2b displays the linear sweep voltammetry (LSV) curves at 1600 rpm from the rotating disk electrode (RDE) for fabricated Au/Pd thin films with different Au layer thicknesses. The ORR polarization curve of the 0.16 nm Au/Pd thin film catalyst revealed the most positive E_{onset} (0.58 V), which was close to that of the pure Pt sample (0.60 V) (Table 1). Compared to the pure Au thin film, the Au/Pd catalyst with 0.16 nm Au thickness had enhanced ORR activity. Despite Au atoms covering a portion of the Pd surface, 0.16 nm Au/Pd catalysts have oxygen reduction abilities similar to pure Pt catalysts. In addition, the fabricated catalysts with an Au thickness in excess of 0.16 nm showed negative shifts in $E_{1/2}$ with a corresponding decrease in current densities compared with pure thin films (Table 1). Clearly, the deposition of Au on Pd catalyst surfaces impacts ORR capabilities. It is suggested that an optimum Au thickness will decrease the

formation of oxygenated intermediates, which are regarded as poisoning species on the surface of Pd thin films during the ORR process.

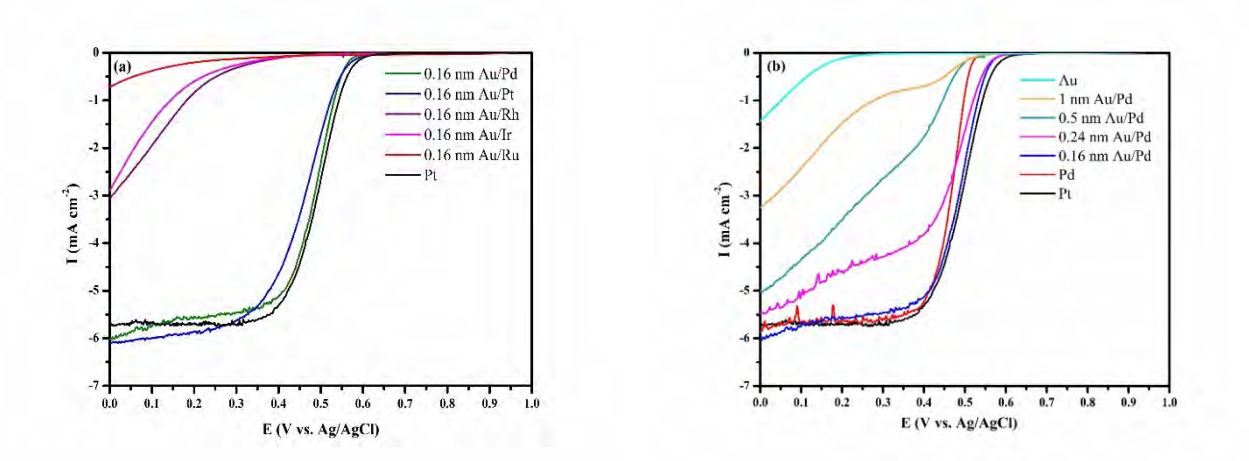

Fig. 2 Comparison of the ORR polarization curves of the pure Pt and different 0.16 nm Au/M (M = Pd, Pt, Rh, Ir, and Ru) samples (a), the ORR polarization curves of prepared thin film catalysts (b) in O_2-saturated 0.1 M $HClO_4$ at 1600 rpm, Potential scan rate: 10 mV s^{-1}.

As shown in Table 1, the Tafel slope of 0.16 nm Au/Pd was close to that of pure Pt, indicating the highly accelerated kinetics of this sample in oxygen reduction.

Tab. 1 Electrochemical properties of the prepared thin film catalysts in 0.1 M $HClO_4$.

Catalysts	E_{onset} (V vs. Ag/AgCl)	$E_{1/2}$ (V vs. Ag/AgCl)	Tafel slope (mV/dec)
Pt	0.60	0.50	59
Pd	0.53	0.46	55
0.16 nm Au/Pd	0.58	0.49	57
0.24 nm Au/Pd	0.56	0.45	58
0.5 nm Au/Pd	0.52	0.44	79
1 nm Au/Pd	0.50	0.43	83

Moreover, the 0.16 nm Au/Pd presented superior durability (just 10 mV loss in $E_{1/2}$) compared to the 0.16 nm Pt/Pd (around 30 mV loss in $E_{1/2}$) after 1000 continuous CV cycles. This can be ascribed to the gradual degradation of surface Pt during accelerated durability tests (ADTs).

Conclusions

In summary, we have prepared a highly active and stable Au/Pd ORR thin film catalyst using magnetron sputtering. Compared with the pure Pd sample, the 0.16 nm Au/Pd catalyst exhibited improved ORR activity with an $E_{1/2}$ of 0.49 V, approaching that of Pt thin films (0.50 V). The 0.16 nm Au/Pd electro-catalyst also displayed outstanding stability and methanol resistance under acidic conditions. We attribute the exceptional catalytic capability to the deposition of Au on Pd surfaces and synergistic interactions between Pd and Au, which provide abundant active sites and rapid electron transfer for ORR. This study shows that modified 0.16 nm Au/Pd thin films are promising candidates for high-performance oxygen reduction catalysts.

Acknowledgements

We thank Professor Kawaguchi, Tohoku U, for the useful discussion on X-ray reflectivity analysis. This work was supported by grants from the Slovak Research and Development Agency under contract APVV-20-0528 and the National Scholarship Programme of the Slovak Republic (NSP). The X-ray measurements performed at Argonne (HY) were supported by the U.S. Department of Energy (DOE), Office of Basic Energy Science (BES), Materials Sciences and Engineering Division under contract no. DE-AC02-06CH11357.

References

[1]W. Wang, Z. Jiang, X. Tian, T. Maiyalagan, and Z. J. Jiang, “Self-standing CoFe embedded nitrogen-doped carbon nanotubes with Pt deposition through direct current plasma magnetron sputtering for direct methanol fuel cells applications,” *Carbon N. Y.*, vol. 201, no. August 2022, pp. 1068–1080, 2023, doi: 10.1016/j.carbon.2022.10.022.

[2]M. Liu *et al.*, “Recent progress of electrocatalysts for oxygen reduction in fuel cells,” *J. Colloid Interface Sci.*, vol. 607, pp. 791–815, 2022, doi: 10.1016/j.jcis.2021.09.008.

[3]C. V. S. Almeida, F. Colmati, E. G. Ciapina, K. I. B. Eguiluz, and G. R. Salazar-Banda, “Nanowires of Pd and Pd alloys for fuel cell applications: A review of the current state-of-the-art,” *J. Electroanal. Chem.*, vol. 955, no. December 2023, 2024, doi: 10.1016/j.jelechem.2024.118073.

[4]T. Promanan, A. Chaisena, T. Sarakonsri, S. Thungprasert, and S. Narakaew, “Binary and ternary alloys based on Pd as cathode catalysts on nitrogen-doped reduced graphene oxide via polyol methods for proton exchange membrane fuel cell,” *Inorg. Chem. Commun.*, vol. 168, no. August, p. 112945, 2024, doi: 10.1016/j.inoche.2024.112945.

[5]X. X. Lin, X. F. Zhang, A. J. Wang, K. M. Fang, J. Yuan, and J. J. Feng, “Simple one-pot aqueous synthesis of AuPd alloy nanocrystals/reduced graphene oxide as highly efficient and stable electrocatalyst for oxygen reduction and hydrogen evolution reactions,” *J. Colloid Interface Sci.*, vol. 499, pp. 128–137, 2017, doi: 10.1016/j.jcis.2017.03.087.

Nanomodified Electrochemical Sensor for Bioanalytes Detection

J. Shepa[a]*, I. Šišoláková[a], R. Oriňaková[a]

[a] Pavol Jozef Šafárik University in Košice, Šrobárova 2, Košice, Slovakia
*jana.shepa@upjs.sk

Introduction

A significant heterocyclic component of urine, uric acid (2,6,8-trihydroxy purine) is mostly generated during the metabolism of purine. Normal physiological blood uric acid concentrations for men and women are 25–80 mg/L and 15–60 mg/L, respectively. Food and genetic variations make it very difficult for the body to maintain the proper level of uric acid. Meat and seafood have the potential to raise blood uric acid levels. Severe conditions like gout, hypertension, hyperuricemia, diabetes, heart failure, and Lesch–Nyhan syndrome can be brought on by an excessive amount of uric acid in the human body. As a result, it's critical to regularly check the body's uric acid levels using a sensitive and focused technique. Uric acid is determined using methods such as liquid chromatography, titration, capillary electrophoresis, and spectrophotometric analysis. But among the many disadvantages of these techniques is the heavy reliance on chemicals. Electrochemical methods have gained popularity among researchers because of their relatively low equipment costs, fast reaction times, ease of use, time savings, and real-time detection under in situ conditions [1].

Screen-printed carbon electrodes (SPCEs) are generally chosen for electrochemical studies due to their many superior properties, which include their wide potential window, high conductivity and adsorption capacity, low residual current, and ease of modification with aqueous/anhydrous matrices. Studies on the use of SPCEs modified with different metal nanoparticles for electrochemical applications have been published recently. In general, nanomaterials offer a greater surface area and a range of surface modification options, which may enhance the electron transfer process and alter a chosen metal's reduction potential value. Various kinds of nanomaterials, including nanoparticles, porous particles, nanospheres, nanocages, and nanoboxes, were employed to modify the electrodes for bioanalytes detection [2, 3].

The transition metals exhibit advantageous characteristics, including the capacity to achieve various oxidation states. Additionally, transition metals can take up electroactive species and create intermediates. Moreover, gold nanostructures are one of the many transition metal nanomaterials that are frequently applied for bioanalyted sensing. Among them, gold nanoparticles (AuNPs) have been the subject of numerous articles, because of their excellent catalytic qualities. Direct gold nanoparticle electrodeposition offers a way around the challenging preparation and application of novel materials [4]. Herein, the SPCE were modified by electrodeposited gold nanoparticles for uric acid detection, to improve electroanalytical properties of prepared sensor.

Results and Discussion

Gold nanoparticles were deposited onto the carbon working electrode of SPCE via cyclic voltammetry (from 0V to -1 V, 50 mV/s during 1 cycle). After the electrodeposition process, the current response of modified electrode was 1.3x higher in comparison to unmodified SPCE (Fig. 1A).

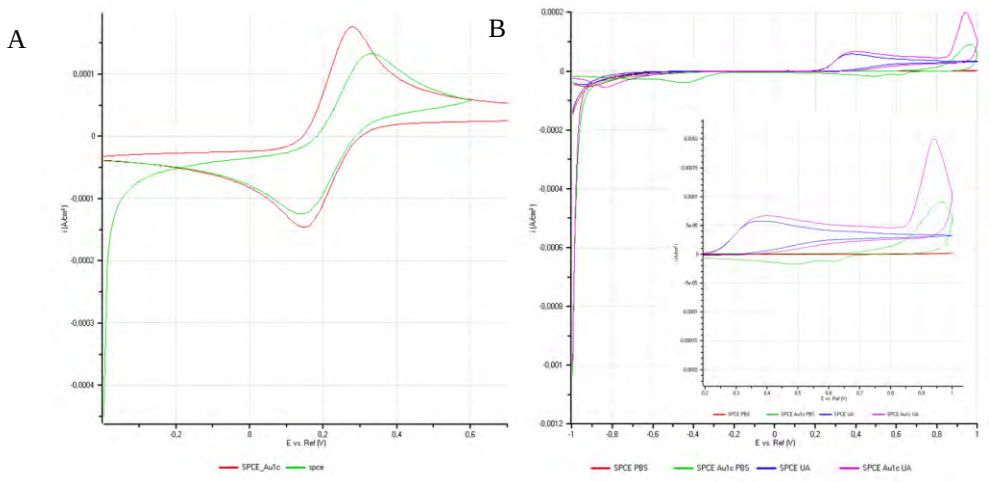

Fig. 14 Cyclic voltammograms for SPCE and SPCE/Au1c electrode in 5 mM $K_4[Fe(CN)_6]/K_3[Fe(CN)_6]$ + 1M KCl (A). Cyclic voltammograms for SPCE and SPCE/Au1c electrode in PBS and PBS with addition uric acid (B).

The active surface area was 1.66 cm^2 and 2.97 cm^2 for SPCE and SPCE/Au1c, respectively. Based on the cyclic voltammogram for SPCE/Au1c in PBS (Fig. 1B) on oxidation peak around 0.9 V was observed and pertain to oxidation of Au to Au_2O_3. For CV in the uric acid (UA) dissolved in the PBS solution there, were 2 peaks one for UA oxidation at 0.35 V and second at 0.9 V which correspond to oxidation of Au. Moreover, the current response was higher in comparison to SPCE/Au1c electrode in PBS, which indicated, that the oxidation of Au is influenced by UA presence in the solution, too. Based on this, there is possibility to detect UA at both potentials, but the potential at 0.35 V was chosen as better, because the potential values around the 0.8 V are typical for oxidation of various bioanalytes. The CV for various concentrations of UA were performed and calibration curve was fitted (Fig. 2). Electroanalytical characteristics of prepared sensor were measured and calculated, too. SPCE/Au1c displays linear range from 1.8 to 4.2 mM, with sensitivity of 10.15 μA/mM and limit of detection of 1.35 mM. Proposed sensor creates good platform for further test and modification in aim to enhance the electroanalytical properties and testing of other bioanalytes.

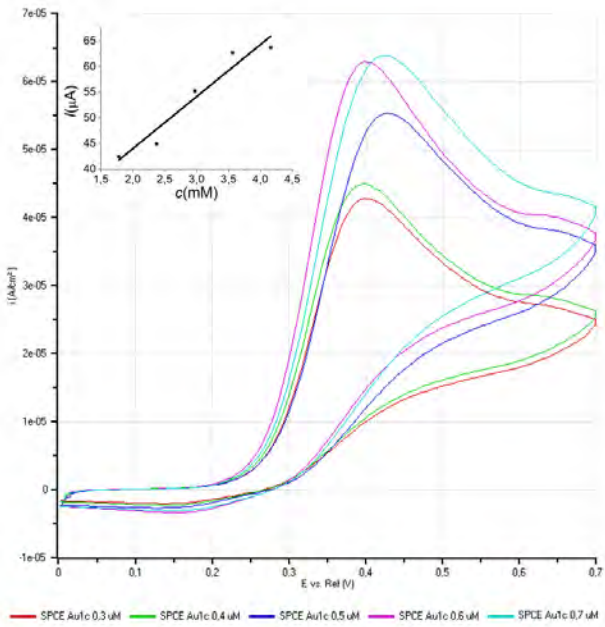

Fig. 15 Cyclic voltammograms of SPCE/Au1c electrode immersed in PBS solution with various concentration of uric acid. Insert: Calibration curve.

Acknowledgements

Funded by the EU NextGenerationEU through the Recovery and Resilience Plan for Slovakia under the project No. 09I03-03-V05-00008 and the NATO Science for Peace and Security Programme under grant id. G6106.

References

[1]S. Rajendrachari, H. Arslanoglu, A. Yaras, and S. M. Golabhanvi, "Electrochemical Detection of Uric Acid Based on a Carbon Paste Electrode Modified with Ta2O5 Recovered from Ore by a Novel Method," *ACS Omega*, vol. 8, no. 49, pp. 46946–46954, Dec. 2023, doi: 10.1021/acsomega.3c06749.

[2]J. Hovancová *et al.*, "Nanostructured Gold Microelectrodes for Non-enzymatic Glucose Sensor," *Electroanalysis*, vol. 31, no. 9, pp. 1680–1689, 2019, doi: 10.1002/elan.201900163.

[3]J. Hovancová *et al.*, "Gold Microelectrodes Decorated by Spike-Like Nanostructures as a Promising Non-Enzymatic Glucose Sensor," *Electroanalysis*, vol. 33, no. 2, pp. 347–354, 2021, doi: 10.1002/elan.202060207.

[4]J. Hovancová, I. Šišoláková, R. Oriňaková, and A. Oriňak, "Nanomaterial-based electrochemical sensors for detection of glucose and insulin," *Journal of Solid State Electrochemistry*, vol. 21, no. 8, pp. 2147–2166, 2017, doi: 10.1007/s10008-017-3544-0.

Novel eco and sustainable binders for Li-S batteries

A. Straková Fedorková[a]*, V. Niščáková[a], N. Podrojková[a], J. Leščinský[a]

[a] Pavol Jozef Safarik University of Kosice, Department of Physical chemistry, Srobarova 2, 040 01, Kosice
*andrea.fedorkova@upjs.sk

Research to enhance Li–S battery performance has largely concentrated on improving cathodes, particularly through carbon matrix designs. Other components, such as electrolytes, anodes, mechanisms, and binders, have received comparatively less attention. One effective strategy to address the shuttle effect has been embedding sulfur within a carbon matrix [1]. This has led to the exploration of various hierarchical sulfur composites, focusing on the concept of sulfur confinement within porous structures. Numerous carbon-based architectures have been developed and studied, including hollow carbon spheres, double-shell carbon spheres, nanofibers, 3D branched hollow nanolayers, hollow carbon nanotubes, tube-in-tube structures, and more [2]. Recently, incorporating graphene and graphene oxide into positive electrodes has yielded impressive results, such as longer cycling lifetimes and sustained capacity over hundreds of cycles.

However, these designs often suffer from complex manufacturing processes, high costs, and challenges in scaling up for industrial production. In light of these challenges, the critical role of binder materials in Li–S battery performance is increasingly acknowledged. Binders not only facilitate the assembly of electrodes but also participate actively in electrochemical reactions. Traditional binders like polyvinylidene fluoride (PVDF) face limitations, including poor adhesion, low conductivity, and reliance on toxic solvents such as N-methyl pyrrolidone (NMP) [3]. Newer binders like carboxymethylcellulose (CMC) and biopolymers such as alginates, chitosan, carrageenan, gelatin, gum arabic, guar gum, and tragacanth gum are environmentally friendly, require no toxic solvents, and can be produced using water-based synthesis methods. These biomass-based binders offer sustainability, cost-effectiveness, and abundant availability. They possess various physical and chemical properties that positively influence Li-S battery chemistry. Most natural binders are polysaccharides rich in -OH, $-SO4^{2-}$, and -COOH groups, making them water-soluble. Their numerous -OH groups facilitate interactions with polar environments and enhance binding with polysulfides. A particularly promising candidate is carrageenan. This study is focusing on novel binders and its use in small cells and also in prototype pouch cells.

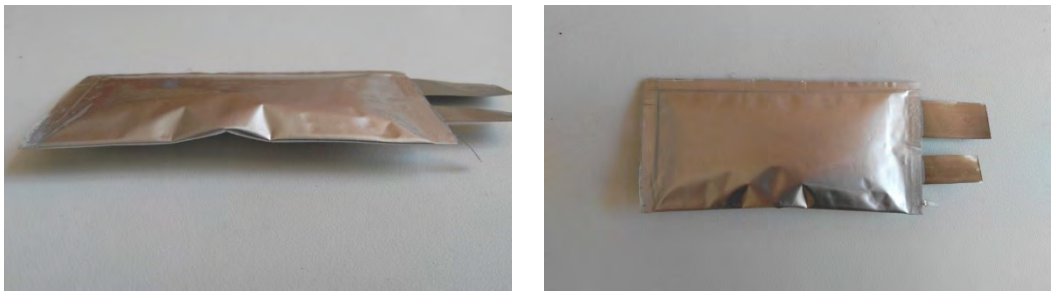

Fig. 1 Prototypes with carrageenan binder.

Acknowledgements

This work was supported by the projects APVV-20-0138 and APVV-20-0111, by the VEGA project No. 1/0095/21 and KEGA project 002UPJS-4/2024.

References

[1] L. Zhang, Y. Wang, Z. Niu, and J. Chen, "Advanced nanostructured carbon-based materials for rechargeable lithium-sulfur batteries," Carbon, vol. 141. Elsevier Ltd, pp. 400–416, Jan. 01, 2019. doi: 10.1016/j.carbon.2018.09.067

[2] S. Chen et al., "3D Hyperbranched Hollow Carbon Nanorod Architectures for High-Performance Lithium-Sulfur Batteries," Adv Energy Mater, vol. 4, no. 8, p. 1301761, Jun. 2014, doi: 10.1002/AENM.201301761.

[3] L. Huang et al., "Electrode Design for Lithium–Sulfur Batteries: Problems and Solutions," Adv Funct Mater, vol. 30, no. 22, p. 1910375, May 2020, doi: 10.1002/ADFM.201910375.

One-Step Mechanochemical Synthesis of Novel Nanostructured and Non-Equilibrium Complex Oxides

V. Šepelák[a]*

[a] Institute of Nanotechnology, Karlsruhe Institute of Technology, Kaiserstraße 12, 76131 Karlsruhe, Germany
*vladimir.sepelak@kit.edu

Complex oxides belong not only to the most abundant phases of the Earth's crust and upper mantle but they constitute on their own a class of materials which are of tremendous scientific and technological importance. Their straightforward synthesis, especially in the nanostructured and far-from-equilibrium states, is a great challenge despite promising developments of preparation techniques. Complex nanooxides with a non-equilibrium short-range structure can hardly be accessed by conventional solid-state thermal routes requiring high temperatures. Also the wet chemistry-based preparation ways lead to the thermodynamically stable rather than metastable products. The present work demonstrates that such hurdles can be overcome by chemical reactions induced by the direct absorption of mechanical energy, i.e., by the mechanochemical synthesis reactions [1]. It is shown that various families of nanostructured complex oxides (germanate, molybdate, silicate, stannate, aluminate, ferrite, gallate) in a highly non-equilibrium state with a variety of structure types (spinel, olivine, perovskite, etc.) can be prepared in a single mechanochemical process, namely, via the one-step high-energy milling [2]. A very facile and efficient mechanochemical synthesis route performed at ambient temperature in air results in complex nanooxides directly from their precursors, without the need for solvents and/or calcination under controlled oxygen fugacity. The non-uniform nanostructure with the distorted constituent polyhedra and the far-from-equilibrium cation arrangement of the mechanochemically synthesized nanooxides as well as their unusual functional properties and thermal stability shall also be highlighted [3-5].

Acknowledgements
The present work is supported by the DFG (project SE 1407/4-2).

References

[1] V. Šepelák, "Foreword," in *Mechanochemistry and Emerging Technologies for Sustainable Chemical Manufacturing*, 1st ed., E. Colacino and F. Garcia, Eds. Boca Raton, FL: CRC Press, 2023, pp. vii – ix, doi: 10.1201/9781003178187.

[2] V. Šepelák, M. Harničárová, J. Valíček, and K. D. Becker, "One-step mechanochemical synthesis of nanostructured and non-equilibrium complex oxides," *Reference Module in Chemistry, Molecular Sciences and Chemical Engineering*, Elsevier, 2024, doi: 10.1016/B978-0-443-15742-4.00006-5.

[3] E. Tóthová, A. Düvel, R. Witte, R. A. Brand, A. Sarkar, R. Kruk, M. Senna, K. L. Da Silva, D. Menzel, V. Girman, M. Hegedüs, M. Baláž, P. Makreski, S. Kubuki, M. Kaňuchová, J. Valíček, H. Hahn, and V. Šepelák, "A unique mechanochemical redox reaction yielding nanostructured double perovskite Sr_2FeMoO_6 with an extraordinarily high degree of anti-site disorder," *Front. Chem.*, vol. 10, art. no. 846910, 2022, doi: 10.3389/fchem.2022.846910.

[4] O. Porodko, M. Fabián, H. Kolev, M. Lisnichuk, M. Zukalová, M. Vinarčíková, V. Girman, K. L. Da Silva, and V. Šepelák, "A novel high entropy spinel-type aluminate MAl_2O_4 (M = Zn, Mg, Cu, Co) and its lithiated oxyfluoride and oxychloride derivatives prepared by one-step mechanosynthesis," *Z. Phys. Chem.*, vol. 236, no. 6–8, pp. 713–726, 2022, doi: 10.1515/zpch-2021-3106.

[5] V. Šepelák, K. L. Da Silva, R. S. Trautwein, K. D. Becker, and H. Hahn, "Unusual cation coordination in nanostructured mullites," *Z. Phys. Chem.*, vol. 236, no. 6–8, pp. 697–712, 2022, doi: 10.1515/zpch-2021-3101.

Electrode Modified by Metal Particles Prepared by Pulse Laser Ablation for Insulin Sensing

I. Šišoláková[a]*, F. Chovancová[a], M. Cvek[b], R. Oriňaková[a,b]

[a] Department of Physical Chemistry, Faculty of Science, Pavol Jozef Šafárik University, Moyzesova 11, 040 11 Košice, Slovak Republic
[b] Centre of Polymer Systems, Tomáš Baťa University in Zlín, Třída Tomáše Bati 5678, 760 01 Zlín, Czech Republic
*ivana.sisolakova@upjs.sk

Due to the rapid increase of requirements for development of fast, cheap, and user-friendly way for various diseases diagnostics, electrochemical sensors represent great interest of the scientific community in last years. Nickel nanoparticles (NiNPs) can be considered as a suitable material for electrode modification for various bioanalytes determination due to its high catalytic activity, which was attributed to the formation of $NiO(OH)^-$ in the alkaline medium [1]. Due to the system miniaturization, and low price of carbon, screen-printed carbon electrodes (SPCEs) are primarily used for analytes determination. Dropsens-made SPCEs type DS 110 (Figure 1) embody one of the most appropriate candidates because of the small size of the working electrode (4 mm diameter). Miniaturization has also led to a reduction in the analytes volume necessary for electrochemical measurements [2]. SPCEs have been widely employed in electrochemical assays also due to their excellent properties, such as the high chemical stability and low background current [3]. To improve the stability, and reproducibility of electrochemical sensors polymer layers are widely used for nanoparticles fixation on the electrode surface [4].

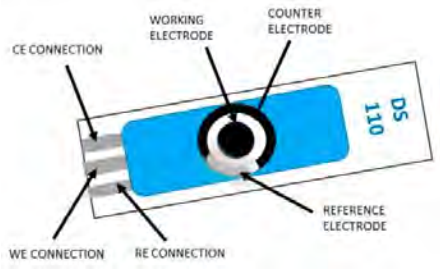

Fig. 1 Screen printed carbon electrode type DS 110.

In this work, the electrochemical oxidation of insulin in human blood serum was studied on SPCE modified by nickel particles prepared by laser ablation Ni(PLA).First, Ni(PLA) were dispersed in a phosphate buffer solution (PBS) containing chitosan to modify the carbon working electrode of SPCE and stabilize the Ni(PLA) on the electrode surface. Fig. 2 shows the cyclic voltammograms (Figure 2, left) of various insulin concentration (0.5 μM to 10 μM) in human blood serum and 0.1 M NaOH. The experimental conditions for insulin oxidation on Ni(PLA)/SPCE involved a potential window from 0 V to +1 V and a scan rate of 50 mV/s. The peak current corresponding to insulin oxidation was observed at E = +0.37 V. Results were fitted by linear function (Figure 2, right) to obtain a correlation coefficient (R^2 = 0.998). Based on the results, Ni(PLA)/SPCE could be a potential sensor for direct and fast insulin detection for clinical diagnostics.

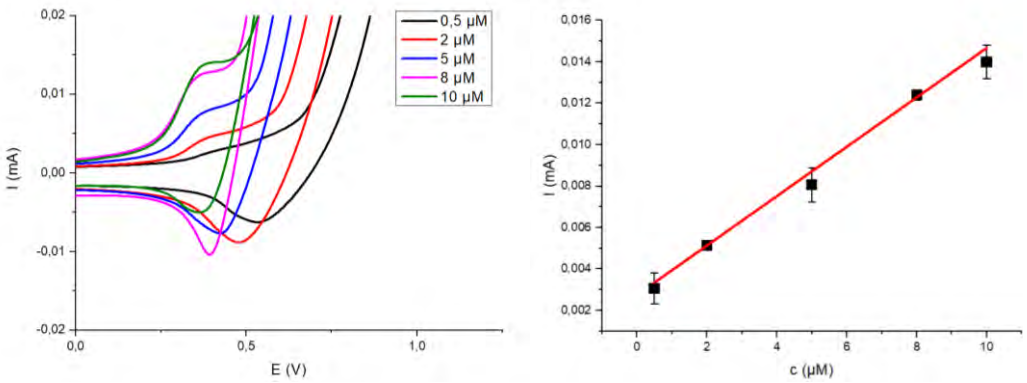

Fig. 2 Cyclic voltammogram of insulin oxidation (0.5 µM to 10 µM) in FHS and 0.1 M NaOH at Ni(PLA)/SPCE. Potential window from 0 V to 1 V and scan rate 50 mV/s (left). The dependence between current response and insulin concentration fitted by linear function R^2 = 0.998 (right).

Acknowledgements

This research was sponsored by the NATO Science for Peace and Security Programme under grant id. G6106. Funded by the EU NextGenerationEU through the Recovery and Resilience Plan for Slovakia under the project No. 09I03-03-V04-00180.

References

[1] X. Hu, X. Hu, Q. Peng, L. Zhou, X. Tan, L. Jiang, C. Tang, H. Wang, S. Liu, Y. Wang, Z. Ning, "Mechanis underlying the photocatalytic degradation pathway of ciprofloxacin with heterogeneous TiO_2," *Chem. Eng. J.*, vol. 380, Jan, 2020, doi.org/10.1016/j.cej.2019.122366.

[2] S. Madhu, S. Ramasamy and J. Choi, "Recent Developments in Electrochemical Sensors for the Detection of Antibiotic-Resistant Bacteria," *Pharmaceuticals*., vol. 15, Nov. 2022, doi.org/10.3390/ph15121488.

[3] A. Aihaiti, Z. Li, Y. Q, F. Meng, X. Li, Z. Huanfu, K. Chen and M. Zhang, "Construction of Electrochemical Sensors for Antibiotic Detection Based on Carbon Nanocomposites," *Nanomaterials (Basel).*, vol. 15, Aug. 2022, doi: 10.3390/nano12162789.

[4] I. Šišolaková, R. Gorejová, F. Chovancová, J. Shepa, F. A. Ngwabebhoh, A. S. Fedorková, P. Sáha, R. Oriňaková, " Polymer-based Electrochemical Sensor: Fast, Accurate, and Simple Insulin Diagnostics Tool," *Electrocatalysis*., Apr. 2023, doi.org/10.1007/s12678-023-00827-w.

$BaZrS_3$ for Photovoltaic Applications. Towards Understanding of the Mechanism of Formation at Moderate Temperatures.

S. K. Tiwari[a], R. Bystrický[ab], P. Hutar[ac], M. Sýkora[a]*

[a] Laboratory for Advanced Materials, Faculty of Natural Sciences, Comenius University, Ilkovičova 6, 842 15 Bratislava, Slovakia
[b] Institute of Inorganic Chemistry, Slovak Academy of Sciences, Dúbravská cesta 9, 845 36 Bratislava, Slovakia
[c] Institute of Electrical Engineering, Slovak Academy of Sciences, Dúbravská cesta 9, 841 04 Bratislava, Slovakia
*sykoram@uniba.sk

Introduction

Organic-inorganic hybrid perovskites (OIHPs) are a class of materials which is been extensively studied due to its extraordinary performance as a photovoltaic absorber layer, rapidly reaching and even exceeding the performance.

of much more mature Crystalline-Silicon technologies. Although OIHPs have excellent photophysical properties

and impressive performance in devices, they suffer from poor ambient stability, rapidly degrading in the presence of Oxygen, humidity, or high temperature. One group of materials that has been recently suggested as a promising alternative are chalcogenide perovskites (CPs), crystalline materials with composition ABX_3, where A, B are cations and X = S, Se anion. CPs offer number of important advantages, as they can be prepared from non-toxic and abundant elements.[1] Many recent computational studies suggest that CPs are likely to have similar or even more appealing electronic properties for application in Photovoltaics (PV) than OIHPs. Among a number of CP's materials $BaZrS_3$ is found to have the properties to act as a solar cell absorber materials i.e. high absorption coefficient, optimal bandgap. $BaZrS_3$ thin films in past were synthesized by high temperature (1000 °C) sulfurization with toxic and flammable gases like CS_2/H_2S.[2] This high temperature synthesis approach is not optimal for the preparation/operation of device as this temperature could lead to the destruction of conductive layers like FTO used as charge transporters.

In this study we explored in-situ formed boron sulfide for the sulfurization of $BaZrO_3$ thin films. The in-situ formed boron sulfide makes the reaction thermodynamically favorable leading to the formation of $BaZrS_3$.[3] A number of reaction parameters were tuned to find the optimal preparation regime of $BaZrS_3$.

Result and discussion

The initial step in preparing $BaZrS_3$ involved reactions at a relatively lower temperature of 500 °C, with varying reaction times to examine the impact of time on the conversion of oxide to sulfide. The XRD pattern shown in Fig.1(a) suggests that with 0 min. holding time at 500 °C, $BaZrO_3$ decomposed into BaS_3 and ZrO_2. Some unreacted $BaZrO_3$ is detected as well. A notable observation is that there was no direct substitution reaction between $BaZrO_3$ and B_2S_3/BS_2, preventing the direct formation of $BaZrS_3$.

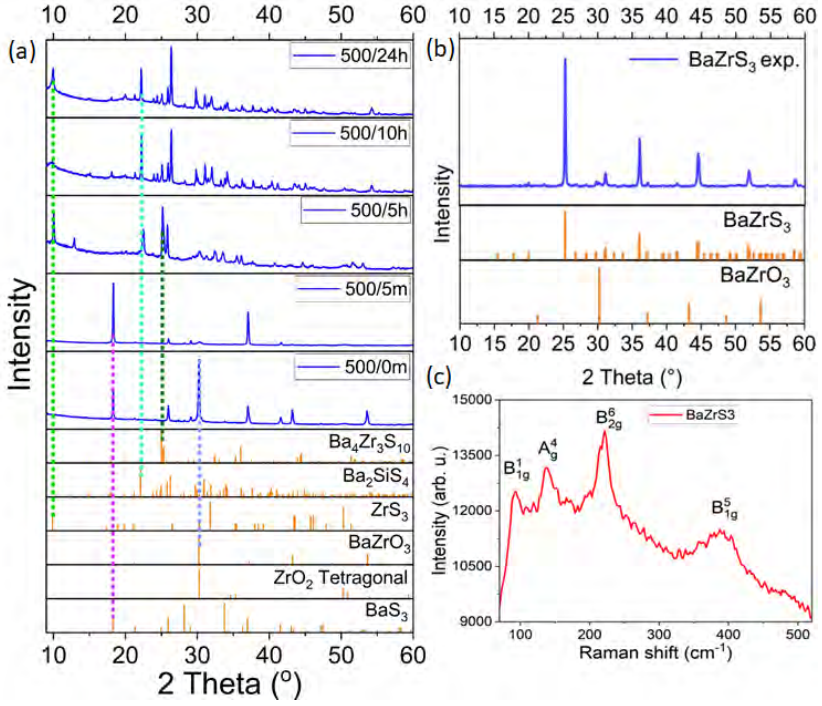

Fig. 1 (a) XRD pattern (blue traces) of the sulfurized thin film at 500 with different exposure time with reference pattern (orange traces). (b,c) XRD and Raman pattern of a $BaZrO_3$ film sulfurized at 560 °C.

Based on these results we propose that the reaction proceeds according to Eq. I.

$$4BaZrO_3(s) + xB_2S_3/BS_2(g) \longrightarrow BaZrO_3 + 3BaS_3 + 3ZrO_2 + xB_2O_3 \quad [I.]$$

With increase in the holding time to 5 minutes, the amount of $BaZrO_3$ was reduced significantly. With a 5-hour holding time, Zr-deficient Ruddlesden−Popper phase, $Ba_4Zr_3S_{10}$, and ZrO_2 was detected, with no $BaZrS_3$ present. Formation of $Ba_4Zr_3S_{10}$ can be attributed to a partial conversion of ZrO_2 to a Zr-poor phase of $BaZrS_3$, possibly due to a presence of a kinetic barrier, which at this temperature is difficult to overcome. Reaction times extended beyond 5h led to the formation of undesired silicate phase Ba_2SiS_4, as well as ZrS_3.

In previous studies it was reported that $B_2S_3(g)$[4] can etch the surface of quartz tube walls, resulting in the formation of SiS_2. Therefore, we hypothesize that at studied conditions SiS_2 likely reacts with $BaZrO_3$ or $BaZrS_3$, which leads to the formation of Ba_2SiS_4, as shown in Eqs. II and III.

$$yB_2S_3(g) + SiO_2(s) \longrightarrow yB_2O_3(s) + SiS_2(g) \quad [II.]$$

$$2BaZrO_3(s) + xB_2S_3/\ BS_2(g) + SiS_2(g) \longrightarrow Ba_2SiS_4(s) + xB_2O_3(s) + 2ZrS_3 \quad [III.]$$

We have investigated the possibility of overcoming the kinetic barrier for the formation of $BaZrS_3$ by varying number of reaction parameters, including temperature and preheating time used for the formation of B_2S_3/BS_2. We observe that at 400 °C/60 min (preheating) followed by 560 °C/10 min holding time resulted the highest $BaZrO_3 \rightarrow BaZrS_3$

conversion rates. The XRD and Raman spectra of the product of the high conversion experiments are shown in Fig.1(b-c). The XRD pattern matches well the $BaZrS_3$ patterns from the crystallographic database ICDS 00-015-0327. A minor peak at 2theta 30.5 degrees is attributed to a trace amount of ZrO_2. The Raman spectra $BaZrS_3$ reveal four prominent peaks in the range 50 and 400 cm^{-1}, which are identified as B_{1g}^1, A_g^4, B_{2g}^6 and B_{1g}^5 modes. This is in agreement with previous Raman studies of $BaZrS_3$.[5]

Acknowledgements

This work was supported by the European Union's Horizon 2020 research and innovation program under grant agreement no. 810701 and by the Slovak Research and Development Agency under grant agreement no. APVV-19-0410, APVV-23-202 and Slovak Ministry of Education under grant agreement No. 1/0892/21. S.K.T. acknowledges support of (1) Grant of the Comenius University Bratislava for Young Scientists: UK/3267/2024 (2) partial support from project USCCCORD (ŽoNFP: NFP313020BUZ3), co-financed by the European Regional Development Fund within the Operation-al Programme Integrated Infrastructure.

References

[1] K. V. Sopiha, C. Comparotto, J. A. Márquez, J. J. S. Scragg, Chalcogenide Perovskites: Tantalizing Prospects, Challenging Materials. *Adv. Optical Mater.* vol. 10, pp. 2101704, 2022,

[2] S. Perera, H. Hui, C. Zhao, H. Xue, F. Sun, C. Deng, N. Gross, C. Milleville, X. Xu, D. F. Watson, B. Weinstein, Y.Y. Sun, S. Zhang,H. Zeng, "Chalcogenide perovskites – an emerging class of ionic semiconductors," *Nano Energ.*, vol. 22, pp. 129-135, 2016.

[3] R. Bystrický, S. K. Tiwari, P. Hutár, L. Vančo, M. Sýkora, "Synthesis of Sulfide Perovskites by Sulfurization with Boron Sulfides," *Inorg. Chem*., vol. 61, n. 47, p. 18823–18827, 2022.

[4] S. W. Martin, D. R. Bloyer, "Preparation of High-Purity Vitreous B_2S_3" *J. Am. Ceram. Soc.*,vol. 73. n. 11, pp. 3481-3485.

[5] S. Dhole, X.Wei, H. Hui, P. Roy, Z. Corey, Y. Wang, W. Nie , A. Chen, H. Zeng and Q. Jia, "A Facile Aqueous Solution Route for the Growth of Chalcogenide Perovskite $BaZrS_3$ Films," *Photonics*, vol. 10, n. 4, pp. 366, 2023.

Biodegradable Thymol-Enriched Nanocomposite Granules with High Biocompatibility and Antibacterial Activity in the Treatment of Bone Defects

M. Trzaskowska[a]*, V. Vivcharenko[a], A. Przekora[a]

[a] Department of Tissue Engineering and Regenerative Medicine, Medical University of Lublin, Chodzki 1, 20-093 Lublin, Poland
*marta.trzaskowska@umlub.pl

Due to their structural similarity to bone tissue, polymer-ceramic biomaterials are of great interest to scientists as fillers for bone defects [1], [2]. However, bone regeneration using biomaterials is hampered by the risk of postoperative infections [3]. The aim of the research was to develop a nanocomposite biomaterial with high biocompatibility, antimicrobial properties, accelerated degradation, and optimal microstructure. Biomaterials in the form of granules consisted of nanohydroxyapatite and a polymer matrix made of agarose and chitosan (chit/aga/nanoHA) or curdlan and chitosan (chit/curd/nanoHA). Additionally, variant of the granules revealing antibacterial properties was enriched with thymol. Cytotoxicity of biomaterials was assessed in indirect contact according to ISO 10993-5:2009 standard and in direct contact after staining of the cells on the surface of the biomaterial with Live/Dead kit. Moreover, specific surface area (SSA), porosity, biodegradability and bioresorption capacity of the biomaterial were evaluated. Antibacterial properties of the granules with immobilized thymol were determined in direct contact with bacteria according to OECD standard for porous materials, No. 202, JT03360420. Furthermore, bacterial biofilm formation on the surface of the granules was assessed. Based on the MTT test, it was confirmed that the produced biomaterials were characterized by a lack of toxicity towards mouse preosteoblasts (MC3T3-E1) (Fig. 1. a). Moreover, the granules supported cell adhesion to their surfaces (Fig. 1. b).

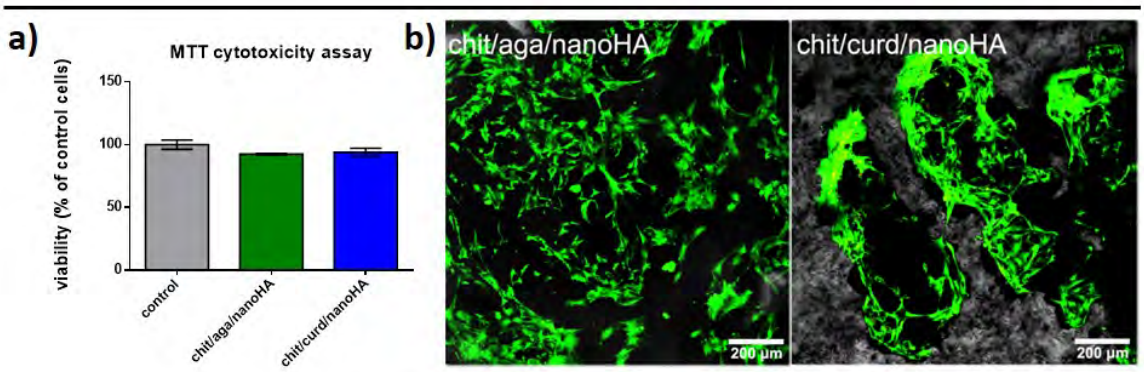

Fig. 1 a) MTT cytotoxicity assay in indirect contact using MC3T3-E1 cell line, b) adhesion and growth of MC3T3-E1 cells visualized by CSLM microscope after Live/Dead staining (live cells emitted green fluorescence and dead cells red fluorescence, magnification 100 ×; scale = 200 µm).

The biomaterials also had a relatively high SSA and high porosity. Additionally, granules were rapidly degraded in an enzyme solution and in an acidic solution. The granules were also bioresorbed with the participation of mouse preosteoblasts (MC3T3-E1), human osteoblasts (hFOB 1.19), and mouse macrophages (RAW 264.7). The antibacterial natural compound (thymol) was immobilized in the aga/chit/nanaHA material microstructure by physical

adsorption at two concentrations: 62.5 µg and 125 µg/100 mg of the granules. The results of direct contact tests showed high antibacterial effect of thymol-containing granules against Gram-negative bacteria (*E. coli, P. aeruginosa*) and lower, concentration-dependent activity against Gram-positive bacteria (*S. aureus*). The biofilm formation test demonstrated that significantly more red fluorescent dead cells of Gram-negative bacteria were observed on the surface of biomaterials with thymol compared to the control. However, in the case of *S. aureus*, no inhibition of biofilm formation by thymol-loaded granules was noted.

The obtained research results indicated that the produced nanocomposite granules are a promising solution in the treatment of small bone defects in maxillofacial surgery and dental procedures. Nevertheless, to fully determine the biomedical potential of the granules, further *in vivo* studies are necessary.

Acknowledgements

The research was funded by National Science Centre (NCN) in Poland within PRELUDIUM 20 no. UMO-2021/41/N/NZ7/01633 and partially supported by the Ministry of Education and Science in Poland within the internal grant dedicated for young scientists of the Medical University of Lublin (PBmb172).

References

[1]D.-E. ; Radulescu, "Novel Trends into the Development of Natural Hydroxyapatite-Based Polymeric Composites for Bone Tissue Engineering," *Polym. 2022, Vol. 14, Page 899*, vol. 14, no. 5, p. 899, Feb. 2022, doi: 10.3390/POLYM14050899.

[2]M. Ebrahimi, M. G. Botelho, and S. V. Dorozhkin, "Biphasic calcium phosphates bioceramics (HA/TCP): Concept, physicochemical properties and the impact of standardization of study protocols in biomaterials research," *Mater. Sci. Eng. C*, vol. 71, pp. 1293–1312, 2017, doi: 10.1016/j.msec.2016.11.039.

[3]W. Zimmerli, "Clinical presentation and treatment of orthopaedic implant-associated infection," *J. Intern. Med.*, vol. 276, no. 2, pp. 111–119, 2014, doi: 10.1111/joim.12233.

8th International Conference on Novel Materials Fundamentals and Applications
High Tatras, 13.-16.10.2024

On the Mechanical and Degradation Behavior of Biodegradable Zinc Foams

C. Wiener[a,b]*,G. Thalmaier[c], R. Gorejová[d]

[a] Department of Materials Science and Engineering, Budapest University of Technology and Economics, Műegyetem rakpart 3., H-1111 Budapest, Hungary
[b] MTA–BME Lendület "Momentum" High-performance Composite Metal Foams Research Group, Műegyetem rakpart 3., Budapest H-1111, Hungary
[c] Faculty of Materials and Environmental Engineering, Technical University of Cluj-Napoca, Bd. Muncii, No. 103–105, 400641 Cluj-Napoca, Romania
[d] Department of Physical Chemistry, Institute of Chemistry, Faculty of Science, Pavol Jozef Šafárik University in Košice, Moyzesova 11, 041 54, Košice, Slovak Republic
*wiener.csilla@gpk.bme.hu

Introduction

With the rise in surgical interventions due to increased human lifespan and accidents, challenges associated with traditional implants used in orthopedic surgery must be addressed. There are two major drawbacks to traditional implants. In the case of long-term implants, stress shielding and the release of toxic metal ions are of major concern [1], while for short-term implants like screws, the secondary surgery for removing the implant delays the patient's recovery; both the time off work and the surgery itself are expensive. Biodegradable materials can overcome the latter problem since they provide temporary support for damaged tissues and then gradually dissolve without the need for a secondary surgery to remove the implant.

In the last decades, biodegradable metals such as magnesium, iron, and zinc and their alloys have been highly investigated for orthopedic implants and stent applications. Iron and its alloys were found to degrade very slowly even when applying surface modification [2]. Magnesium alloys were found to be applicable as biodegradable stent materials; however, non-uniform degradation was found in these alloys [3]. Zinc and its alloys exhibit an appropriate degradation rate for orthopedic implants, but pure zinc has low strength for the intended application. Thus, many papers investigate possible alloying so that the zinc alloy remains biocompatible and has appropriate mechanical properties [4].

Nowadays, zinc-based metal foams have gained attention due to their structure. Since the structure of foams resembles the structure of human bone, it is very advantageous for orthopedics, allowing faster regeneration of the tissue. Despite these advantages, research on zinc-based foams for biomedical applications remains limited. Most of the papers report only on developing new zinc foams and the influence of the manufacturing parameters on their compressive properties [5].

Zinc foams can be manufactured by various methods. The three most widely used are casting, powder metallurgy, and electrodeposition. Previously, we investigated low-density open-cell foams produced by a modified investment casting method [6]. Here we changed the pore size and the struts' thickness, thus the density of the foams. We found that due to the immersion of the foams in Hank's solution, the mechanical response changed: the slope in the "plateau" region was wavier and the slope was smaller. Also, strain localization was observed. These changes were explained by microcrack propagation into the zinc due to corrosion. We continued the investigation with another cast sample and compared it with the characteristics of the samples produced by the powder metallurgical method.

Materials and results

Two types of manufacturing techniques were employed to produce different types of zinc foams to investigate the effect of manufacturing on mechanical and corrosion properties. In both cases we used the space holder method, and the space holder was NaCl salt for both techniques. First, samples with two different pore-size (~1 mm and ~0.7 mm) were produced by powder metallurgical (PM) method. In this case, after mixing the Zn powder with the sieved salt

particles for 15 minutes in a tumbler at 60 rpm, the blend was compressed with 500 MPa of pressure, then sintered at 410 ˚C for 3 hours. Finally, the salt particles were leached out. In the case of casting, low-pressure infiltration was applied on previously sieved and sintered salt particles. After cooling at ambient temperature, the salt particles were leached out from the cast block.

For the compression test rectangular blocks of 12x12x12 mm^3 were tested for the cast samples, while cylindrical samples (12.8 mm in diameter and 8 mm in length) were compressed in the case of samples manufactured by powder metallurgical method. The density of the samples was 2.8±0.2 g cm^{-3} regardless of the pore-size and the manufacturing method.

The samples were tested in compression as recieved and after a four-weeks immersion in Hanks' solution (8 g l^{-1} NaCl, 0.4 g l^{-1} KCl, 0.14 g l^{-1} $CaCl_2$, 0.06 g l^{-1}, $MgSO_4 \cdot 7H_2O$, 0.06 g l^{-1} $NaH_2PO_4 \cdot 2H_2O$, 0.35 g l^{-1} $NaHCO_3$, 1.00 g l^{-1} glucose, 0.60 g l^{-1}, KH_2PO_4, and 0.10 g l^{-1} $MgCl_2 \cdot 6H_2O$) at 37 ± 2 °C.

All types of zinc foams show similar stress-strain curves, which consist of three stages (Figure 1). The first stage is the quasi-linear stage, where the deformation is caused by the bending of the cell edge. The quasi-linear stage is followed by the region, where the cells collapse. The cast sample exhibit the highest stiffness and yield strength, which is partly due to the density difference.

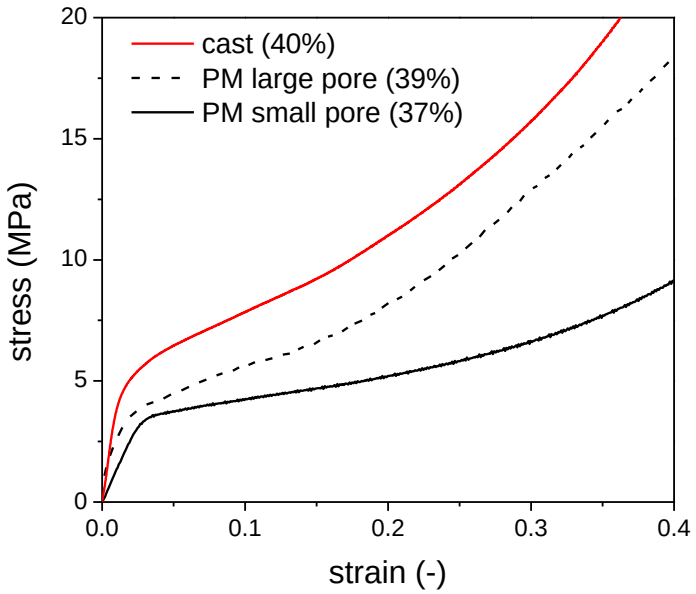

Fig. 1 Typical stress-strain curves of the different foam types. The relative density is given in parentheses.

We found that the amount of corrosion products depends on the used the manufacturing technique as Fig. 2 shows. PM samples have less corrosion products on their surface. It seems that the corrosion properties depend on the pore-size and the manufacturing method.

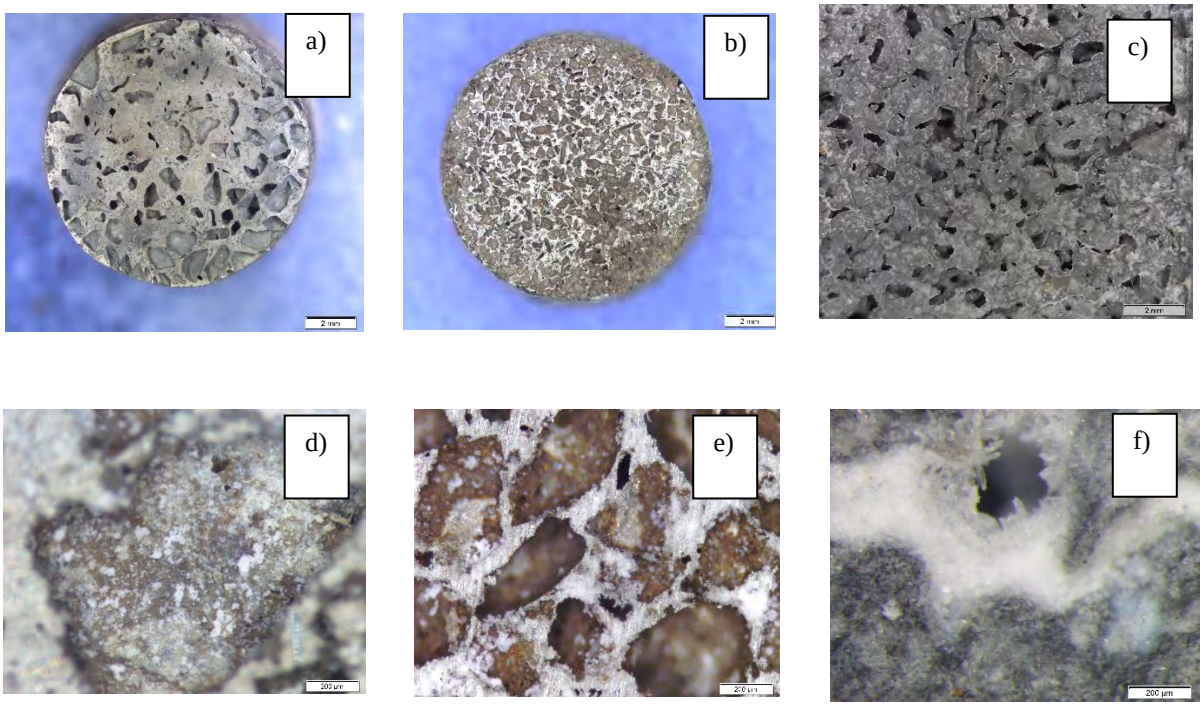

Fig. 2 Stereo microscopic images of a), e) PM sample with large pores, b), e) PM sample with small pores, c), f) cast sample as received (a), b), c)) and after the immersion in Hank's solution (d). e), f)).

Acknowledgements

This work was supported by the Visegrad Grant from International Visegrad Fund. (project no. 22310096) and by the Government Office of the Slovak Republic under the call Fellowships for excellent researchers R2-R4 (project. ZETA no. 09I03-03-V04-00010).

References

[1] C. Shuai, S. Li, S. Peng, P. Feng, Y. Lai, and C. Gao, "Biodegradable metallic bone implants," *Mater. Chem. Front.*, vol. 3, no. 4, pp. 544–562, Jan. 2019, doi: 10.1039/C8QM00507A.

[2] R. Gorejová, L. Haverová, R. Oriňaková, A. Oriňak, and M. Oriňak, "Recent advancements in Fe-based biodegradable materials for bone repair," *J. Mater. Sci.*, vol. 54, no .3, 1913–1947, 2019, doi: 10.1007/s10853-018-3011-z.

[3] N. T. Kirkland, N. Birbilis, and M. P. Staiger. "Assessing the corrosion of biodegradable magnesium implants: A critical review of current methodologies and their limitations," *Acta Biomat.*, vol. 8, no.3, 925–936, 2012, doi: 10.1016/j.actbio.2011.11.014.

[4] H. Kabir, K. Munir, C. Wen, C. and Y. Li, "Recent research and progress of biodegradable zinc alloys and composites for biomedical applications: Biomechanical and biocorrosion perspectives," *Bioactive Mater.*, vol. 6, no. 3, 836–879, 2021, doi: 10.1016/j.bioactmat.2020.09.013.

[5] R. Oriňaková, R. Gorejová, Z.O. Králová, M. Petráková, and A. Oriňak, "Novel trends and recent progress on preparation methods of biodegradable metallic foams for biomedicine: a review," *J. Mater. Sci.*, vol. 56, no. 25, pp. 13925–13963, 2021, https://doi.org/10.1007/s10853-021-06163-y.

[6] C. Kádár, R. Gorejová, P. Kubelka, R. Oriňaková, R. and I.N. Orbulov, " Mechanical and Degradation Behavior of Zinc-Based Biodegradable Metal Foams" *Adv. Eng. Mater.*, vol. 26, 2301496, Jan. 2024, doi: 10.1002/adem.202301496

Smart, Macroporous Bone Implant Based on pH-Sensitive Zeolite-Chitosan-Bisphosphonate Complex

A. Wójcik[a]*, P. Kazimierczak[a], J. Matusiak[b], R. Panek[b], W. Franus[b], A. Przekora[a]

[a] Medical University of Lublin, Department of Tissue Engeneering and Regenerative Medicine, Poland
[b] Lublin University of Technology, Department of Building Materials Engeneering and Geoengineering, Poland
*AlicjaWojcik1@umlub.pl

Introduction

Osteoporosis is the most common systemic metabolic bone disease. It is characterized by low bone mass and destruction of the microstructure of bone tissue, leading to increased bone fragility. Although osteoporosis can occur at any age and in both sexes, its incidence increases with age, and it affects women more often than men [1]. Unfortunately, existing therapeutic strategies are often burdened with a number of troublesome side effects. With the aging of our societies, the number of patients suffering from osteoporosis is likely to increase. For this reason, an intensive search for new therapeutic methods in the treatment of fractures, so common in the course of osteoporosis, should be undertaken.

A biomaterial that is intended to accelerate bone formation process should promote adhesion, proliferation, differentiation of osteoprogenitor cells and osteoblasts [2]. In the case of osteoprotic fractures, ideally, implant should inhibit osteoclasts activity, and thus bone repsorption process. In response to this need, a smart bone implant based on a zeolite-bisphosphonate complex, which responds to a decrease in pH level, was developed. The presented biomaterial can be used as an implant releasing a drug with anti-osteoporotic effect - sodium risedronate - during the bone healing process in response to acidified microenvironment created by osteoclasts. Due to its microstructural, chemical and biological properties, it will also significantly support bone regeneration processes at the implantation site.

Material and Methods

The bone implant was made of a pH-sensitive zeolite-chitosan-bisphosphonate complex (Na-X-chitosan-risedronate), Na-X zeolite functionalized with chitosan (Na-X-chitosan), hydroxyapatite, chitosan and agarose. The production method of the smart biomaterial was described in a Polish patent application no P.449568. All components were mixed in acetic acid solution, then a porogen was added (sodium bicarbonate), and the obtained paste was subjected to high temperature, then cooled, frozen and freeze-dried. After freeze-drying, the obtained biomaterial was soaked in a phosphate buffered saline (PBS) and air-dried. Microstructure of the biomaterial was visualized using SEM. The pH-responsive behaviour of smart implant based on zeolite-chitosan-bisphosphonate complex was determined using citrate buffer (pH 4). The amount of released drug after incubation in acidic solution was measured using a spectrophotometer at 262 nm. The biocompatibility *in vitro* was evaluated using normal human fetal osteoblast cell line (hFOB 1.19, ATCC-LGC Standards, UK). hFOB 1.19 cells were cultured in a 1:1 mixture of DMEM/Ham's F12 medium without phenol red (Sigma-Aldrich Chemicals, Poland), supplemented with 10% foetal bovine serum (Pan-Biotech GmbH, Germany), 1% antibiotic solution (100 U/mL penicillin and 100 µg/mL streptomycin), and 0.3 mg/mL G418 (Sigma-Aldrich Chemicals, Poland), and maintained at 34 ˚C with 5% CO_2 in an air atmosphere. Biological safety of the implant was tested according to ISO 10993-5 standard for medical devices. Osteoblast viability on the biomaterial surface was confirmed by Live/Dead staining and confocal microscope (CLSM) observation. Cell proliferation was assessed qualitatively by CLSM observation after fluorescent staining of the cytoskeleton with AlexaFluor®635 phalloidin and cell nuclei with DAPI on the 3rd and 7th day of culture on the bone implant surface.

Results

Produced smart bone implant showed porous microstructure and ability to release the anti-osteoporotic drug in response to acidified microenvironment. Biomaterial was nontoxic according to ISO 10993-5 standard since cell viability exceeded 70%. Live/Dead staining demonstrated that osteoblasts grown on the surface of the implant were well-spread, revealed normal morphology and were viable. Moreover, the obtained CLSM images after staining of cell cytoskeleton and nuclei revealed a significant increase in cell number over time, proving that the biomaterial supported cell proliferation (Figure 1).

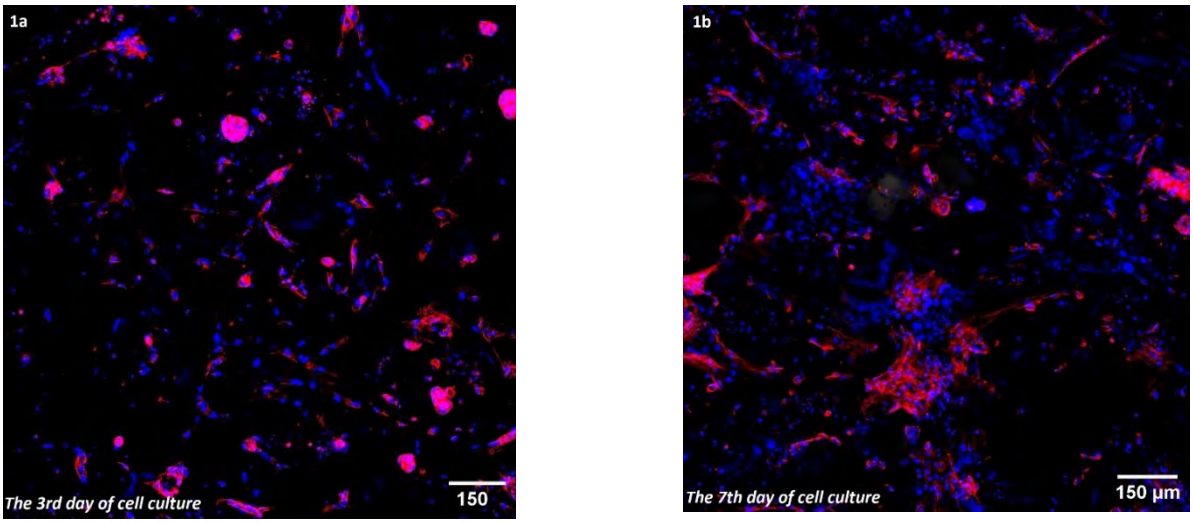

Fig. 1 Assessment of biomaterial biocompatibility *in vitro*: CLSM images showing the growth of hFOB 1.19 cells cultured on the surface of the bone implant for 3 (Figure 1a) and 7 (Figure 1b) days (nuclei – blue fluorescence, cytoskeleton filaments – red fluorescence).

Conclusions

The developed bone implant is highly biocompatible. This makes it a promising candidate for use as a smart bone implant containing a complex of zeolite, chitosan and pH-responsive bisphosphonate in the treatment of osteoporotic fractures. The use of a bone implant releasing the anti-osteoporotic drug - sodium risedronate - only locally allows to avoid side effects occurring when it is used systemically, thus allowing for increased comfort of patients' convalescence.

Acknowledgements

This research was funded by the National Science Centre (NCN) in Poland within OPUS 22 grant no. UMO-2021/43/B/NZ7/00447 and supported by the Visegrad grants from the International Visegrad Fund (project no. 22310096).

References

[1] Sözen T, Özışık L, Başaran NÇ. “An overview and management of osteoporosis,” *Eur J Rheumatol*., vol. 4(1), pp. 46-56. Mar. 2017.

[2] Chun HJ, Gun-Woo K, Chun-Ho K. “Fabrication of porous chitosan scaffold in order to improve biocompatibility,” *J Phys Chem Sol*, vol. 69(5-6), pp. 1573-1576, 2008.

The 8th International Conference on Novel Materials Fundamentals and Applications
Book of Abstracts

Edited by: RNDr. Jana Shepa PhD.

Publisher: Pavol Jozef Šafárik University in Košice
Publishing ŠafárikPress

Year: 2024
Pages: 131
Author's sheets: 8.12
Edition: first

ISBN 978-80-574-0353-1 (e-publication)